The Astrophysical Journal Letters, 900:L13 (27pp), 2020 September 1 https://doi.org/10.3847/2041-8213/aba493

Properties and Astrophysical Implications of the 150 $M_\odot$ Binary Black Hole Merger GW190521

R. Abbott[1], T. D. Abbott[2], S. Abraham[3], F. Acernese[4,5], K. Ackley[6], C. Adams[7], R. X. Adhikari[1], V. B. Adya[8], C. Affeldt[9,10], M. Agathos[11,12], K. Agatsuma[13], N. Aggarwal[14], O. D. Aguiar[15], A. Aich[16], L. Aiello[17,18], A. Ain[3], P. Ajith[19], S. Akcay[11], G. Allen[20], A. Allocca[21], P. A. Altin[8], A. Amato[22], S. Anand[1], A. Ananyeva[1], S. B. Anderson[1], W. G. Anderson[23], S. V. Angelova[24], S. Ansoldi[25,26], S. Antier[27], S. Appert[1], K. Arai[1], M. C. Araya[1], J. S. Areeda[28], M. Arène[27], N. Arnaud[29,30], S. M. Aronson[31], K. G. Arun[32], Y. Asali[33], S. Ascenzi[17,34], G. Ashton[6], S. M. Aston[7], P. Astone[35], F. Aubin[36], P. Aufmuth[10], K. AultONeal[37], C. Austin[2], V. Avendano[38], S. Babak[27], P. Bacon[27], F. Badaracco[17,18], M. K. M. Bader[39], S. Bae[40], A. M. Baer[41], J. Baird[27], F. Baldaccini[42,43], G. Ballardin[30], S. W. Ballmer[44], A. Bals[37], A. Balsamo[41], G. Baltus[45], S. Banagiri[46], D. Bankar[3], R. S. Bankar[3], J. C. Barayoga[1], C. Barbieri[47,48], B. C. Barish[1], D. Barker[49], K. Barkett[50], P. Barneo[51], F. Barone[5,52], B. Barr[53], L. Barsotti[54], M. Barsuglia[27], D. Barta[55], J. Bartlett[49], I. Bartos[31], R. Bassiri[56], A. Basti[21,57], M. Bawaj[43,58], J. C. Bayley[53], M. Bazzan[59,60], B. Bécsy[61], M. Bejger[62], I. Belahcene[29], A. S. Bell[53], D. Beniwal[63], M. G. Benjamin[37], J. D. Bentley[13], F. Bergamin[9], B. K. Berger[56], G. Bergmann[9,10], S. Bernuzzi[11], C. P. L. Berry[14], D. Bersanetti[64], A. Bertolini[39], J. Betzwieser[7], R. Bhandare[65], A. V. Bhandari[3], J. Bidler[28], E. Biggs[23], I. A. Bilenko[66], G. Billingsley[1], R. Birney[67], O. Birnholtz[68,69], S. Biscans[1,54], M. Bischi[70,71], S. Biscoveanu[54], A. Bisht[10], G. Bissenbayeva[16], M. Bitossi[21,30], M. A. Bizouard[72], J. K. Blackburn[1], J. Blackman[50], C. D. Blair[7], D. G. Blair[73], R. M. Blair[49], F. Bobba[74,75], N. Bode[9,10], M. Boer[72], Y. Boetzel[76], G. Bogaert[72], F. Bondu[77], E. Bonilla[56], R. Bonnand[36], P. Booker[9,10], B. A. Boom[39], R. Bork[1], V. Boschi[21], S. Bose[3], V. Bossilkov[73], J. Bosveld[73], Y. Bouffanais[59,60], A. Bozzi[30], C. Bradaschia[21], P. R. Brady[23], A. Bramley[7], M. Branchesi[17,18], J. E. Brau[78], M. Breschi[11], T. Briant[79], J. H. Briggs[53], F. Brighenti[70,71], A. Brillet[72], M. Brinkmann[9,10], P. Brockill[23], A. F. Brooks[1], J. Brooks[30], D. D. Brown[63], S. Brunett[1], G. Bruno[80], R. Bruntz[41], A. Buikema[54], T. Bulik[81], H. J. Bulten[39,82], A. Buonanno[83,84], R. Buscicchio[13], D. Buskulic[36], R. L. Byer[56], M. Cabero[9,10], L. Cadonati[85], G. Cagnoli[86], C. Cahillane[1], J. Calderón Bustillo[6], J. D. Callaghan[53], T. A. Callister[1], E. Calloni[5,87], J. B. Camp[88], M. Canepa[64,89], K. C. Cannon[90], H. Cao[63], J. Cao[91], G. Carapella[74,75], F. Carbognani[30], S. Caride[92], M. F. Carney[14], G. Carullo[21,57], J. Casanueva Diaz[21], C. Casentini[34,93], J. Castañeda[51], S. Caudill[39], M. Cavaglià[94], F. Cavalier[29], R. Cavalieri[30], G. Cella[21], P. Cerdá-Durán[95], E. Cesarini[34,96], O. Chaibi[72], K. Chakravarti[3], C. Chan[90], M. Chan[53], S. Chao[97], P. Charlton[98], E. A. Chase[14], E. Chassande-Mottin[27], D. Chatterjee[23], M. Chaturvedi[65], K. Chatziioannou[99,100], H. Y. Chen[101], X. Chen[73], Y. Chen[50], H.-P. Cheng[31], C. K. Cheong[102], H. Y. Chia[31], F. Chiadini[75,103], R. Chierici[104], A. Chincarini[64], A. Chiummo[30], G. Cho[105], H. S. Cho[106], M. Cho[84], N. Christensen[72], Q. Chu[73], S. Chua[79], K. W. Chung[102], S. Chung[73], G. Ciani[59,60], P. Ciecielag[62], M. Cieślar[62], A. A. Ciobanu[63], R. Ciolfi[60,107], F. Cipriano[72], A. Cirone[64,89], F. Clara[49], J. A. Clark[85], P. Clearwater[108], S. Clesse[80], F. Cleva[72], E. Coccia[17,18], P.-F. Cohadon[79], D. Cohen[29], M. Colleoni[109], C. G. Collette[110], C. Collins[13], M. Colpi[47,48], M. Constancio, Jr.,[15], L. Conti[60], S. J. Cooper[13], P. Corban[7], T. R. Corbitt[2], I. Cordero-Carrión[111], S. Corezzi[42,43], K. R. Corley[33], N. Cornish[61], D. Corre[29], A. Corsi[92], S. Cortese[30], C. A. Costa[15], R. Cotesta[83], M. W. Coughlin[1], S. B. Coughlin[14,112], J.-P. Coulon[72], S. T. Countryman[33], P. Couvares[1], P. B. Covas[109], D. M. Coward[73], M. J. Cowart[7], D. C. Coyne[1], R. Coyne[113], J. D. E. Creighton[23], T. D. Creighton[16], J. Cripe[2], M. Croquette[79], S. G. Crowder[114], J.-R. Cudell[45], T. J. Cullen[2], A. Cumming[53], R. Cummings[53], L. Cunningham[53], E. Cuoco[30], M. Curylo[81], T. Dal Canton[83], G. Dálya[115], A. Dana[56], L. M. Daneshgaran-Bajastani[116], B. D'Angelo[64,89], S. L. Danilishin[9,10], S. D'Antonio[34], K. Danzmann[9,10], C. Darsow-Fromm[117], A. Dasgupta[118], L. E. H. Datrier[53], V. Dattilo[30], I. Dave[65], M. Davier[29], G. S. Davies[119], D. Davis[44], E. J. Daw[120], D. DeBra[56], M. Deenadayalan[3], J. Degallaix[22], M. De Laurentis[5,87], S. Deléglise[79], M. Delfavero[68], N. De Lillo[53], W. Del Pozzo[21,57], L. M. DeMarchi[14], V. D'Emilio[112], N. Demos[54], T. Dent[119], R. De Pietri[121,122], R. De Rosa[5,87], C. De Rossi[30], R. DeSalvo[123], O. de Varona[9,10], S. Dhurandhar[3], M. C. Díaz[16], M. Diaz-Ortiz, Jr.[31], T. Dietrich[39], L. Di Fiore[5], C. Di Fronzo[13], C. Di Giorgio[74,75], F. Di Giovanni[95], M. Di Giovanni[124,125], T. Di Girolamo[5,87], A. Di Lieto[21,57], B. Ding[110], S. Di Pace[35,126], I. Di Palma[35,126], F. Di Renzo[21,57], A. K. Divakarla[31], A. Dmitriev[13], Z. Doctor[101], F. Donovan[54], K. L. Dooley[112], S. Doravari[3], I. Dorrington[112], T. P. Downes[23], M. Drago[17,18], J. C. Driggers[49], Z. Du[91], J.-G. Ducoin[29], P. Dupej[53], O. Durante[74,75], D. D'Urso[127,128], S. E. Dwyer[49], P. J. Easter[6], G. Eddolls[53], B. Edelman[78], T. B. Edo[120], O. Edy[129], A. Effler[7], P. Ehrens[1], J. Eichholz[8], S. S. Eikenberry[31], M. Eisenmann[36], R. A. Eisenstein[54], A. Ejlli[112], L. Errico[5,87], R. C. Essick[101], H. Estelles[109], D. Estevez[36], Z. B. Etienne[130], T. Etzel[1], M. Evans[54], T. M. Evans[7], B. E. Ewing[131], V. Fafone[17,34,93], S. Fairhurst[112], X. Fan[91], S. Farinon[64], B. Farr[78], W. M. Farr[99,100], E. J. Fauchon-Jones[112], M. Favata[38], M. Fays[120], M. Fazio[132], J. Feicht[1], M. M. Fejer[56], F. Feng[27], E. Fenyvesi[55,133], D. L. Ferguson[85], A. Fernandez-Galiana[54], I. Ferrante[21,57], E. C. Ferreira[15], T. A. Ferreira[15], F. Fidecaro[21,57], I. Fiori[30], D. Fiorucci[17,18], M. Fishbach[101], R. P. Fisher[41], R. Fittipaldi[75,134], M. Fitz-Axen[46], V. Fiumara[75,135], R. Flaminio[36,136], E. Floden[46], E. Flynn[28], H. Fong[90], J. A. Font[95,137], P. W. F. Forsyth[8], J.-D. Fournier[72], S. Frasca[35,126], F. Frasconi[21], Z. Frei[115], A. Freise[13], R. Frey[78], V. Frey[29], P. Fritschel[54], V. V. Frolov[7], G. Fronzè[138], P. Fulda[31], M. Fyffe[7], H. A. Gabbard[53], B. U. Gadre[83], S. M. Gaebel[13], J. R. Gair[83], S. Galaudage[6], D. Ganapathy[54], S. G. Gaonkar[3], C. García-Quirós[109], F. Garufi[5,87], B. Gateley[49], S. Gaudio[37], V. Gayathri[139], G. Gemme[64], E. Genin[30], A. Gennai[21], D. George[20], J. George[65], L. Gergely[140], S. Ghonge[85], Abhirup Ghosh[83], Archisman Ghosh[39,141,142,143], S. Ghosh[23], B. Giacomazzo[124,125], J. A. Giaime[2,7], K. D. Giardina[7],

D. R. Gibson[67], C. Gier[24], K. Gill[33], J. Glanzer[2], J. Gniesmer[117], P. Godwin[131], E. Goetz[2,94], R. Goetz[31], N. Gohlke[9,10], B. Goncharov[6], G. González[2], A. Gopakumar[144], S. E. Gossan[1], M. Gosselin[21,30,57], R. Gouaty[36], B. Grace[8], A. Grado[5,145], M. Granata[22], A. Grant[53], S. Gras[54], P. Grassia[1], C. Gray[49], R. Gray[53], G. Greco[70,71], A. C. Green[31], R. Green[112], E. M. Gretarsson[37], H. L. Griggs[85], G. Grignani[42,43], A. Grimaldi[124,125], S. J. Grimm[17,18], H. Grote[112], S. Grunewald[83], P. Gruning[29], G. M. Guidi[70,71], A. R. Guimaraes[2], G. Guixé[51], H. K. Gulati[118], Y. Guo[39], A. Gupta[131], Anchal Gupta[1], P. Gupta[39], E. K. Gustafson[1], R. Gustafson[146], L. Haegel[109], O. Halim[17,18], E. D. Hall[54], E. Z. Hamilton[112], G. Hammond[53], M. Haney[76], M. M. Hanke[9,10], J. Hanks[49], C. Hanna[131], M. D. Hannam[112], O. A. Hannuksela[102], T. J. Hansen[37], J. Hanson[7], T. Harder[72], T. Hardwick[2], K. Haris[19], J. Harms[17,18], G. M. Harry[147], I. W. Harry[129], R. K. Hasskew[7], C.-J. Haster[54], K. Haughian[53], F. J. Hayes[53], J. Healy[68], A. Heidmann[79], M. C. Heintze[7], J. Heinze[9,10], H. Heitmann[72], F. Hellman[148], P. Hello[29], G. Hemming[30], M. Hendry[53], I. S. Heng[53], E. Hennes[39], J. Hennig[9,10], M. Heurs[9,10], S. Hild[53,149], T. Hinderer[39,141,143], S. Y. Hoback[28,147], S. Hochheim[9,10], E. Hofgard[56], D. Hofman[22], A. M. Holgado[20], N. A. Holland[8], K. Holt[7], D. E. Holz[101], P. Hopkins[112], C. Horst[23], J. Hough[53], E. J. Howell[73], C. G. Hoy[112], Y. Huang[54], M. T. Hübner[6], E. A. Huerta[20], D. Huet[29], B. Hughey[37], V. Hui[36], S. Husa[109], S. H. Huttner[53], R. Huxford[131], T. Huynh-Dinh[7], B. Idzkowski[81], A. Iess[34,93], H. Inchauspe[31], C. Ingram[63], G. Intini[35,126], J.-M. Isac[79], M. Isi[54], B. R. Iyer[19], T. Jacqmin[79], S. J. Jadhav[150], S. P. Jadhav[3], A. L. James[112], K. Jani[85], N. N. Janthalur[150], P. Jaranowski[151], D. Jariwala[31], R. Jaume[109], A. C. Jenkins[152], J. Jiang[31], G. R. Johns[41], N. K. Johnson-McDaniel[12], A. W. Jones[13], D. I. Jones[153], J. D. Jones[49], P. Jones[13], R. Jones[53], R. J. G. Jonker[39], L. Ju[73], J. Junker[9,10], C. V. Kalaghatgi[112], V. Kalogera[14], B. Kamai[1], S. Kandhasamy[3], G. Kang[40], J. B. Kanner[1], S. J. Kapadia[19], S. Karki[78], R. Kashyap[19], M. Kasprzack[1], W. Kastaun[9,10], S. Katsanevas[30], E. Katsavounidis[54], W. Katzman[7], S. Kaufer[10], K. Kawabe[49], F. Kéfélian[72], D. Keitel[129], A. Keivani[33], R. Kennedy[120], J. S. Key[154], S. Khadka[56], F. Y. Khalili[66], I. Khan[17,34], S. Khan[9,10], Z. A. Khan[91], E. A. Khazanov[155], N. Khetan[17,18], M. Khursheed[65], N. Kijbunchoo[8], Chunglee Kim[156], G. J. Kim[85], J. C. Kim[157], K. Kim[102], W. Kim[63], W. S. Kim[158], Y.-M. Kim[159], C. Kimball[14], P. J. King[49], M. Kinley-Hanlon[53], R. Kirchhoff[9,10], J. S. Kissel[49], L. Kleybolte[117], S. Klimenko[31], T. D. Knowles[130], E. Knyazev[54], P. Koch[9,10], S. M. Koehlenbeck[9,10], G. Koekoek[39,149], S. Koley[39], V. Kondrashov[1], A. Kontos[160], N. Koper[9,10], M. Korobko[117], W. Z. Korth[1], M. Kovalam[73], D. B. Kozak[1], V. Kringel[9,10], N. V. Krishnendu[32], A. Królak[161,162], N. Krupinski[23], G. Kuehn[9,10], A. Kumar[150], P. Kumar[163], Rahul Kumar[49], Rakesh Kumar[118], S. Kumar[19], L. Kuo[97], A. Kutynia[161], B. D. Lackey[83], D. Laghi[21,57], E. Lalande[164], T. L. Lam[102], A. Lamberts[72], M. Landry[49], B. B. Lane[54], R. N. Lang[165], J. Lange[68], B. Lantz[56], R. K. Lanza[54], I. La Rosa[36], A. Lartaux-Vollard[29], P. D. Lasky[6], M. Laxen[7], A. Lazzarini[1], C. Lazzaro[60], P. Leaci[35,126], S. Leavey[9,10], Y. K. Lecoeuche[49], C. H. Lee[106], H. M. Lee[166], H. W. Lee[157], J. Lee[105], K. Lee[56], J. Lehmann[9,10], N. Leroy[29], N. Letendre[36], Y. Levin[6], A. K. Y. Li[102], J. Li[91], K. li[102], T. G. F. Li[102], X. Li[50], F. Linde[39,167], S. D. Linker[116], J. N. Linley[53], T. B. Littenberg[168], J. Liu[9,10], X. Liu[23], M. Llorens-Monteagudo[95], R. K. L. Lo[1], A. Lockwood[169], L. T. London[54], A. Longo[170,171], M. Lorenzini[17,18], V. Loriette[172], M. Lormand[7], G. Losurdo[21], J. D. Lough[9,10], C. O. Lousto[68], G. Lovelace[28], H. Lück[9,10], D. Lumaca[34,93], A. P. Lundgren[129], Y. Ma[50], R. Macas[112], S. Macfoy[24], M. MacInnis[54], D. M. Macleod[112], I. A. O. MacMillan[147], A. Macquet[72], I. Magaña Hernandez[23], F. Magaña-Sandoval[31], R. M. Magee[131], E. Majorana[35], I. Maksimovic[172], A. Malik[65], N. Man[72], V. Mandic[46], V. Mangano[35,53,126], G. L. Mansell[49,54], M. Manske[23], M. Mantovani[30], M. Mapelli[59,60], F. Marchesoni[43,58,173], F. Marion[36], S. Márka[33], Z. Márka[33], C. Markakis[12], A. S. Markosyan[56], A. Markowitz[1], E. Maros[1], A. Marquina[111], S. Marsat[27], F. Martelli[70,71], I. W. Martin[53], R. M. Martin[38], V. Martinez[86], D. V. Martynov[13], H. Masalehdan[117], K. Mason[54], E. Massera[120], A. Masserot[36], T. J. Massinger[54], M. Masso-Reid[53], S. Mastrogiovanni[27], A. Matas[83], F. Matichard[1,54], N. Mavalvala[54], E. Maynard[2], J. J. McCann[73], R. McCarthy[49], D. E. McClelland[8], S. McCormick[7], L. McCuller[54], S. C. McGuire[174], C. McIsaac[129], J. McIver[1], D. J. McManus[8], T. McRae[8], S. T. McWilliams[130], D. Meacher[23], G. D. Meadors[6], M. Mehmet[9,10], A. K. Mehta[19], E. Mejuto Villa[75,123], A. Melatos[108], G. Mendell[49], R. A. Mercer[23], L. Mereni[22], K. Merfeld[78], E. L. Merilh[49], J. D. Merritt[78], M. Merzougui[72], S. Meshkov[1], C. Messenger[53], C. Messick[175], R. Metzdorff[79], P. M. Meyers[108], F. Meylahn[9,10], A. Mhaske[3], A. Miani[124,125], H. Miao[13], I. Michaloliakos[31], C. Michel[22], H. Middleton[108], L. Milano[5,87], A. L. Miller[31,35,126], M. Millhouse[108], J. C. Mills[112], E. Milotti[26,176], M. C. Milovich-Goff[116], O. Minazzoli[72,177], Y. Minenkov[34], A. Mishkin[31], C. Mishra[178], T. Mistry[120], S. Mitra[3], V. P. Mitrofanov[66], G. Mitselmakher[31], R. Mittleman[54], G. Mo[54], K. Mogushi[94], S. R. P. Mohapatra[54], S. R. Mohite[23], M. Molina-Ruiz[148], M. Mondin[116], M. Montani[70,71], C. J. Moore[13], D. Moraru[49], F. Morawski[62], G. Moreno[49], S. Morisaki[90], B. Mours[179], C. M. Mow-Lowry[13], S. Mozzon[129], F. Muciaccia[35,126], Arunava Mukherjee[53], D. Mukherjee[131], S. Mukherjee[16], Subroto Mukherjee[118], N. Mukund[9,10], A. Mullavey[7], J. Munch[63], E. A. Muñiz[44], P. G. Murray[53], A. Nagar[96,138,180], I. Nardecchia[34,93], L. Naticchioni[35,126], R. K. Nayak[181], B. F. Neil[73], J. Neilson[75,123], G. Nelemans[39,182], T. J. N. Nelson[7], M. Nery[9,10], A. Neunzert[146], K. Y. Ng[54], S. Ng[63], C. Nguyen[27], P. Nguyen[78], D. Nichols[39,143], S. A. Nichols[2], S. Nissanke[39,143], F. Nocera[30], M. Noh[54], C. North[112], D. Nothard[183], L. K. Nuttall[129], J. Oberling[49], B. D. O'Brien[31], G. Oganesyan[17,18], G. H. Ogin[184], J. J. Oh[158], S. H. Oh[158], F. Ohme[9,10], H. Ohta[90], M. A. Okada[15], M. Oliver[109], C. Olivetto[30], P. Oppermann[9,10], Richard J. Oram[7], B. O'Reilly[7], R. G. Ormiston[46], L. F. Ortega[31], R. O'Shaughnessy[68], S. Ossokine[83], C. Osthelder[1], D. J. Ottaway[63], H. Overmier[7], B. J. Owen[92], A. E. Pace[131], G. Pagano[21,57], M. A. Page[73], G. Pagliaroli[17,18], A. Pai[139], S. A. Pai[65], J. R. Palamos[78], O. Palashov[155], C. Palomba[35], H. Pan[97], P. K. Panda[150], P. T. H. Pang[39], C. Pankow[14], F. Pannarale[35,126], B. C. Pant[65], F. Paoletti[21], A. Paoli[30], A. Parida[3], W. Parker[7,174], D. Pascucci[39,53], A. Pasqualetti[30], R. Passaquieti[21,57], D. Passuello[21], B. Patricelli[21,57], E. Payne[6], B. L. Pearlstone[53], T. C. Pechsiri[31], A. J. Pedersen[44], M. Pedraza[1], A. Pele[7], S. Penn[185], A. Perego[124,125], C. J. Perez[49], C. Périgois[36], A. Perreca[124,125], S. Perriès[104], J. Petermann[117], H. P. Pfeiffer[83],

M. Phelps[9,10], K. S. Phukon[3,39,167], O. J. Piccinni[35,126], M. Pichot[72], M. Piendibene[21,57], F. Piergiovanni[70,71], V. Pierro[75,123], G. Pillant[30], L. Pinard[22], I. M. Pinto[75,96,123], K. Piotrzkowski[80], M. Pirello[49], M. Pitkin[186], W. Plastino[170,171], R. Poggiani[21,57], D. Y. T. Pong[102], S. Ponrathnam[3], P. Popolizio[30], E. K. Porter[27], J. Powell[187], A. K. Prajapati[118], K. Prasai[56], R. Prasanna[150], G. Pratten[13], T. Prestegard[23], M. Principe[75,96,123], G. A. Prodi[124,125], L. Prokhorov[13], M. Punturo[43], P. Puppo[35], M. Pürrer[83], H. Qi[112], V. Quetschke[16], P. J. Quinonez[37], F. J. Raab[49], G. Raaijmakers[39,143], H. Radkins[49], N. Radulesco[72], P. Raffai[115], H. Rafferty[188], S. Raja[65], C. Rajan[65], B. Rajbhandari[92], M. Rakhmanov[16], K. E. Ramirez[16], A. Ramos-Buades[109], Javed Rana[3], K. Rao[14], P. Rapagnani[35,126], V. Raymond[112], M. Razzano[21,57], J. Read[28], T. Regimbau[36], L. Rei[64], S. Reid[24], D. H. Reitze[1,31], P. Rettegno[138,189], F. Ricci[35,126], C. J. Richardson[37], J. W. Richardson[1], P. M. Ricker[20], G. Riemenschneider[138,189], K. Riles[146], M. Rizzo[14], N. A. Robertson[1,53], F. Robinet[29], A. Rocchi[34], R. D. Rodriguez-Soto[37], L. Rolland[36], J. G. Rollins[1], V. J. Roma[78], M. Romanelli[77], R. Romano[4,5], C. L. Romel[49], I. M. Romero-Shaw[6], J. H. Romie[7], C. A. Rose[23], D. Rose[28], K. Rose[183], D. Rosińska[81], S. G. Rosofsky[20], M. P. Ross[169], S. Rowan[53], S. J. Rowlinson[13], P. K. Roy[16], Santosh Roy[3], Soumen Roy[190], P. Ruggi[30], G. Rutins[67], K. Ryan[49], S. Sachdev[131], T. Sadecki[49], M. Sakellariadou[152], O. S. Salafia[47,48,191], L. Salconi[30], M. Saleem[32], A. Samajdar[39], E. J. Sanchez[1], L. E. Sanchez[1], N. Sanchis-Gual[192], J. R. Sanders[193], K. A. Santiago[38], E. Santos[72], N. Sarin[6], B. Sassolas[22], B. S. Sathyaprakash[112,131], O. Sauter[36], R. L. Savage[49], V. Savant[3], D. Sawant[139], S. Sayah[22], D. Schaetzl[1], P. Schale[78], M. Scheel[50], J. Scheuer[14], P. Schmidt[13], R. Schnabel[117], R. M. S. Schofield[78], A. Schönbeck[117], E. Schreiber[9,10], B. W. Schulte[9,10], B. F. Schutz[112], O. Schwarm[184], E. Schwartz[7], J. Scott[53], S. M. Scott[8], E. Seidel[20], D. Sellers[7], A. S. Sengupta[190], N. Sennett[83], D. Sentenac[30], V. Sequino[64], A. Sergeev[155], Y. Setyawati[9,10], D. A. Shaddock[8], T. Shaffer[49], M. S. Shahriar[14], S. Sharifi[2], A. Sharma[17,18], P. Sharma[65], P. Shawhan[84], H. Shen[20], M. Shikauchi[90], R. Shink[164], D. H. Shoemaker[54], D. M. Shoemaker[85], K. Shukla[148], S. ShyamSundar[65], K. Siellez[85], M. Sieniawska[62], D. Sigg[49], L. P. Singer[88], D. Singh[131], N. Singh[81], A. Singha[53], A. Singhal[17,35], A. M. Sintes[109], V. Sipala[127,128], V. Skliris[112], B. J. J. Slagmolen[8], T. J. Slaven-Blair[73], J. Smetana[13], J. R. Smith[28], R. J. E. Smith[6], S. Somala[194], E. J. Son[158], S. Soni[2], B. Sorazu[53], V. Sordini[104], F. Sorrentino[64], T. Souradeep[3], E. Sowell[92], A. P. Spencer[53], M. Spera[59,60], A. K. Srivastava[118], V. Srivastava[44], K. Staats[14], C. Stachie[72], M. Standke[9,10], D. A. Steer[27], M. Steinke[9,10], J. Steinlechner[53,117], S. Steinlechner[117], D. Steinmeyer[9,10], S. Stevenson[187], D. Stocks[56], D. J. Stops[13], M. Stover[183], K. A. Strain[53], G. Stratta[71,195], A. Strunk[49], R. Sturani[196], A. L. Stuver[197], S. Sudhagar[3], V. Sudhir[54], T. Z. Summerscales[198], L. Sun[1], S. Sunil[118], A. Sur[62], J. Suresh[90], P. J. Sutton[112], B. L. Swinkels[39], M. J. Szczepańczyk[31], M. Tacca[39], S. C. Tait[53], C. Talbot[6], A. J. Tanasijczuk[80], D. B. Tanner[31], D. Tao[1], M. Tápai[140], A. Tapia[28], E. N. Tapia San Martin[39], J. D. Tasson[199], R. Taylor[1], R. Tenorio[109], L. Terkowski[117], M. P. Thirugnanasambandam[3], M. Thomas[7], P. Thomas[49], J. E. Thompson[112], S. R. Thondapu[65], K. A. Thorne[7], E. Thrane[6], C. L. Tinsman[6], T. R. Saravanan[3], Shubhanshu Tiwari[76,124,125], S. Tiwari[144], V. Tiwari[112], K. Toland[53], M. Tonelli[21,57], Z. Tornasi[53], A. Torres-Forné[83], C. I. Torrie[1], I. Tosta e Melo[127,128], D. Töyrä[8], E. A. Trail[2], F. Travasso[43,58], G. Traylor[7], M. C. Tringali[81], A. Tripathee[146], A. Trovato[27], R. J. Trudeau[1], K. W. Tsang[39], M. Tse[54], R. Tso[50], L. Tsukada[90], D. Tsuna[90], T. Tsutsui[90], M. Turconi[72], A. S. Ubhi[13], R. Udall[85], K. Ueno[90], D. Ugolini[188], C. S. Unnikrishnan[144], A. L. Urban[2], S. A. Usman[101], A. C. Utina[53], H. Vahlbruch[10], G. Vajente[1], G. Valdes[2], M. Valentini[124,125], N. van Bakel[39], M. van Beuzekom[39], J. F. J. van den Brand[39,82,149], C. Van Den Broeck[39,200], D. C. Vander-Hyde[44], L. van der Schaaf[39], J. V. Van Heijningen[73], A. A. van Veggel[53], M. Vardaro[39,167], V. Varma[50], S. Vass[1], M. Vasúth[55], A. Vecchio[13], G. Vedovato[60], J. Veitch[53], P. J. Veitch[63], K. Venkateswara[169], G. Venugopalan[1], D. Verkindt[36], D. Veske[33], F. Vetrano[70,71], A. Viceré[70,71], A. D. Viets[201], S. Vinciguerra[13], D. J. Vine[67], J.-Y. Vinet[72], S. Vitale[54], Francisco Hernandez Vivanco[6], T. Vo[44], H. Vocca[42,43], C. Vorvick[49], S. P. Vyatchanin[66], A. R. Wade[8], L. E. Wade[183], M. Wade[183], R. Walet[39], M. Walker[28], G. S. Wallace[24], L. Wallace[1], S. Walsh[23], J. Z. Wang[146], S. Wang[20], W. H. Wang[16], R. L. Ward[8], Z. A. Warden[37], J. Warner[49], M. Was[36], J. Watchi[110], B. Weaver[49], L.-W. Wei[9,10], M. Weinert[9,10], A. J. Weinstein[1], R. Weiss[54], F. Wellmann[9,10], L. Wen[73], P. Weßels[9,10], J. W. Westhouse[37], K. Wette[8], J. T. Whelan[68], B. F. Whiting[31], C. Whittle[54], D. M. Wilken[9,10], D. Williams[53], J. L. Willis[1], B. Willke[9,10], W. Winkler[9,10], C. C. Wipf[1], H. Wittel[9,10], G. Woan[53], J. Woehler[9,10], J. K. Wofford[68], C. Wong[102], J. L. Wright[53], D. S. Wu[9,10], D. M. Wysocki[68], L. Xiao[1], H. Yamamoto[1], L. Yang[132], Y. Yang[31], Z. Yang[46], M. J. Yap[8], M. Yazback[31], D. W. Yeeles[112], Hang Yu[54], Haocun Yu[54], S. H. R. Yuen[102], A. K. Zadrożny[16], A. Zadrożny[161], M. Zanolin[37], T. Zelenova[30], J.-P. Zendri[60], M. Zevin[14], J. Zhang[73], L. Zhang[1], T. Zhang[53], C. Zhao[73], G. Zhao[110], M. Zhou[14], Z. Zhou[14], X. J. Zhu[6], A. B. Zimmerman[175], Y. Zlochower[68], M. E. Zucker[1,54], and J. Zweizig[1]

LIGO Scientific Collaboration and Virgo Collaboration

[1] LIGO, California Institute of Technology, Pasadena, CA 91125, USA
[2] Louisiana State University, Baton Rouge, LA 70803, USA
[3] Inter-University Centre for Astronomy and Astrophysics, Pune 411007, India
[4] Dipartimento di Farmacia, Università di Salerno, I-84084 Fisciano, Salerno, Italy
[5] INFN, Sezione di Napoli, Complesso Universitario di Monte S.Angelo, I-80126 Napoli, Italy
[6] OzGrav, School of Physics & Astronomy, Monash University, Clayton 3800, Victoria, Australia
[7] LIGO Livingston Observatory, Livingston, LA 70754, USA
[8] OzGrav, Australian National University, Canberra, Australian Capital Territory 0200, Australia
[9] Max Planck Institute for Gravitational Physics (Albert Einstein Institute), D-30167 Hannover, Germany
[10] Leibniz Universität Hannover, D-30167 Hannover, Germany
[11] Theoretisch-Physikalisches Institut, Friedrich-Schiller-Universität Jena, D-07743 Jena, Germany
[12] University of Cambridge, Cambridge CB2 1TN, UK
[13] University of Birmingham, Birmingham B15 2TT, UK
[14] Center for Interdisciplinary Exploration & Research in Astrophysics (CIERA), Northwestern University, Evanston, IL 60208, USA

[15] Instituto Nacional de Pesquisas Espaciais, 12227-010 São José dos Campos, São Paulo, Brazil
[16] The University of Texas Rio Grande Valley, Brownsville, TX 78520, USA
[17] Gran Sasso Science Institute (GSSI), I-67100 L'Aquila, Italy
[18] INFN, Laboratori Nazionali del Gran Sasso, I-67100 Assergi, Italy
[19] International Centre for Theoretical Sciences, Tata Institute of Fundamental Research, Bengaluru 560089, India
[20] NCSA, University of Illinois at Urbana-Champaign, Urbana, IL 61801, USA
[21] INFN, Sezione di Pisa, I-56127 Pisa, Italy
[22] Laboratoire des Matériaux Avancés (LMA), IP2I—UMR 5822, CNRS, Université de Lyon, F-69622 Villeurbanne, France
[23] University of Wisconsin-Milwaukee, Milwaukee, WI 53201, USA
[24] SUPA, University of Strathclyde, Glasgow G1 1XQ, UK
[25] Dipartimento di Matematica e Informatica, Università di Udine, I-33100 Udine, Italy
[26] INFN, Sezione di Trieste, I-34127 Trieste, Italy
[27] APC, AstroParticule et Cosmologie, Université Paris Diderot, CNRS/IN2P3, CEA/Irfu, Observatoire de Paris, Sorbonne Paris Cité, F-75205 Paris Cedex 13, France
[28] California State University Fullerton, Fullerton, CA 92831, USA
[29] LAL, Univ. Paris-Sud, CNRS/IN2P3, Université Paris-Saclay, F-91898 Orsay, France
[30] European Gravitational Observatory (EGO), I-56021 Cascina, Pisa, Italy
[31] University of Florida, Gainesville, FL 32611, USA
[32] Chennai Mathematical Institute, Chennai 603103, India
[33] Columbia University, New York, NY 10027, USA
[34] INFN, Sezione di Roma Tor Vergata, I-00133 Roma, Italy
[35] INFN, Sezione di Roma, I-00185 Roma, Italy
[36] Laboratoire d'Annecy de Physique des Particules (LAPP), Univ. Grenoble Alpes, Université Savoie Mont Blanc, CNRS/IN2P3, F-74941 Annecy, France
[37] Embry-Riddle Aeronautical University, Prescott, AZ 86301, USA
[38] Montclair State University, Montclair, NJ 07043, USA
[39] Nikhef, Science Park 105, 1098 XG Amsterdam, The Netherlands
[40] Korea Institute of Science and Technology Information, Daejeon 34141, Republic of Korea
[41] Christopher Newport University, Newport News, VA 23606, USA
[42] Università di Perugia, I-06123 Perugia, Italy
[43] INFN, Sezione di Perugia, I-06123 Perugia, Italy
[44] Syracuse University, Syracuse, NY 13244, USA
[45] Université de Liège, B-4000 Liège, Belgium
[46] University of Minnesota, Minneapolis, MN 55455, USA
[47] Università degli Studi di Milano-Bicocca, I-20126 Milano, Italy
[48] INFN, Sezione di Milano-Bicocca, I-20126 Milano, Italy
[49] LIGO Hanford Observatory, Richland, WA 99352, USA
[50] Caltech CaRT, Pasadena, CA 91125, USA
[51] Departament de Física Quàntica i Astrofísica, Institut de Ciències del Cosmos (ICCUB), Universitat de Barcelona (IEEC-UB), E-08028 Barcelona, Spain
[52] Dipartimento di Medicina, Chirurgia e Odontoiatria "Scuola Medica Salernitana," Università di Salerno, I-84081 Baronissi, Salerno, Italy
[53] SUPA, University of Glasgow, Glasgow G12 8QQ, UK
[54] LIGO, Massachusetts Institute of Technology, Cambridge, MA 02139, USA
[55] Wigner RCP, RMKI, H-1121 Budapest, Konkoly Thege Miklós út 29-33, Hungary
[56] Stanford University, Stanford, CA 94305, USA
[57] Università di Pisa, I-56127 Pisa, Italy
[58] Università di Camerino, Dipartimento di Fisica, I-62032 Camerino, Italy
[59] Università di Padova, Dipartimento di Fisica e Astronomia, I-35131 Padova, Italy
[60] INFN, Sezione di Padova, I-35131 Padova, Italy
[61] Montana State University, Bozeman, MT 59717, USA
[62] Nicolaus Copernicus Astronomical Center, Polish Academy of Sciences, 00-716, Warsaw, Poland
[63] OzGrav, University of Adelaide, Adelaide, South Australia 5005, Australia
[64] INFN, Sezione di Genova, I-16146 Genova, Italy
[65] RRCAT, Indore, Madhya Pradesh 452013, India
[66] Faculty of Physics, Lomonosov Moscow State University, Moscow 119991, Russia
[67] SUPA, University of the West of Scotland, Paisley PA1 2BE, UK
[68] Rochester Institute of Technology, Rochester, NY 14623, USA
[69] Bar-Ilan University, Ramat Gan 5290002, Israel
[70] Università degli Studi di Urbino "Carlo Bo," I-61029 Urbino, Italy
[71] INFN, Sezione di Firenze, I-50019 Sesto Fiorentino, Firenze, Italy
[72] Artemis, Université Côte d'Azur, Observatoire Côte d'Azur, CNRS, CS 34229, F-06304 Nice Cedex 4, France
[73] OzGrav, University of Western Australia, Crawley, Western Australia 6009, Australia
[74] Dipartimento di Fisica "E.R. Caianiello," Università di Salerno, I-84084 Fisciano, Salerno, Italy
[75] INFN, Sezione di Napoli, Gruppo Collegato di Salerno, Complesso Universitario di Monte S. Angelo, I-80126 Napoli, Italy
[76] Physik-Institut, University of Zurich, Winterthurerstrasse 190, 8057 Zurich, Switzerland
[77] Univ Rennes, CNRS, Institut FOTON—UMR6082, F-3500 Rennes, France
[78] University of Oregon, Eugene, OR 97403, USA
[79] Laboratoire Kastler Brossel, Sorbonne Université, CNRS, ENS-Université PSL, Collège de France, F-75005 Paris, France
[80] Université catholique de Louvain, B-1348 Louvain-la-Neuve, Belgium
[81] Astronomical Observatory Warsaw University, 00-478 Warsaw, Poland
[82] VU University Amsterdam, 1081 HV Amsterdam, The Netherlands
[83] Max Planck Institute for Gravitational Physics (Albert Einstein Institute), D-14476 Potsdam-Golm, Germany
[84] University of Maryland, College Park, MD 20742, USA
[85] School of Physics, Georgia Institute of Technology, Atlanta, GA 30332, USA
[86] Université de Lyon, Université Claude Bernard Lyon 1, CNRS, Institut Lumière Matière, F-69622 Villeurbanne, France
[87] Università di Napoli "Federico II," Complesso Universitario di Monte S.Angelo, I-80126 Napoli, Italy
[88] NASA Goddard Space Flight Center, Greenbelt, MD 20771, USA
[89] Dipartimento di Fisica, Università degli Studi di Genova, I-16146 Genova, Italy

[90] RESCEU, University of Tokyo, Tokyo, 113-0033, Japan
[91] Tsinghua University, Beijing 100084, People's Republic of China
[92] Texas Tech University, Lubbock, TX 79409, USA
[93] Università di Roma Tor Vergata, I-00133 Roma, Italy
[94] Missouri University of Science and Technology, Rolla, MO 65409, USA
[95] Departamento de Astronomía y Astrofísica, Universitat de València, E-46100 Burjassot, València, Spain
[96] Museo Storico della Fisica e Centro Studi e Ricerche "Enrico Fermi," I-00184 Roma, Italy
[97] National Tsing Hua University, Hsinchu City, 30013 Taiwan, Republic of China
[98] Charles Sturt University, Wagga Wagga, New South Wales 2678, Australia
[99] Physics and Astronomy Department, Stony Brook University, Stony Brook, NY 11794, USA
[100] Center for Computational Astrophysics, Flatiron Institute, 162 5th Ave., New York, NY 10010, USA
[101] University of Chicago, Chicago, IL 60637, USA
[102] The Chinese University of Hong Kong, Shatin, NT, Hong Kong
[103] Dipartimento di Ingegneria Industriale (DIIN), Università di Salerno, I-84084 Fisciano, Salerno, Italy
[104] Institut de Physique des 2 Infinis de Lyon (IP2I) - UMR 5822, Université de Lyon, Université Claude Bernard, CNRS, F-69622 Villeurbanne, France
[105] Seoul National University, Seoul 08826, Republic of Korea
[106] Pusan National University, Busan 46241, Republic of Korea
[107] INAF, Osservatorio Astronomico di Padova, I-35122 Padova, Italy
[108] OzGrav, University of Melbourne, Parkville, Victoria 3010, Australia
[109] Universitat de les Illes Balears, IAC3—IEEC, E-07122 Palma de Mallorca, Spain
[110] Université Libre de Bruxelles, Brussels 1050, Belgium
[111] Departamento de Matemáticas, Universitat de València, E-46100 Burjassot, València, Spain
[112] Cardiff University, Cardiff CF24 3AA, UK
[113] University of Rhode Island, Kingston, RI 02881, USA
[114] Bellevue College, Bellevue, WA 98007, USA
[115] MTA-ELTE Astrophysics Research Group, Institute of Physics, Eötvös University, Budapest 1117, Hungary
[116] California State University, Los Angeles, 5151 State University Dr., Los Angeles, CA 90032, USA
[117] Universität Hamburg, D-22761 Hamburg, Germany
[118] Institute for Plasma Research, Bhat, Gandhinagar 382428, India
[119] IGFAE, Campus Sur, Universidade de Santiago de Compostela, E-15782, Spain
[120] The University of Sheffield, Sheffield S10 2TN, UK
[121] Dipartimento di Scienze Matematiche, Fisiche e Informatiche, Università di Parma, I-43124 Parma, Italy
[122] INFN, Sezione di Milano Bicocca, Gruppo Collegato di Parma, I-43124 Parma, Italy
[123] Dipartimento di Ingegneria, Università del Sannio, I-82100 Benevento, Italy
[124] Università di Trento, Dipartimento di Fisica, I-38123 Povo, Trento, Italy
[125] INFN, Trento Institute for Fundamental Physics and Applications, I-38123 Povo, Trento, Italy
[126] Università di Roma "La Sapienza," I-00185 Roma, Italy
[127] Università degli Studi di Sassari, I-07100 Sassari, Italy
[128] INFN, Laboratori Nazionali del Sud, I-95125 Catania, Italy
[129] University of Portsmouth, Portsmouth, PO1 3FX, UK
[130] West Virginia University, Morgantown, WV 26506, USA
[131] The Pennsylvania State University, University Park, PA 16802, USA
[132] Colorado State University, Fort Collins, CO 80523, USA
[133] Institute for Nuclear Research (Atomki), Hungarian Academy of Sciences, Bem tér 18/c, H-4026 Debrecen, Hungary
[134] CNR-SPIN, c/o Università di Salerno, I-84084 Fisciano, Salerno, Italy
[135] Scuola di Ingegneria, Università della Basilicata, I-85100 Potenza, Italy
[136] National Astronomical Observatory of Japan, 2-21-1 Osawa, Mitaka, Tokyo 181-8588, Japan
[137] Observatori Astronòmic, Universitat de València, E-46980 Paterna, València, Spain
[138] INFN Sezione di Torino, I-10125 Torino, Italy
[139] Indian Institute of Technology Bombay, Powai, Mumbai 400 076, India
[140] University of Szeged, Dóm tér 9, Szeged 6720, Hungary
[141] Delta Institute for Theoretical Physics, Science Park 904, 1090 GL Amsterdam, The Netherlands
[142] Lorentz Institute, Leiden University, P.O. Box 9506, Leiden 2300 RA, The Netherlands
[143] GRAPPA, Anton Pannekoek Institute for Astronomy and Institute for High-Energy Physics, University of Amsterdam, Science Park 904, 1098 XH Amsterdam, The Netherlands
[144] Tata Institute of Fundamental Research, Mumbai 400005, India
[145] INAF, Osservatorio Astronomico di Capodimonte, I-80131 Napoli, Italy
[146] University of Michigan, Ann Arbor, MI 48109, USA
[147] American University, Washington, DC 20016, USA
[148] University of California, Berkeley, CA 94720, USA
[149] Maastricht University, P.O. Box 616, 6200 MD Maastricht, The Netherlands
[150] Directorate of Construction, Services & Estate Management, Mumbai 400094, India
[151] University of Białystok, 15-424 Białystok, Poland
[152] King's College London, University of London, London WC2R 2LS, UK
[153] University of Southampton, Southampton SO17 1BJ, UK
[154] University of Washington Bothell, Bothell, WA 98011, USA
[155] Institute of Applied Physics, Nizhny Novgorod, 603950, Russia
[156] Ewha Womans University, Seoul 03760, Republic of Korea
[157] Inje University Gimhae, South Gyeongsang 50834, Republic of Korea
[158] National Institute for Mathematical Sciences, Daejeon 34047, Republic of Korea
[159] Ulsan National Institute of Science and Technology, Ulsan 44919, Republic of Korea
[160] Bard College, 30 Campus Rd., Annandale-On-Hudson, NY 12504, USA
[161] NCBJ, 05-400 Świerk-Otwock, Poland
[162] Institute of Mathematics, Polish Academy of Sciences, 00656 Warsaw, Poland
[163] Cornell University, Ithaca, NY 14850, USA
[164] Université de Montréal/Polytechnique, Montreal, QC H3T 1J4, Canada

[165] Hillsdale College, Hillsdale, MI 49242, USA
[166] Korea Astronomy and Space Science Institute, Daejeon 34055, Republic of Korea
[167] Institute for High-Energy Physics, University of Amsterdam, Science Park 904, 1098 XH Amsterdam, The Netherlands
[168] NASA Marshall Space Flight Center, Huntsville, AL 35811, USA
[169] University of Washington, Seattle, WA 98195, USA
[170] Dipartimento di Matematica e Fisica, Università degli Studi Roma Tre, I-00146 Roma, Italy
[171] INFN, Sezione di Roma Tre, I-00146 Roma, Italy
[172] ESPCI, CNRS, F-75005 Paris, France
[173] Center for Phononics and Thermal Energy Science, School of Physics Science and Engineering, Tongji University, 200092 Shanghai, People's Republic of China
[174] Southern University and A&M College, Baton Rouge, LA 70813, USA
[175] Department of Physics, University of Texas, Austin, TX 78712, USA
[176] Dipartimento di Fisica, Università di Trieste, I-34127 Trieste, Italy
[177] Centre Scientifique de Monaco, 8 quai Antoine Ier, MC-98000, Monaco
[178] Indian Institute of Technology Madras, Chennai 600036, India
[179] Université de Strasbourg, CNRS, IPHC UMR 7178, F-67000 Strasbourg, France
[180] Institut des Hautes Etudes Scientifiques, F-91440 Bures-sur-Yvette, France
[181] IISER-Kolkata, Mohanpur, West Bengal 741252, India
[182] Department of Astrophysics/IMAPP, Radboud University Nijmegen, P.O. Box 9010, 6500 GL Nijmegen, The Netherlands
[183] Kenyon College, Gambier, OH 43022, USA
[184] Whitman College, 345 Boyer Avenue, Walla Walla, WA 99362 USA
[185] Hobart and William Smith Colleges, Geneva, NY 14456, USA
[186] Department of Physics, Lancaster University, Lancaster, LA1 4YB, UK
[187] OzGrav, Swinburne University of Technology, Hawthorn VIC 3122, Australia
[188] Trinity University, San Antonio, TX 78212, USA
[189] Dipartimento di Fisica, Università degli Studi di Torino, I-10125 Torino, Italy
[190] Indian Institute of Technology, Gandhinagar Ahmedabad Gujarat 382424, India
[191] INAF, Osservatorio Astronomico di Brera sede di Merate, I-23807 Merate, Lecco, Italy
[192] Centro de Astrofísica e Gravitação (CENTRA), Departamento de Física, Instituto Superior Técnico, Universidade de Lisboa, 1049-001 Lisboa, Portugal
[193] Marquette University, 11420 W. Clybourn St., Milwaukee, WI 53233, USA
[194] Indian Institute of Technology Hyderabad, Sangareddy, Khandi, Telangana 502285, India
[195] INAF, Osservatorio di Astrofisica e Scienza dello Spazio, I-40129 Bologna, Italy
[196] International Institute of Physics, Universidade Federal do Rio Grande do Norte, Natal RN 59078-970, Brazil
[197] Villanova University, 800 Lancaster Ave., Villanova, PA 19085, USA
[198] Andrews University, Berrien Springs, MI 49104, USA
[199] Carleton College, Northfield, MN 55057, USA
[200] Department of Physics, Utrecht University, 3584CC Utrecht, The Netherlands
[201] Concordia University Wisconsin, 2800 N. Lake Shore Dr., Mequon, WI 53097, USA
Received 2020 June 3; revised 2020 July 6; accepted 2020 July 9; published 2020 September 2

Abstract

The gravitational-wave signal GW190521 is consistent with a binary black hole (BBH) merger source at redshift 0.8 with unusually high component masses, $85^{+21}_{-14}\,M_{\odot}$ and $66^{+17}_{-18}\,M_{\odot}$, compared to previously reported events, and shows mild evidence for spin-induced orbital precession. The primary falls in the mass gap predicted by (pulsational) pair-instability supernova theory, in the approximate range 65–120 $M_{\odot}$. The probability that at least one of the black holes in GW190521 is in that range is 99.0%. The final mass of the merger ($142^{+28}_{-16}\,M_{\odot}$) classifies it as an intermediate-mass black hole. Under the assumption of a quasi-circular BBH coalescence, we detail the physical properties of GW190521's source binary and its post-merger remnant, including component masses and spin vectors. Three different waveform models, as well as direct comparison to numerical solutions of general relativity, yield consistent estimates of these properties. Tests of strong-field general relativity targeting the merger-ringdown stages of the coalescence indicate consistency of the observed signal with theoretical predictions. We estimate the merger rate of similar systems to be $0.13^{+0.30}_{-0.11}$ Gpc^{-3} yr^{-1}. We discuss the astrophysical implications of GW190521 for stellar collapse and for the possible formation of black holes in the pair-instability mass gap through various channels: via (multiple) stellar coalescences, or via hierarchical mergers of lower-mass black holes in star clusters or in active galactic nuclei. We find it to be unlikely that GW190521 is a strongly lensed signal of a lower-mass black hole binary merger. We also discuss more exotic possible sources for GW190521, including a highly eccentric black hole binary, or a primordial black hole binary.

Unified Astronomy Thesaurus concepts: Astrophysical black holes (98); High energy astrophysics (739); Gravitational collapse (662); Gravitation (661); Gravitational wave astronomy (675); Gravitational wave sources (677); LIGO (920); Stellar mass black holes (611); Stellar populations (1622); Intermediate-mass black holes (816)

1. Introduction

The gravitational-wave (GW) signal GW190521 (Abbott et al. 2020b, 2019b) was observed by the Advanced LIGO (Aasi et al. 2015) and Advanced Virgo (Acernese et al. 2015) detectors during their third observing run (O3). The event was found with four different search pipelines, both at low latency and offline with improved background estimation; an offline search sensitive to generic transients found GW190521 with a three-detector network signal-to-noise ratio (S/N) of 14.7 and an estimated false-alarm rate of 1 in 4900 yr (Abbott et al. 2020b). Another candidate GW signal was reported later on the same day (Abbott et al. 2019c). The source of GW190521 is

consistent with being a high-mass binary black hole (BBH) system. The final merger product of GW190521, with an estimated mass of $142^{+28}_{-16}\,M_\odot$ (all values quoted as medians with symmetric 90% credible interval), is the first strong observational evidence for an intermediate-mass BH (IMBH) in the mass range 10^2–$10^3\,M_\odot$, under the assumption of a quasi-circular BBH coalescence. This merger of two high-mass BHs (primary mass $85^{+21}_{-14}\,M_\odot$, secondary mass $66^{+17}_{-18}\,M_\odot$) is also exceptional as the first observation of a BH that lies with high confidence in the mass gap predicted by pair-instability (PI) supernova theory (Woosley 2017); the probability that the primary mass is below $65\,M_\odot$ is 0.3%. This high component mass represents a challenge for current astrophysical formation scenarios.

The very short duration (approximately 0.1 s) and bandwidth (around four cycles in the frequency band 30–80 Hz) of GW190521 means that the interpretation of the source as being a quasi-circular compact binary coalescence consisting of inspiral, merger, and ringdown phases is not certain. Under that interpretation, we find that the observed signal, including its frequency evolution, is entirely consistent both with three different waveform models derived from analytical and/or numerical solutions of general relativity (GR) and with direct comparisons to numerical relativity (NR) solutions. Therefore, most of the discussion in this paper and in Abbott et al. (2020b) proceeds under that assumption, including our inferences on the inferred masses and spins and on the effect of including higher-order multipoles in the waveform models. However, as discussed below, other interpretations are possible, adding to the exceptional nature of this event.

Searches for IMBH binaries with total mass $>100\,M_\odot$ and primary mass $\lesssim 500\,M_\odot$ were carried out in data from Initial LIGO and Virgo (Abadie et al. 2012; Aasi et al. 2014a) and from the first and second observing runs of the Advanced detector era, O1 and O2 (Abbott et al. 2017a, 2019d). However, no significant candidates were identified: see Udall et al. (2020) for further discussion. The most stringent upper limit on the local IMBH merger rate from O1 and O2 is $0.20\,\mathrm{Gpc^{-3}\,yr^{-1}}$ (in comoving units, 90% confidence level), for binaries with equal component masses $m_1 = m_2 = 100\,M_\odot$ (Abbott et al. 2019d). Other groups have also searched LIGO–Virgo open data (Abbott et al. 2018a, 2019e) for possible IMBH events (Nitz et al. 2019; Zackay et al. 2019). The O3 run started in 2019 April with significantly increased sensitivities for all three Advanced detectors compared to O1 and O2 (Acernese et al. 2019; Tse et al. 2019); here we consider the implications of GW190521, detected in the first half of the run, O3a (2019 April 1 through October 1).

1.1. Astrophysics of IMBHs

Observational evidence for IMBHs, usually defined as BHs with mass 10^2–$10^5\,M_\odot$ (see, e.g., Miller & Colbert 2004; van der Marel 2004) has long been sought. IMBHs bridge the gap between stellar BHs and supermassive BHs (SMBHs) and might be the missing link to explain the formation of SMBHs (Volonteri 2010; Greene et al. 2019). IMBHs are predicted to form in the early universe via direct collapse of very massive Population III stars ($\gtrsim 230\,M_\odot$; e.g., Fryer et al. 2001; Heger et al. 2003; Spera & Mapelli 2017) or through collapse of low angular momentum gas clouds (e.g., Loeb & Rasio 1994; Bromm & Loeb 2003; Begelman et al. 2006; Lodato & Natarajan 2006), perhaps passing through a quasi-star phase (e.g., Begelman 2010; Ball et al. 2011). In stellar clusters, IMBHs are predicted to form via dynamical channels such as runaway collisions (Portegies Zwart & McMillan 2002; Gurkan et al. 2004; Portegies Zwart et al. 2004) and hierarchical mergers of smaller BHs (Miller & Hamilton 2002; O'Leary et al. 2006; Giersz et al. 2015), especially in metal-poor star clusters (Mapelli 2016). However, there is no conclusive observational confirmation of IMBHs in globular clusters and other massive star clusters (Gerssen et al. 2002; Gebhardt et al. 2005; Noyola et al. 2008; Anderson & van der Marel 2010; van der Marel & Anderson 2010; Lützgendorf et al. 2011, 2013; Miller-Jones et al. 2012; Nyland et al. 2012; Strader et al. 2012; Lanzoni et al. 2013; Kızıltan et al. 2017; Perera et al. 2017; Lin et al. 2018; Tremou et al. 2018; Baumgardt et al. 2019; Mann et al. 2019; Zocchi et al. 2019).

Several ultraluminous X-ray sources, defined as those with a total luminosity, assumed isotropic, of $\gtrsim 10^{39}\,\mathrm{erg\,s^{-1}}$, have been studied as IMBH candidates (Kaaret et al. 2001; Matsumoto et al. 2001; Strohmayer & Mushotzky 2003; Miller & Colbert 2004; van der Marel 2004; Feng & Soria 2011; Sutton et al. 2012; Mezcua et al. 2015; Mezcua 2017; Wang et al. 2015; Kaaret et al. 2017; Lin et al. 2020), but only a few still support evidence for IMBHs. HLX-1 is possibly the strongest IMBH candidate from electromagnetic data (Farrell et al. 2009; Godet et al. 2009; Servillat et al. 2011; Soria et al. 2012; Webb et al. 2012; Cseh et al. 2015), pointing to an IMBH mass of $\sim(0.3\text{–}30)\times 10^4\,M_\odot$.

Several IMBH candidates lie at the centers of dwarf galaxies and are associated with low-luminosity active galactic nuclei (AGNs; Filippenko & Sargent 1989; Filippenko & Ho 2003; Barth et al. 2004, 2005; Greene & Ho 2004, 2007; Seth et al. 2010; Dong et al. 2012; Reines et al. 2013; Baldassare et al. 2015, 2016, 2017; den Brok et al. 2015; Mezcua et al. 2016, 2018). Their estimated masses are close to (or above) the upper edge of the IMBH mass range. The final mass of GW190521 is close to the lower end of the IMBH mass range, in an apparent BH desert covering the mass range of $\sim 10^2$–$10^3\,M_\odot$. Moreover, this final mass is the first confirmation that IMBHs can form through the merger of two less massive BHs.

1.2. Pair-instability Mass Gap

The mass of the primary component of GW190521 falls within the range where PI is expected to suppress BH formation. PI develops in a star when the effective production of electron–positron pairs in the stellar core softens the equation of state, removing pressure support (Woosley et al. 2007). This leads to a contraction of the core, raising the internal temperature up to the ignition of oxygen or silicon, and the star becomes unstable. PI is expected to develop in stars with helium-core mass $\gtrsim 32\,M_\odot$. For helium cores $32 \lesssim M_{\mathrm{He}}/M_\odot \lesssim 64$, this instability manifests as pulsational PI (PPI): the star undergoes a number of oscillations that eject material and remove the stellar envelope, bringing the star back to a stable configuration after the resulting mass loss (Barkat et al. 1967; Woosley et al. 2007; Chen et al. 2014; Yoshida et al. 2016). After PPI, the star ends its life with a core-collapse supernova (CCSN) or with direct collapse, leaving a compact object less massive than expected in the absence of PPI (Woosley 2017, 2019). For helium cores $64 \lesssim M_{\mathrm{He}}/M_\odot \lesssim 135$, PI leads to a complete disruption of the star, leaving no compact object, while for even larger helium cores PI drives a

direct collapse to a BH (Fowler & Hoyle 1964; Ober et al. 1983; Bond et al. 1984; Heger et al. 2003; Woosley et al. 2007).

The combined effect of PI and PPI is expected to carve a mass gap in the BH mass function, with lower boundary $\sim$40–65 $M_\odot$ and upper boundary $\gtrsim$120 $M_\odot$ (Heger et al. 2003; Belczynski et al. 2016; Spera & Mapelli 2017; Woosley 2017, 2019; Giacobbo et al. 2018). The boundaries of the mass gap are highly uncertain because they depend on stellar evolution and on our understanding of CCSNe, PPI supernovae, and PI supernovae (Farmer et al. 2019; Marchant et al. 2019; Stevenson et al. 2019; Mapelli et al. 2020). Several formation channels might populate the mass gap. Below, we will review these channels and attempt to interpret the astrophysical origin of GW190521 in this context and to put constraints on different scenarios.

1.3. Outline of the Paper

We describe the detection of GW190521 in a companion paper (Abbott et al. 2020b), where we detail the circumstances of the observation and the detection significance using three different search pipelines. The search results are consistent with a coherent astrophysical signal and inconsistent with an instrumental noise origin for the event. In addition, the strain data are consistent with GW emission from the coalescence of a quasi-circular compact binary system.

In this paper, we begin by assuming that the source is indeed the coalescence of such a binary. In Section 2, we give further details about the Bayesian parameter estimation procedure and the posterior probability distributions that provide estimates of the source's intrinsic and extrinsic parameters. We quantify the evidence for orbital precession due to in-plane component spins and the evidence for the presence of higher-order multipoles beyond the dominant $\ell = 2$, $m = 2$ mode in the data.

In Section 3, we discuss the consistency of the observed signal with the coalescence of a quasi-circular compact binary system. We test the consistency of the residual data, after subtraction of the best-fitting signal, with detector noise, as well as the consistency of the merger and ringdown portions of the signal with expectations from waveform models derived from GR.

In Section 4, we present an estimate of the rate per comoving volume for merger events similar to GW190521. In Section 5, we consider the astrophysical implications of the observation, discussing uncertainties on the PI mass gap and proposed astrophysical channels that might populate the mass gap, including hierarchical merger in stellar cluster environments and stellar mergers. In Section 6, we discuss alternative scenarios for the source of GW190521, including a strongly gravitationally lensed merger, an eccentric BBH, or a primordial BBH; we also exclude a cosmic string cusp or kink or a CCSN as possible sources owing to mismatch with the GW data. Finally, we summarize our observations and consider future prospects in Section 7.

2. Source Properties

Under the assumption that GW190521 is a quasi-circular BBH coalescence, the intrinsic parameters of the source are fully described by the masses, m_1 and m_2, and the spin vectors, $\boldsymbol{S}_1$ and $\boldsymbol{S}_2$, of the two BHs. We use the convention that $m_1 \geqslant m_2$ and the mass ratio $q = m_2/m_1 \leqslant 1$. The dimensionless spin magnitudes, $\chi_i = |c\,\boldsymbol{S}_i/(Gm_i^2)|$, are assumed to be constant throughout the inspiral, while the spin orientations relative to the orbital angular momentum axis, $\theta_{\mathrm{LS}_i} = \arccos(\hat{\boldsymbol{L}} \cdot \hat{\boldsymbol{S}}_i) \in [0, 180^\circ]$, evolve over the duration of the signal. The spin orientations must therefore be parameterized at some fiducial time, which, for this work, is when the signal has a GW frequency $f_0 = 11$ Hz. The remnant BH produced from post-merger is described by its mass M_f and spin magnitude χ_f. We also estimate the BH recoil velocity $v_\mathrm{f} = |\boldsymbol{v}_\mathrm{f}|$ relative to the center of mass of the binary.

As discussed in Section 2.4 below, the source is estimated to be cosmologically distant. The masses measured in the frame of LIGO and Virgo detectors are therefore redshifted by a factor $(1 + z)$ and are denoted with a superscript "det" so that $m^{\mathrm{det}} = (1 + z)m$, where m is the source-frame mass. GWs directly encode the luminosity distance to the source D_L, which in turn depends on the inclination angle of the binary orbit with respect to the line of sight (Section 2.4). To make inferences about the source-frame masses, we must therefore convert the distance measurement to a redshift. The statistical uncertainty associated with estimation of the source-frame masses is increased relative to that of the detector-frame masses owing to these dependencies. From the inferred posterior distribution of D_L we compute redshift assuming a Planck 2015 ΛCDM cosmology with Hubble parameter $H_0 = 67.9\,\mathrm{km\,s^{-1}\,Mpc^{-1}}$ (Ade et al. 2016) (and we address the effect of taking a larger value of the Hubble parameter in Section 2.2). Unless stated otherwise, mass measurements are quoted in the source frame of the binary.

2.1. Method and Signal Models

To infer the source properties of GW190521, we analyzed 8 s of data in the LIGO and Virgo detectors around the time of the detection. The data are downsampled from 16,384 to 1024 Hz, as we expect no signal power above several hundred Hz owing to the total mass of GW190521. The parameter estimation analysis is done with two independently developed coherent Bayesian inference pipelines, `LALInference` (Veitch et al. 2015) and `RIFT` (Lange et al. 2018; Wysocki et al. 2019), which produce consistent results for the inferred source parameters. Both parameter estimation algorithms assume stationary Gaussian noise characterized by the power spectral density (PSD), which is inferred from the data by the `BayesLine` algorithm (Littenberg & Cornish 2015). We compute the event likelihood in the frequency domain, integrating over the frequency band 11–512 Hz.

We used three distinct GW signal models of BBH coalescence in our analysis: `NRSur7dq4` (NRSur PHM), a surrogate waveform model built by directly interpolating NR solutions (Varma et al. 2019); `IMRPhenomPv3HM` (Phenom PHM), an inspiral-merger-ringdown waveform model that uses phenomenological frequency domain fits combining post-Newtonian calculations of the GW phase and amplitude (Blanchet et al. 1995, 2005; Damour et al. 2001; Arun et al. 2009; Blanchet 2014) with tuning to NR solutions (Khan et al. 2020); and `SEOBNRv4PHM` (SEOBNR PHM), an inspiral-merger-ringdown waveform model that is based on the effective-one-body formalism (Buonanno & Damour 1999, 2000) and calibrated to NR (Ossokine et al. 2020).

These three waveform models employ different approaches to reproduce the predictions from analytical relativity and numerical relativity; we expect to see differences in the parameter estimation from these three models as a result of those different approaches, and we can interpret those differences as a form of

systematic error associated with the modeling. Note that the effects of the astrophysical environment, such as the presence of gas, on the GW waveform are expected to be negligible (Fedrow et al. 2017) in the late stages of inspiral, merger, and ringdown that we observe.

NRSur PHM is constructed based on NR simulations with component spins that are not constrained to be aligned with the orbital axis, thus including the effects of spin–orbit precession. The model covers dimensionless spin magnitudes $\chi_i \leqslant 0.8$ and mass ratios $q = m_2/m_1 \geqslant 1/4$. It includes all $(l, |m|)$-multipoles of the gravitational radiation (Blanchet et al. 1996, 2008; Kidder 2008; Mishra et al. 2016) up to and including $l = 4$. In the training parameter space, the waveform model has shown excellent agreement with NR simulations, with mismatches comparable to the numerical errors associated with the NR simulation. The model continues to agree with NR when extrapolating to mass ratios $q \geqslant 1/6$ (Varma et al. 2019). NRSur PHM is directly trained with NR simulations and therefore only models the last ∼20 orbits of the inspiral, which is adequate for GW190521 because the signal is in the measurement band of the detectors for fewer cycles.

Phenom PHM (Khan et al. 2019) is an approximate higher-multipole aligned-spin waveform model that maps the subdominant radiative moments $(l, |m|) = (2, 1), (3, 2), (3, 3), (4, 3), (4, 4)$ to the dominant (2, 2) mode (London et al. 2018). Multipoles are defined in the co-precessing frame, where the binary approximates a system with aligned spins (Schmidt et al. 2011; Pekowsky et al. 2013), and are then transformed by a time-dependent rotation to model the harmonic modes of a precessing binary in the inertial frame (Schmidt et al. 2012; Hannam et al. 2014), using a double-spin model of spin–orbit precession during the inspiral (Chatziioannou et al. 2017). After this precession "twisting," all $l \leqslant 4$ modes will be nonzero in the inertial frame. The nonprecessing, dominant multipole of the radiation is tuned to spin-aligned NR simulations in the parameter space of spin magnitudes $\chi_i \leqslant 0.85$ and mass ratios $q \geqslant 1/18$ (Husa et al. 2016; Khan et al. 2016). The subdominant multipoles and precessional effects in Phenom PHM, however, have not been calibrated to NR, and the model does not include spherical−spheroidal mode-mixing effects, which can significantly impact some of the higher multipoles (Kelly & Baker 2013).

SEOBNR PHM is based on the dynamics of spinning, nonprecessing BBHs in the effective-one-body formalism, calibrated to NR simulations and results from BH perturbation theory (Bohé et al. 2017). The model includes the nonprecessing $(l, |m|) = (2, 1), (3, 3), (4, 4), (5, 5)$ multipoles in addition to the dominant (2, 2) multipole mode. The individual modes are calibrated to waveforms from NR and BH perturbation theory (Cotesta et al. 2018), covering the parameter space of mass ratios $q \geqslant 1/10$ and effective inspiral spin parameter $\chi_{\rm eff} \in [-0.7, 0.85]$. Effects from the precessing orbital plane are modeled through a suitable rotation of the nonprecessing inspiral-plunge multipoles from the co-precessing frame to the inertial frame (without recalibration to NR), with a direct attachment of merger-ringdown modes in the co-precessing frame (Babak et al. 2017; Ossokine et al. 2020). After the precession twisting, all $l \leqslant 5$ modes will be nonzero in the inertial frame.

Although not directly fitted to NR simulations of precessing binaries, both Phenom PHM and SEOBNR PHM have been validated through a comparison with a large set of such NR waveforms (Khan et al. 2020; Ossokine et al. 2020). The three models described above are tuned to different NR solutions. Comparisons between different NR codes find agreement on the level of accuracy of the individual codes (Hannam et al. 2009; Hinder et al. 2014; Lovelace et al. 2016). The agreement between different NR codes is sufficiently good (Pürrer & Haster 2020) to avoid systematic biases at the S/N of GW190521. However, The three models are constructed in sufficiently different ways that it is useful to compare the results of parameter estimation from each of them.

The NRSur PHM waveform model is most faithful to NR simulations in the parameter range relevant for GW190521 (Varma et al. 2019). Therefore, the inferred source parameters quoted in this paper and in Abbott et al. (2020b) were obtained with the NRSur PHM model unless otherwise noted. In this section we also present results from the Phenom PHM and SEOBNR PHM models to check for systematic differences between waveform models. As shown below, differences in results between waveform models are of the same order as or smaller than the statistical error and do not impact the astrophysical interpretation of GW190521 discussed in this paper.

We choose priors that are uniform on the component masses in the detector frame from [30, 200] $M_\odot$. We further restrict the mass priors such that the total mass must be greater than 200 $M_\odot$ and the chirp mass to be between 70 and 150 $M_\odot$, both in the detector frame. In all cases, we verify that the posterior distributions do not have support at the boundaries of the priors. The distance prior scales as $D_{\rm L}^2$ (i.e., differential in Euclidean volume) up to a maximum of 10 Gpc. We have checked that a prior that is differential in comoving volume (with Planck 2015 cosmology) makes negligible (<1%) difference in the posterior medians for all source parameters. For the BH spins, we adopt a uniform prior for the magnitude in the dimensionless parameters $\chi_i \in [0, 0.99]$ and their orientation angles chosen to be uniform on the surface of the unit sphere. We adopt a uniform prior in the cosine of the inclination angle between the binary angular momentum and the line of sight, $\theta_{\rm JN}$. The prior on the sky location (R.A. and decl.) is chosen to be uniform on the surface of the unit sphere.

The parameters of the remnant BH formed after the merger, its mass $M_{\rm f}$, dimensionless spin $\chi_{\rm f}$, and recoil kick velocity $v_{\rm f}$, are inferred by applying fits calibrated to NR to the posterior distributions of the binary's initial masses and spins. For the posteriors from the Phenom PHM and SEOBNR PHM waveform models, we used the same $M_{\rm f}$ and $\chi_{\rm f}$ fits that are implemented internally in these models: for Phenom PHM, the fits from Husa et al. (2016) with corrections for precession from Bohé et al. (2016), and for SEOBNR PHM, the fits from Ossokine et al. (2020) and from Hofmann et al. (2016) applied to the spins evolved using the waveform model's dynamics as described in Ossokine et al. (2020). For the NRSur PHM posterior, we applied the related surrogate remnant fit of Varma et al. (2019) for $M_{\rm f}$, $\chi_{\rm f}$, and $v_{\rm f}$. Applying the $M_{\rm f}$ and $\chi_{\rm f}$ surrogate fits to the posteriors from the Phenom PHM and SEOBNR PHM waveform models, and using the average of the fits from Healy & Lousto (2017), Hofmann et al. (2016), and Jiménez-Forteza et al. (2017) after applying corrections for precession (Johnson-McDaniel et al. 2016; Abbott et al. 2017b), both yield consistent results. The surrogate $v_{\rm f}$ was only tested for NRSur PHM (Varma et al. 2020); therefore, we do not apply it to Phenom PHM and SEOBNR PHM. The peak luminosity is also inferred using fits calibrated to NR (Healy & Lousto 2017; Keitel et al. 2017), while

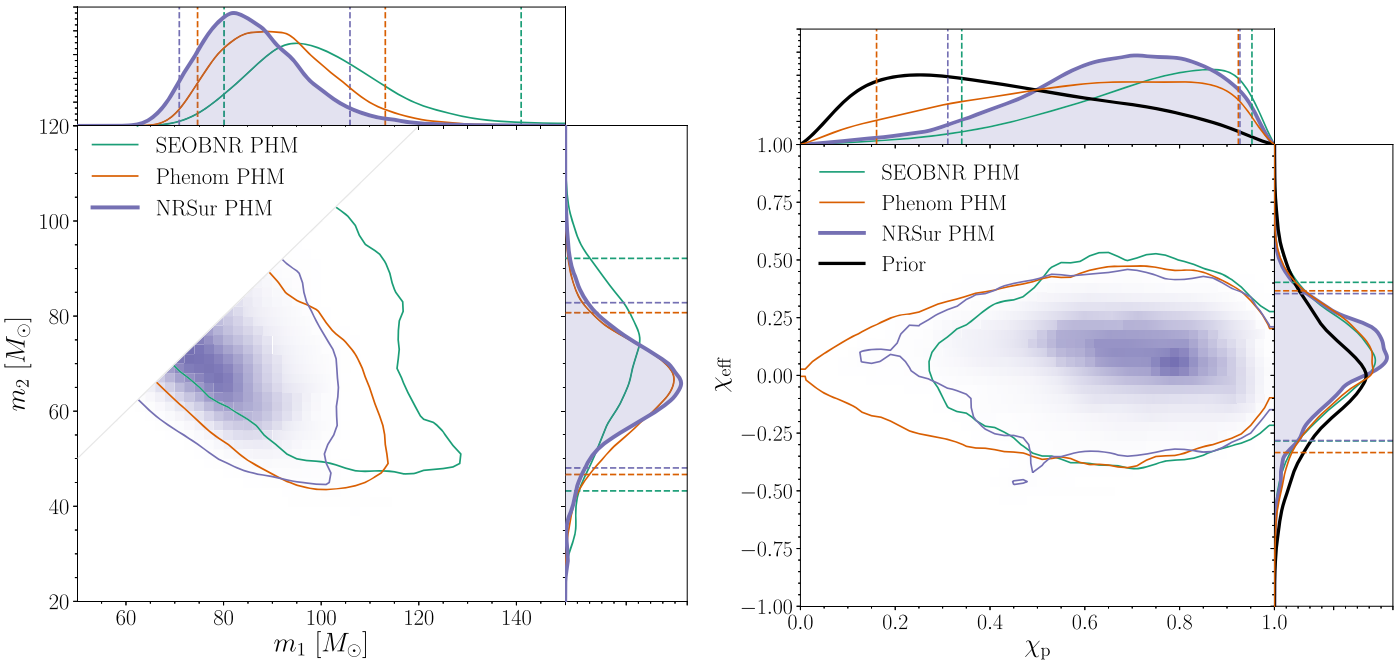

Figure 1. Posterior distributions on the individual source-frame masses (left) and effective spin parameters (right) according to the three waveform models employed. The one-dimensional distributions include the posteriors for the three waveform models, and the dashed lines mark their 90% credible interval. The two-dimensional plot shows the 90% credible regions for each waveform model, with lighter-blue shading showing the posterior distribution for the NRSur PHM model. The black lines in the right panel show the prior distributions.

Table 1
Source Properties for GW190521: Median Values with 90% Credible Intervals That Include Statistical Errors

Waveform Model	NRSur PHM	Phenom PHM	SEOBNR PHM
Primary BH mass m_1 $(M_\odot)$	85^{+21}_{-14}	90^{+23}_{-16}	99^{+42}_{-19}
Secondary BH mass m_2 $(M_\odot)$	66^{+17}_{-18}	65^{+16}_{-18}	71^{+21}_{-28}
Total BBH mass M $(M_\odot)$	150^{+29}_{-17}	154^{+25}_{-16}	170^{+36}_{-23}
Binary chirp mass $\mathcal{M}$ $(M_\odot)$	64^{+13}_{-8}	65^{+11}_{-7}	71^{+15}_{-10}
Mass ratio $q = m_2/m_1$	$0.79^{+0.19}_{-0.29}$	$0.73^{+0.24}_{-0.29}$	$0.74^{+0.23}_{-0.42}$
Primary BH spin χ_1	$0.69^{+0.27}_{-0.62}$	$0.65^{+0.32}_{-0.57}$	$0.80^{+0.18}_{-0.58}$
Secondary BH spin χ_2	$0.73^{+0.24}_{-0.64}$	$0.53^{+0.42}_{-0.48}$	$0.54^{+0.41}_{-0.48}$
Primary BH spin tilt angle $\theta_{\rm LS_1}$ (deg)	81^{+64}_{-53}	80^{+64}_{-49}	81^{+49}_{-45}
Secondary BH spin tilt angle $\theta_{\rm LS_2}$ (deg)	85^{+57}_{-55}	87^{+63}_{-58}	93^{+61}_{-60}
Effective inspiral spin parameter $\chi_{\rm eff}$	$0.08^{+0.27}_{-0.36}$	$0.06^{+0.31}_{-0.39}$	$0.06^{+0.34}_{-0.35}$
Effective precession spin parameter $\chi_{\rm p}$	$0.68^{+0.25}_{-0.37}$	$0.60^{+0.33}_{-0.44}$	$0.74^{+0.21}_{-0.40}$
Remnant BH mass $M_{\rm f}$ $(M_\odot)$	142^{+28}_{-16}	147^{+23}_{-15}	162^{+35}_{-22}
Remnant BH spin $\chi_{\rm f}$	$0.72^{+0.09}_{-0.12}$	$0.72^{+0.11}_{-0.15}$	$0.74^{+0.12}_{-0.14}$
Radiated energy $E_{\rm rad}$ $(M_\odot c^2)$	$7.6^{+2.2}_{-1.9}$	$7.2^{+2.7}_{-2.2}$	$7.8^{+2.8}_{-2.3}$
Peak Luminosity $\ell_{\rm peak}$ (erg s^{-1})	$3.7^{+0.7}_{-0.9} \times 10^{56}$	$3.5^{+0.7}_{-1.1} \times 10^{56}$	$3.5^{+0.8}_{-1.4} \times 10^{56}$
Luminosity distance $D_{\rm L}$ (Gpc)	$5.3^{+2.4}_{-2.6}$	$4.6^{+1.6}_{-1.6}$	$4.0^{+2.0}_{-1.8}$
Source redshift z	$0.82^{+0.28}_{-0.34}$	$0.73^{+0.20}_{-0.22}$	$0.64^{+0.25}_{-0.26}$
Sky localization $\Delta\Omega$ (deg^2)	774	862	1069

the energy radiated in the merger is given by $M - M_{\rm f}$. The key analysis elements described above, including parameter estimation sampling algorithms, PSD estimates, and waveform models, all potentially introduce systematic uncertainties. Different choices for these elements can affect the results but in most cases these changes are significantly smaller than the statistical uncertainties. Below, we highlight the more significant differences in the results associated with waveform models.

2.2. Primary and Secondary BH Components

In Table 1 we summarize the source properties of GW190521. Results are quoted as the median and symmetric 90% credible interval of the marginalized posterior distributions for each parameter, and for each of the three GW signal models. The measurements are marginalized over uncertainty in the data calibration. In the rest of this paper we quote source properties derived using NRSur PHM, unless explicitly stated otherwise.

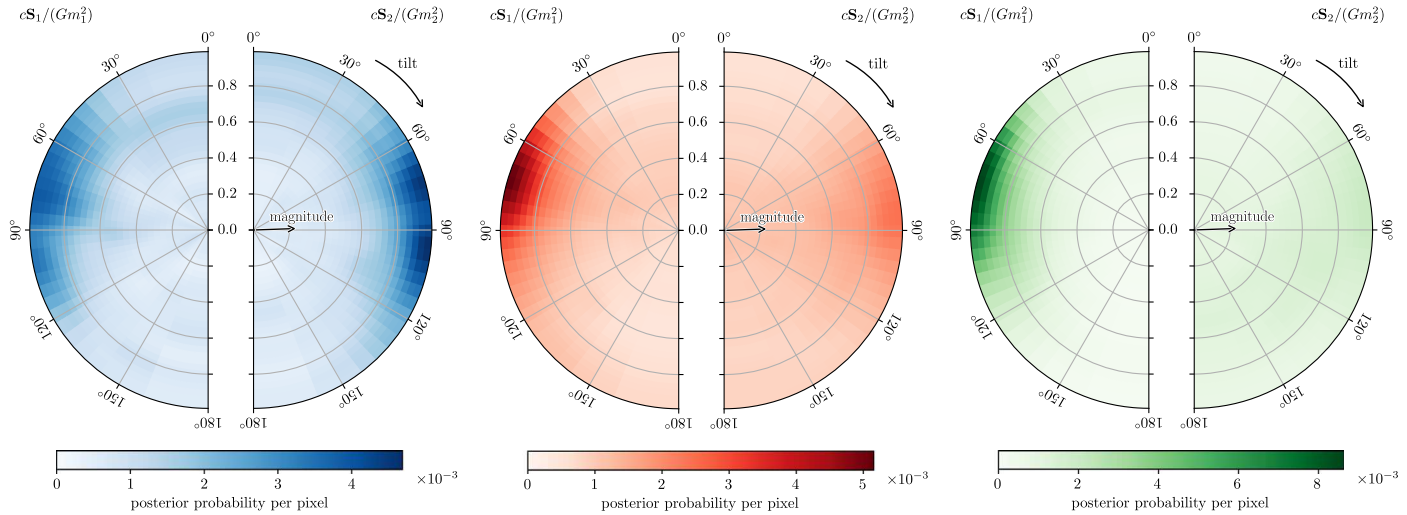

Figure 2. Posterior probabilities for the dimensionless component spins, $c\boldsymbol{S}_1/(Gm_1^2)$ and $c\boldsymbol{S}_2/(Gm_2^2)$, relative to the orbital angular momentum axis $\hat{\boldsymbol{L}}$. Shown here for the three waveform models (left to right: NRSur PHM, Phenom PHM, and SEOBNR PHM). The tilt angles are 0° for spins aligned with the orbital angular momentum and 180° for spins anti-aligned. Probabilities are marginalized over the azimuthal angles. The pixels have equal prior probability, being equally spaced in the spin magnitudes and the cosines of tilt angles. The spin orientations are defined at a fiducial GW frequency of 11 Hz.

Masses.—The estimated mass posterior distributions are shown in the left panel of Figure 1 for the three GW signal models. The primary BH mass of GW190521 is $m_1 = 85^{+21}_{-14}\,M_\odot$, making it the highest-mass component BH known to date in GW astronomy. The mass of the secondary BH is inferred to be $m_2 = 66^{+17}_{-18}\,M_\odot$. The primary BH of GW190521 is more massive (median value) than any *remnant* BH reported in GWTC-1 except for GW170729 (Abbott et al. 2019i); the secondary BH of GW190521 is also more massive than any *primary* BH in GWTC-1.

These source-frame masses have been redshift corrected, as discussed above, using a value of the Hubble parameter $H_0 = 67.9$ from Planck 2015. However, recent measurements of H_0 using nearby Cepheid distance standards obtain a precise value of $H_0 = 74.03 \pm 1.42\,\mathrm{km\,s^{-1}\,Mpc^{-1}}$ (Riess et al. 2019), 9% higher than the Planck value. Using the latter value along with the other cosmological parameters from Planck 2015 increases the median value of the redshift by 7% and reduces the estimated source-frame masses by 3%. These shifts are significantly smaller than statistical or other systematic uncertainties, including those affecting the astrophysical interpretation discussed throughout this paper.

While the low-mass cutoff of the PI mass gap is uncertain (see Section 5.1), the primary BH of GW190521 offers strong evidence for the existence of BHs in the mass gap. If the PI gap begins at $50\,M_\odot$ ($65\,M_\odot$), we find that the primary BH has only a $< 0.1\%$ (0.3%) probability of being below the mass gap, while the secondary BH has 6.6% (46.2%) probability of also being below the mass gap.

The SEOBNR PHM model supports a higher primary mass and more asymmetric mass ratio for GW190521: within 90% credible intervals, m_1 and m_2 can be as high as $141\,M_\odot$ and $92\,M_\odot$ respectively, while support for the mass ratio extends down to $q \sim 0.32$. While the upper limit of the PI mass gap remains uncertain, adopting $120\,M_\odot$ as the high-mass end of the gap, we find the probability that the primary BH of GW190521 is beyond the gap of 12% when using the SEOBNR PHM model. The corresponding probabilities using the NRSur PHM and Phenom PHM models are 0.9% and 2.3%, respectively.

The probability that at least one of the BHs in GW190521 is in the range 65–$120\,M_\odot$ is 99.0%, using the NRSur PHM model. The corresponding probabilities using the SEOBNR PHM and Phenom PHM models are 90.2% and 98.0%, respectively.

We measure the total binary mass of GW190521 to be $M = 150^{+29}_{-17}\,M_\odot$ making it the highest-mass binary observed via GWs to date. The binary chirp mass is $\mathcal{M} = 63^{+13}_{-8}\,M_\odot$, a factor of $\sim$2 higher than the first BBH detection, GW150914 (Abbott et al. 2016a, 2019i). GW190521 is consistent with a nearly equal mass binary with mass ratio $q = m_2/m_1 = 0.79^{+0.19}_{-0.29}$ (90% credible interval).

In the detector frame, the measured masses are $m_1^{\mathrm{det}} = 152^{+32}_{-19}\,M_\odot$, $m_2^{\mathrm{det}} = 120^{+21}_{-32}\,M_\odot$, $M^{\mathrm{det}} = 272^{+29}_{-27}\,M_\odot$, and $\mathcal{M}^{\mathrm{det}} = 117^{+12}_{-14}\,M_\odot$, using the NRSur PHM model. These results are very nearly the same for all three models.

Spins.—Due to its high total mass, GW190521 is the shortest-duration signal (approximately 0.1 s) recorded so far in the LIGO and Virgo detectors. With only around four cycles (two orbits) in the frequency band 30–80 Hz (Abbott et al. 2020b), information about spin evolution during the coalescence is limited. Still, analyses of GW190521 indicate that GW signal models including effects of spin–orbit precession are mildly preferred over those that omit such effects (i.e., allow only spins aligned with the orbital axis), with a $\log_{10}$-Bayes factor of $+0.65 +- 0.06$ for the NRSur PHM model allowing generic BH spins versus limiting the effects of spin to the aligned components.

In the disk plots of Figure 2, we show constraints on the spins of the component BHs of GW190521 in terms of their dimensionless magnitudes χ_1 and χ_2 and polar angles (tilts) with respect to the orbital angular momentum, θ_{LS_1} and θ_{LS_2}, defined at a fiducial GW frequency of 11 Hz. Median values from all three waveform models suggest in-plane spin components with high spin magnitudes for both the BHs. Within the 90% credible intervals given in Table 1, however, the constraints on the dimensionless BH spin magnitudes remain uninformative. For our preferred model NRSur PHM, the 90% bounds on spin magnitude extend from $\chi_{1,2} \sim 0.1$ to 0.9. The constraints on the tilt angles of these spins are also relatively broad.

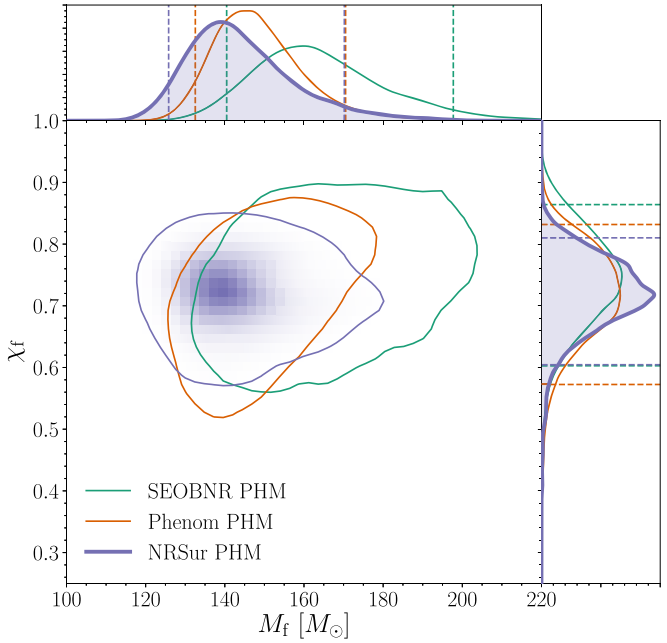

Figure 3. Posterior distributions of the mass (M_f) and the dimensionless spin (χ_f) of the remnant BH according to the three waveform models employed. The one-dimensional distributions include the posteriors for the three waveform model, and the dashed lines mark their 90% credible interval. The two-dimensional plot shows the 90% credible regions for each waveform model, with lighter-blue shading showing the posterior distribution for the NRSur PHM model.

As for past GW observations, we present inferences on the spins of GW190521 using the parameters $\chi_{\rm eff}$ and $\chi_{\rm p}$ constructed from the mass and spin of the binary components. Here, $\chi_{\rm eff} = (m_1\chi_1\cos\theta_1 + m_2\chi_2\cos\theta_2)/(m_1+m_2) \in [-1, 1]$ is the effective inspiral spin parameter (Damour 2001; Ajith et al. 2011), which measures the mass-weighted net spin aligned with the orbital angular momentum axis $\hat{\boldsymbol{L}}$ and remains approximately constant throughout the inspiral (Racine 2008). The effective precession spin parameter $\chi_{\rm p} \in [0, 1]$ (Schmidt et al. 2015) measures the spin components in the plane of the orbit and therefore the strength of the spin–orbit precession in the binary. The inferred posterior distributions of $\chi_{\rm eff}$ and $\chi_{\rm p}$ are shown in the right panel of Figure 1 for the three GW signal models. Our priors are uniform in the component spins of the binaries, which results in nontrivial priors for the effective spin parameters, shown as the black distribution in the figure. For all three waveform models the posterior distribution of $\chi_{\rm eff}$ is peaked close to 0, similarly to the prior, while the $\chi_{\rm p}$ distribution is shifted toward higher values. While the bulk of the posterior on $\chi_{\rm p}$ suggests an in-plane component of the spins, which contributes to spin-induced precession, the broad distribution prevents a more conclusive finding.

2.3. Remnant BH

Mass and Spin.—The merger of GW190521 resulted in a final (remnant) BH of mass $M_{\rm f} = 142^{+28}_{-16}\,M_\odot$ (see Figure 3). The inferred mass of the remnant BH provides observational evidence for an IMBH of $\gtrsim 100\,M_\odot$. The remnant BH mass is $7.6^{+2.2}_{-1.9}\,M_\odot$ less than the sum of the component BH masses; the equivalent energy was released as GWs during coalescence, making GW190521 the most energetic GW event recorded to date. We find a peak luminosity close to merger $\ell_{\rm peak} = 3.7^{+0.7}_{-0.9} \times 10^{56}$ erg s^{-1}.

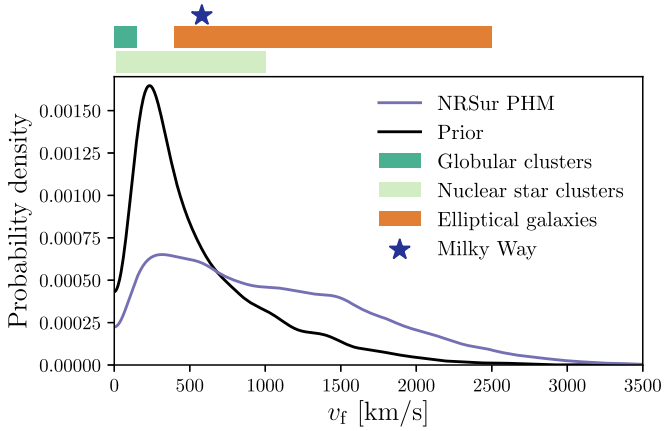

Figure 4. Posterior and prior distributions for the kick magnitude of GW190521. For comparison, we show known ranges for the escape velocities from globular clusters, nuclear star clusters, giant elliptical galaxies, and the Sun's location in the Milky Way.

The remnant BH of GW190521 has a dimensionless spin parameter $\chi_{\rm f} = 0.72^{+0.09}_{-0.12}$. Within the 90% credible interval this is consistent with the BBH merger remnant spins reported in GWTC-1 (Abbott et al. 2019i). The predictions for remnant BH parameters from the inferred values of the component masses and spins agree with analyses of GW190521 that target the ringdown portion of the signal, directly measuring $M_{\rm f}$ and $\chi_{\rm f}$ without assuming a quasi-circular BBH, described in Section 3.2.

Recoil Velocity.—In generic BBH mergers, the radiation of linear momentum through beamed GW emission imparts a recoil velocity, or kick, to the remnant BH (Fitchett 1983; Favata et al. 2004), of magnitude up to $\sim$5000 km s^{-1} for precessing systems (Favata et al. 2004; Lousto & Zlochower 2011). As large in-plane spin components are not ruled out for GW190521, it is a potential candidate for a large kick. Figure 4 shows the prior and posterior distributions for the kick magnitude, with respect to the center of mass of the progenitor binary, computed using NRSur PHM and applying the related remnant surrogate model (Varma et al. 2019) to the component masses and spins. Although the kick velocity remains unconstrained, we find that the posterior is weighted toward higher values relative to the prior, with support for values exceeding fiducial escape velocities for globular clusters, the half-mass radius of nuclear star clusters (Antonini & Rasio 2016), giant elliptical galaxies (Fitchett 1983; Merritt et al. 2004; Campanelli et al. 2007a), and Milky Way–like galaxies (Monari et al. 2018).

2.4. Extrinsic Parameters

Sky Position.—The initial sky map of GW190521, computed using the low-latency pipeline `BAYESTAR` (Singer & Price 2016), was publicly released with the initial public circular on 2019 May 21 03:08:32 UTC (Abbott et al. 2019b). The source was localized within a 90% credible area of 1163 deg^2 (see blue curve in Figure 5). An updated sky map was released the same day at 13:32:27 UTC (Abbott et al. 2019f), using a low-latency analysis from `LALInference` employing the `SEOBNRv4_ROM model` (Bohé et al. 2017), giving a 90% credible localization within 765 deg^2 (orange curve in Figure 5). Here we report our latest constraints on the

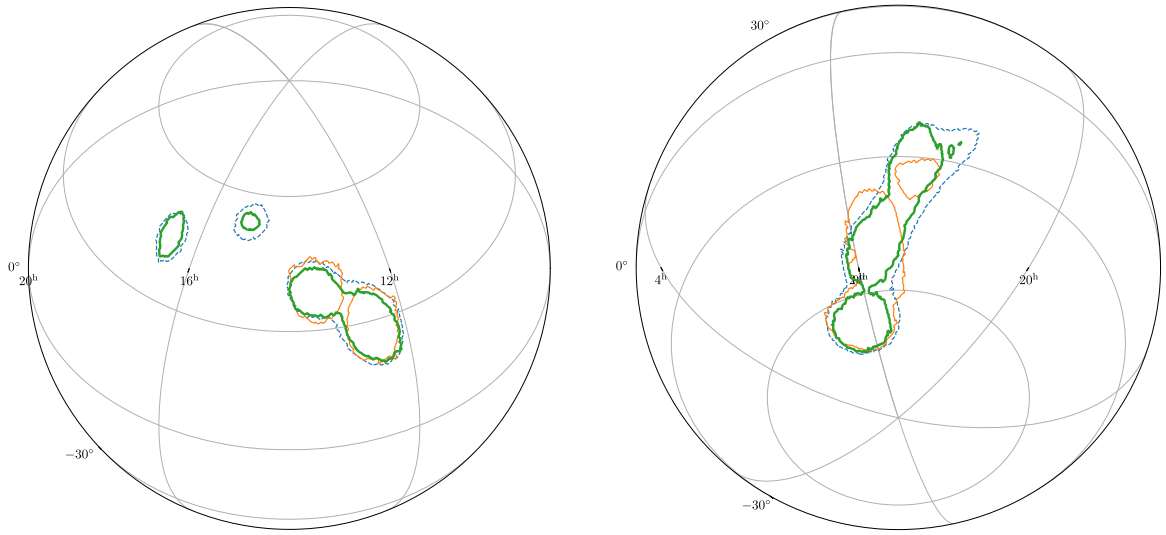

Figure 5. Sky maps (source location 90% credible areas) for GW190521, as seen from the north (left) and south (right) celestial poles. The blue (dashed) and orange (solid thin) curves show two low-latency sky maps from the BAYESTAR pipeline and the LALInference pipeline using the SEOBNRv4_ROM waveform model; neither incorporates higher-order multipoles. The green (solid thick) curve, reported here for the first time, was obtained from full parameter estimation with the NRSur HM model.

sky position of GW190521 found using LALInference with the NRSur PHM model (green curve in Figure 5). The source is now localized within 774 deg^2.

Distance and Inclination.—The inferred luminosity distance D_L reported at low latency (Abbott et al. 2019b, 2019f) made use of waveform models that did not include higher-order multipoles. As discussed in Section 2.5, the luminosity distance and redshift inferred using the waveform models described in this paper that incorporate higher-order multipoles result in larger values than those low-latency estimates. In Figure 6, we show the posteriors on the luminosity distance D_L and the inclination angle θ_{JN} of GW190521 for the three waveform models. Here, the inclination angle is between the *total* angular momentum of the source and the observer's line of sight. One can note in the figure the typical correlation between D_L and θ_{JN} and near degeneracy between systems with the angular momentum vector pointed toward or away from the observer. GW emission is strongest along the orbital angular momentum direction, so face-on sources at larger distances produce similar signals to edge-on sources closer by. Both the NRSur PHM and Phenom PHM models suggest that the total angular momentum of the source is roughly aligned with the observer's line of sight $\theta_{\mathrm{JN}} \sim 0°$ or 180°, i.e., the orbital plane is close to face-on to the line of sight, while the SEOBNR PHM model also supports an orbital plane that is closer to edge-on ($\theta_{\mathrm{JN}} \sim 90°$). In accordance with the covariance between the distance and inclination, the NRSur PHM model places GW190521 at $D_L = 5.3^{+2.4}_{-2.6}$ Gpc ($z \simeq 0.82^{+0.27}_{-0.29}$), while the SEOBNR PHM model suggests $D_L = 4.0^{+2.0}_{-1.8}$ Gpc. The masses of the component BH and remnant BH scale inversely with $(1+z)$. In accordance, as reported in Table 1, the SEOBNR PHM model supports higher masses than the other two models. A binary close to face-on, as favored by our preferred NRSur PHM model, makes it difficult to directly observe the effects of spin–orbit precession; thus, the evidence for precession in GW190521, reported in the *Spins* subsection of Section 2.2 above, is weak.

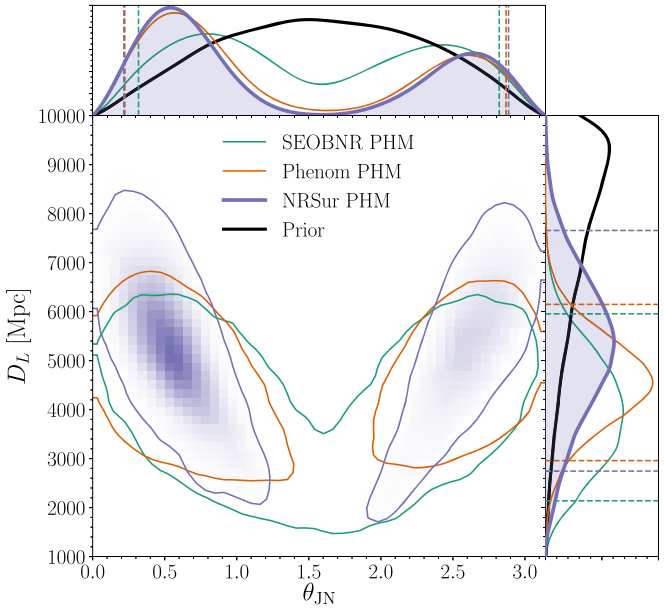

Figure 6. Posterior distributions of the inclination (θ_{JN}) and the luminosity distance (D_L) according to the three waveform models employed. The one-dimensional distributions include the posteriors for the three waveform models, and the dashed lines mark their 90% credible interval; black lines show the prior distributions. The two-dimensional plot shows the 90% credible regions for each waveform model, with lighter-blue shading showing the posterior distribution for the NRSur PHM model.

2.5. Impact of Higher-order Multipoles

The GWs emitted during a BBH coalescence can be decomposed as spherical harmonic multipoles ℓ and $|m| \leqslant \ell$. The quadrupole $(\ell, |m|) = (2, 2)$ mode remains dominant during most of the inspiral, while other, higher-order multipoles become comparable near the merger and ringdown stages (see, e.g., Pan et al. 2011; Calderón Bustillo et al. 2016). Higher-order multipoles have been found to be important for high-mass BBH mergers in advanced detector observations

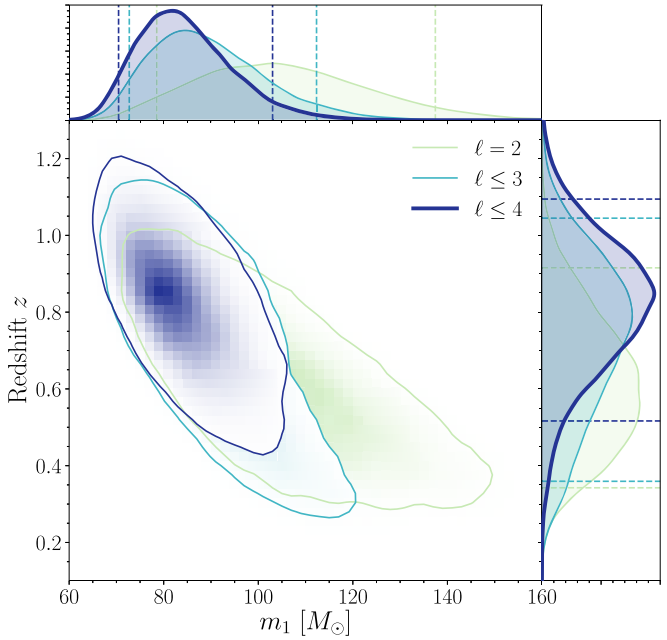

Figure 7. Posterior probability density for the source-frame mass of the primary BH m_1 and luminosity distance D_L. The one-dimensional distributions include the posteriors for the NRSur PHM waveform using the RIFT pipeline, for different combinations of multipoles: dominant multipole $\ell = 2$ (light green), higher-order multipoles up to $\ell \leqslant 3$ (light blue), and those up to $\ell \leqslant 4$ (dark blue). The two-dimensional plot shows the contours of the 90% credible areas, with light-blue shading showing the posterior density function for $\ell \leqslant 4$.

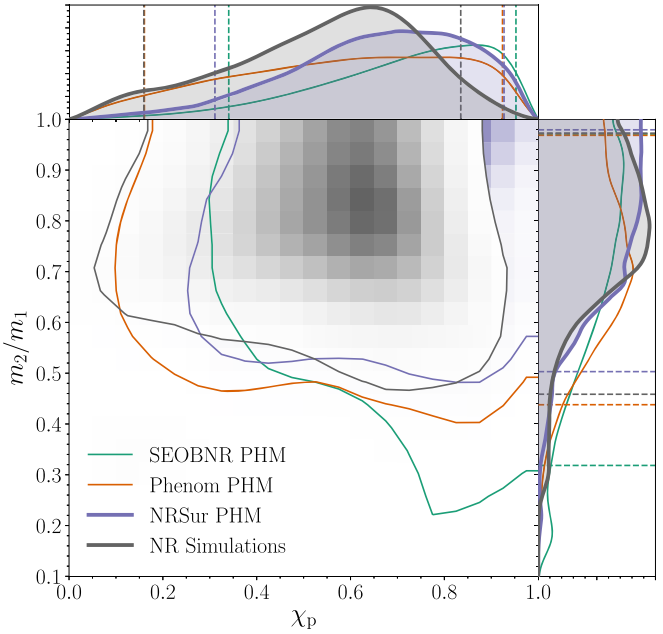

Figure 8. Posterior probability density for the precessing spin parameter χ_p and mass ratio from the direct comparison of NR simulations with GW190521 (gray tiles, and gray contour showing 90% confidence area). For comparison, shown here are the 90% bounds on these parameters from the three waveform models.

(Pan et al. 2011; Varma et al. 2014; Graff et al. 2015; Varma & Ajith 2017; Calderón Bustillo et al. 2017, 2018; Mehta et al. 2017; Chatziioannou et al. 2019; Kumar Mehta et al. 2019); their presence was also crucial in reducing uncertainties in the mass ratio and component spins of the recently reported unequal-mass binary mergers GW190412 (Abbott et al. 2020a) and GW190814 (Abbott et al. 2020e). To quantify the impact and evidence of higher-order multipoles on GW190521, we computed the posterior distribution of our preferred model, NRSur PHM (Varma et al. 2019), using the RIFT pipeline (Lange et al. 2018) for three different combinations of modes: $\ell = 2$, $\ell \leqslant 3$, and $\ell \leqslant 4$.

GR predicts radiation from BBH mergers at all multipoles, with amplitudes strongly dependent on the binary mass ratio and orbital inclination angle (Graff et al. 2015; London et al. 2018); evidence of their presence consistent with GR is presented in Abbott et al. (2020a).

We find that the omission of higher-order multipoles leads to broader posterior distributions for some parameters of GW190521, especially the binary orbital inclination angle θ_{JN}. The higher-order multipoles enable better constraints of the binary inclination angle, which is coupled to the source-frame mass estimates through the luminosity distance D_L, and therefore the redshift. Inclusion of these higher-order multipoles results in significantly larger values for these parameters. As shown in Figure 7, this change in distance directly impacts our inference of the primary BH mass of GW190521. For our preferred model, if we only included $\ell = 2$, the posterior distribution of primary BH mass extends to $m_1 = 137\,M_\odot$ at the 90% credible interval. As we include higher-order multipoles up to $\ell = 4$, the masses are better constrained and we find that m_1 cannot be greater than $103\,M_\odot$ at the 90% credible interval. We find that the higher-order multipoles have marginal impact on constraining the effective precession spin parameter χ_p.

Although the released version of NRSur PHM (Varma et al. 2019) does not include multipoles with $\ell > 4$, we have extended it to include all multipoles with $\ell = 5$ and find that the parameter estimation results are nearly identical to those for $\ell \leqslant 4$; the $\ell = 5$ multipoles are found to be quantitatively negligible for GW190521.

While higher-order multipoles influence our inference of the source properties, the observation of GW190521 does not offer evidence for such multipoles. The $\log_{10}$-Bayes factor for our preferred model with and without higher-order multipoles is -0.38, implying that the data marginally disfavor their presence, but there is no statistically significant evidence for their absence. As noted above, this gives important information about the orbital inclination of the binary, as higher-order multipoles are suppressed for face-on binary orbits. Since higher-order multipoles are a firm prediction of GR and significantly affect parameter estimation, they must be included when modeling GW190521.

2.6. Comparison with NR

We compared the data from LIGO and Virgo at the time of GW190521 directly with 3459 NR simulations of BBH coalescence (Jani et al. 2016; Boyle et al. 2019; Healy et al. 2019). These NR simulations are the most accurate representation available of the strong-field dynamics near merger and the radiated higher-order multipoles. As was done for previous direct comparisons of NR simulations with LIGO–Virgo-detected events (Abbott et al. 2016a, 2019i; Healy et al. 2018), the likelihood of the data was calculated for each waveform derived from NR simulations. Using the RIFT pipeline (Lange et al. 2018) to evaluate these comparisons and interpolate them over all intrinsic parameters, we deduce a posterior distribution for all detector-frame quantities: redshifted mass, mass ratio, and both component spins.

As shown in Figure 8, we find that the best-matching (highest-likelihood) NR waveforms and the derived posterior

distribution are consistent with the mass ratio of GW190521 being near unity. We also find that the analysis favors NR waveforms with $\chi_{\rm eff} \sim 0$ and $\chi_{\rm p} \sim 0.6$, further suggesting that GW190521 is a precessing binary. The agreement between our preferred model NRSur PHM and the NR simulations provides an independent check on the inferred source properties of GW190521.

3. Consistency with Binary Merger Waveform Models

GW190521 presents an opportunity for strong-field tests of GR in a previously unexplored region of parameter space (Abbott et al. 2016c, 2019g). We first test the consistency of the data with the waveform models employed for parameter estimation by searching for unmodeled residual power; we then study in detail the properties of the ringdown phase using fewer assumptions on the progenitors of the remnant BH, and we demonstrate consistency with predictions from the full waveform models.

3.1. Residual Tests

We first test the consistency of the templates used for parameter estimation with the observed signal by subtracting the maximum likelihood NRSur PHM waveform from the data and studying the residual (Abbott et al. 2016c, 2020f). The residual data are analyzed by the `BayesWave` algorithm, which simultaneously fits models for the noise PSD and short (<1 s) transient signals coherent across the detector network (Cornish & Littenberg 2015). `BayesWave` does not assume a particular waveform morphology, instead using a linear combination of wavelets to fit excess coherent features in the data of arbitrary shape.

The metric used for quantifying the coherent residual, $\mathrm{S/N}_{90}$, is the upper 90% credible bound on the posterior distribution function of the recovered S/N of the wavelet reconstruction (Abbott et al. 2016c). The significance of the recovered $\mathrm{S/N}_{90}$ value is empirically measured by repeating the analysis on 195 randomly chosen off-source times drawn from 4096 s of detector data surrounding the event time, which serves as the background estimate for $\mathrm{S/N}_{90}$. For GW190521, we find $\mathrm{S/N}_{90} \sim 6.34$, which is consistent with expectations for typical LIGO–Virgo noise, resulting in a p-value of ∼0.26 when compared to the times analyzed immediately surrounding the merger time. Since the residual is consistent with noise, we find that the best-fit waveform interpolated from numerical solutions of GR, as used in our parameter estimation analyses, is consistent with the observed signal within the measurement capability of the detectors.

3.2. Tests Using Final BH Ringdown

In this section, we describe a number of studies that explore the nature of the remnant compact object and also evaluate the consistency of the observed signal with waveform models for a quasi-circular BBH merger in GR. These are extensions to similar tests applied to previous LIGO–Virgo BBH events (Abbott et al. 2016c, 2019g). As in the case for those previous tests, the high mass of GW190521 makes it possible to study the quasi-normal oscillations of the remnant BH approaching a stationary state (ringdown), as encoded in the last few cycles of the GW signal (see Vishveshwara 1970; Buonanno et al. 2007; Berti et al. 2009, 2018, and references therein). Parameter estimates obtained from the ringdown studies presented in this section are solely extracted from the properties of the remnant. For these studies, we consider both a model that makes no assumptions on the process leading to the signal formation and waveform templates specifically modeling the remnant of a quasi-circular BBH merger. The results are thus robust against systematic uncertainty due to the possible neglect of eccentricity or other physical effects in modeling the system; for further discussion of such effects see Section 6.1.

We model the ringdown as a set of damped sinusoids and measure the properties of the signal using `pyRing`, a time domain analysis framework (Carullo et al. 2019; Isi et al. 2019). Within the analysis, the beginning of the ringdown-dominated portion of the signal is marked by a fixed time t_0 (see Supplement of Isi et al. 2019), reported with respect to an estimate of the peak time of the complex strain at each detector. The peak time is taken from the posterior median inferred from the NRSur PHM model and yields a GPS time for LIGO Hanford $t^{\rm H}_{\rm peak} = 1242442967.4306^{+0.0067}_{-0.0106}$ s; times in other detectors are computed by assuming a fixed sky position. The duration of the analysis segment after the start time in each detector is 0.1 s. We consider three distinct models of the ringdown: for each, we use the `CPNest` Bayesian nested sampling algorithm (Del Pozzo & Veitch 2020) to compute posterior distributions on the model parameters.

The first model consists of a single damped sinusoid of arbitrary complex frequency, amplitude, and phase, with no assumptions on the nature of the remnant object. The left panel of Figure 9 shows the resulting 90% credible regions for the posterior probability distribution of the redshifted, detector-frame frequency and damping time, assuming uniform priors on these two parameters (solid curves). Since there is uncertainty in the time at which the single damped sinusoid model may become valid, we perform this analysis by truncating the data at different start times, as in Kamaretsos et al. (2012) and Abbott et al. (2016c): we choose start times $\Delta t_0 \equiv t_0 - t^{\rm H}_{\rm peak} \simeq 6.4$, 12.7, and 19.1 ms after the reference time. In units of the redshifted remnant mass $M^{\rm det}_{\rm f} = (1+z)M_{\rm f} = 258.3\,M_\odot$ (median estimate from NRSur PHM) these times correspond to $\Delta t_0 = 5$, 10, 15 $GM^{\rm det}_{\rm f}/c^3$. Truncating the data at later times yields uninformative posteriors due to the decrease in S/N. Values of $\Delta t_0 \geqslant 10\,GM^{\rm det}_{\rm f}/c^3$ are consistent with the range where numerical simulations predict that the fundamental mode should be dominant for this source. The systematic uncertainty due to the choice of the NRSur PHM model in determining $t_{\rm peak}$ as opposed to other waveform models considered in this paper is negligible with respect to the statistical uncertainty.

At a start time of $\Delta t_0 = 12.7$ ms (corresponding to $10\,GM^{\rm det}_{\rm f}/c^3$), we measure a ringdown frequency $f = 66.0^{+4.0}_{-3.0}$ Hz and damping time $\tau = 19.0^{+9.0}_{-7.0}$ ms. As the start time increases from 6.4 to 19.1 ms, we observe convergence toward the predicted value of the least damped mode frequency, together with a broadening of the posterior due to the decreasing S/N of the ringdown. Similar behavior is observed for the other models we will present in the remainder of the section.

The second model is built from the superposition of a set of damped sinusoids with arbitrary amplitudes and phases, but with complex frequencies determined by the remnant mass $M_{\rm f}$ and dimensionless spin $\chi_{\rm f}$, as predicted by perturbation theory (Berti et al. 2006). We include up to the $n = 0$, 1, 2 overtones of the $\ell = m = 2$ ringdown mode of a Kerr BH starting at the peak of the complex strain (Buonanno et al. 2007;

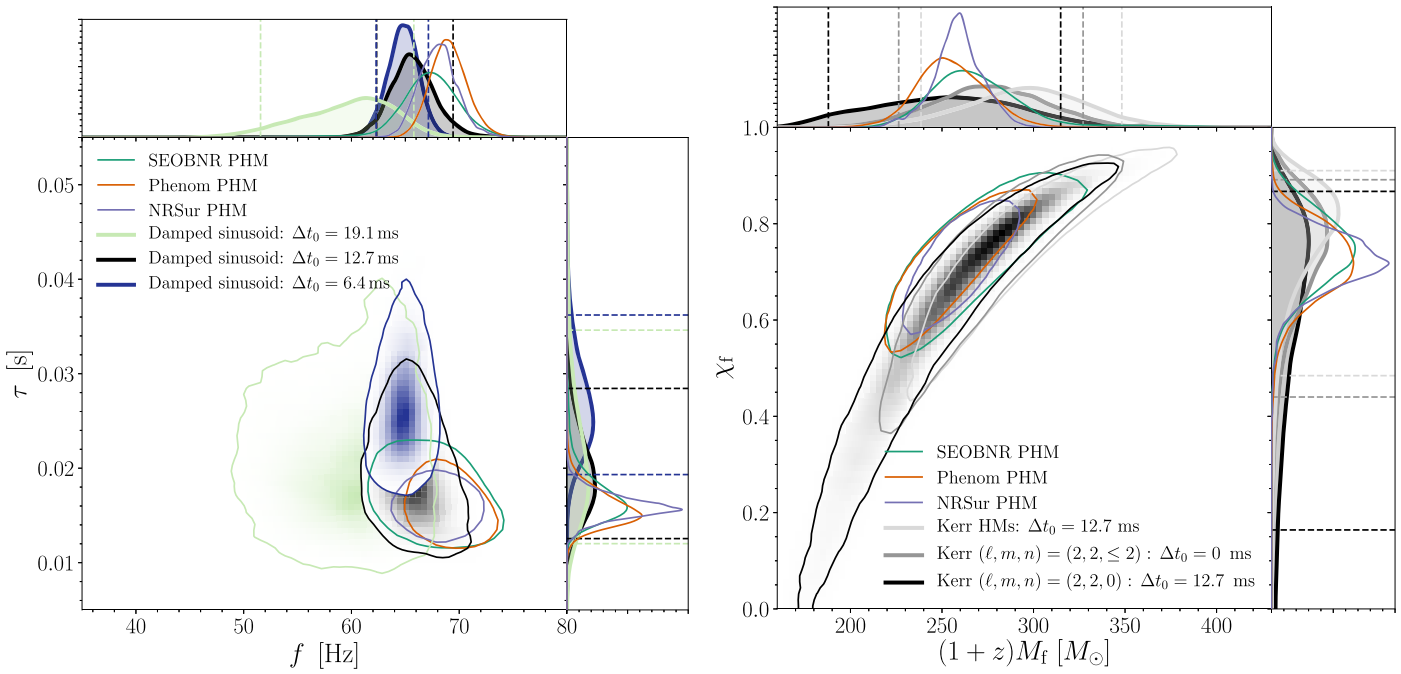

Figure 9. Left: redshifted (detector-frame) frequency and damping time inferred from the ringdown portion of the GW190521 signal. Measurements using a single damped sinusoidal model of the ringdown are shown with filled contours at different start times $\Delta t_0 = 6.4$ ms (blue), 12.7 ms (black), and 19.1 ms (light-green) ($\sim$5, 10, 15 $GM_f^{\rm det}/c^3$) after the reference $t_{\rm peak}^{\rm H}$. These are compared with the least-damped ringdown mode from the three distinct inspiral-merger-ringdown waveform models described in Section 2.1. Right: redshifted remnant mass $M_f^{\rm det} = (1+z)M_f$ and spin inferred from the ringdown portion of the signal. The filled contours show the measurement using the fundamental Kerr $\ell = 2$, $m = 2$, $n = 0$ multipole (black); the $\ell = 2$, $m = 2$ Kerr model including overtones up to $n = 2$ (gray); and the fundamental higher mode model (Kerr HMs, light gray) described in the text. These are compared with redshifted remnant mass and spin obtained using the three waveform models stated in Section 2.1 and Figure 3. Contours enclose 90% of the posterior distribution, and the 1D histogram shows the 90% credible regions only for the ringdown models.

Giesler et al. 2019; Ota & Chirenti 2020); see also Bhagwat et al. (2020) and Okounkova (2020) for discussions concerning the interpretation of a linearized approximation starting at the peak of GW emission. The redshifted, detector-frame remnant mass and spin obtained from this waveform model are shown in the right panel of Figure 9, assuming a uniform prior over these two parameters. We find $M_f^{\rm det} = 252.0^{+63.0}_{-64.0}\,M_\odot$, $\chi_f = 0.65^{+0.22}_{-0.48}$ taking $\Delta t_0 = 12.7$ ms and including only the fundamental Kerr ($\ell = 2$, $m = 2$, $n = 0$) mode, and $M_f^{\rm det} = 276.0^{+51.0}_{-50.0}\,M_\odot$, $\chi_f = 0.74^{+0.15}_{-0.3}$ taking $\Delta t_0 = 0$ ms and including overtones up to $n = 2$.

Finally, the third model (Kerr HMs) consists of a set of damped sinusoids corresponding to all fundamental modes (i.e., without inclusion of overtones) of a Kerr BH up to $\ell = 4$ and $m = \ell$, $\ell - 1$, including spherical−spheroidal harmonic mixing (London 2018). Complex frequencies are predicted as a function of the remnant mass M_f and dimensionless spin χ_f, while amplitudes and phases are calibrated on NR simulations of nonprecessing BBH mergers. With this model we measure $M_f^{\rm det} = 296.0^{+52.0}_{-58.0}\,M_\odot$, $\chi_f = 0.79^{+0.12}_{-0.3}$ taking $\Delta t_0 = 12.7$ ms; the full probability distribution is shown in the right panel of Figure 9.

In Figure 9, we compare the ringdown measurements to the posterior credible regions for the remnant parameters obtained through NR-calibrated fits from the initial binary parameters, as described in Section 2.1, from the three different full waveform models discussed above. The posterior of the ringdown analyses is consistent at the 90% credible level with the full-signal analyses. Furthermore, despite the different physical content, both models that include higher multipoles or overtones obtain measurements of remnant parameters consistent with the single-mode analysis estimates; a Bayes factor computation also does not find strong evidence in favor of the presence of higher multipoles or overtones.

A parameterized test of gravitational waveform generation (Blanchet & Sathyaprakash 1995; Mishra et al. 2010; Li et al. 2012a, 2012b; Agathos et al. 2014) based on the Phenom PHM waveform model also does not reveal inconsistencies with GR predictions. Full details will be provided in an upcoming paper.

4. Single-event-based Merger Rate Estimate

We estimate the rate of mergers similar to this source, assuming a constant rate per comoving volume–time element. We proceed similarly to Abbott et al. (2016b): in the absence of a parameterized population model for such sources, we assume a population of mergers whose intrinsic parameters (component masses and spins) are identical to the detected event up to measurement errors (Kim et al. 2003). We estimate the sensitivity of the LIGO–Virgo detector network by adding simulated signals to data from the O1, O2, and O3a observing runs and recovering them with the `Coherent WaveBurst` (cWB) weakly modeled transient detection pipeline (Klimenko et al. 2016), optimized for sensitivity to IMBH mergers (Abadie et al. 2012), which identified GW190521 with the highest significance (Abbott et al. 2020b). As in Abbott et al. (2017d, 2016b), we consider a simulated signal to be detected if recovered with an estimated false-alarm rate of 1 per 100 yr or less. Simulated signals are prepared by drawing source parameter samples from a posterior distribution inferred using the NRSur PHM waveform (Section 2). The simulations' component masses and spins are taken directly from the posterior samples, whereas their line-of-sight direction and orbital axis direction are randomized, and their luminosity

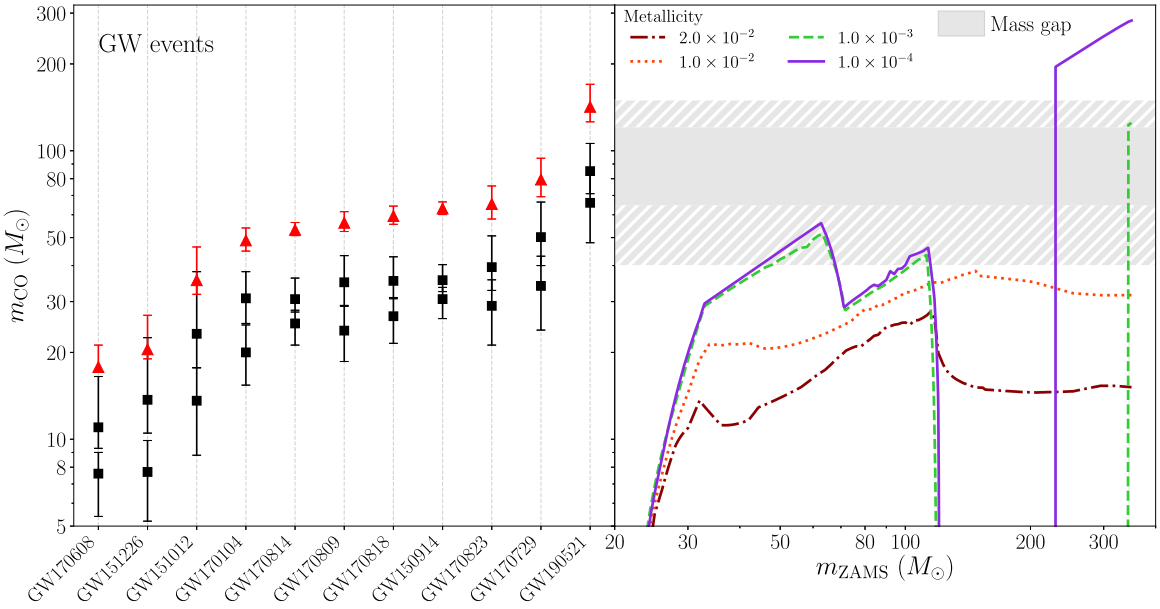

Figure 10. Left: masses ($m_{\rm CO}$) of GW190521 compared with BBH detections in O1 and O2. Black squares and error bars represent the component masses of the merging BHs and their 90% uncertainties, and red triangles represent the mass and associated uncertainties of the final merger remnants. Right: predicted compact-object mass, as a function of the zero-age main-sequence mass of the progenitor star ($m_{\rm ZAMS}$ up to 350 $M_\odot$) and for four different metallicities of the progenitor star (ranging from $Z = 10^{-4}$ to $Z = 2 \times 10^{-2}$; Spera & Mapelli 2017). This model accounts for single stellar evolution from the PARSEC stellar evolution code (Bressan et al. 2012), for CCSNe (Fryer et al. 2012), and for PPI and PI supernovae (Woosley 2017). Only the two metal-poor models with metallicity $Z = 10^{-3}$ (dashed green line) and $Z = 10^{-4}$ (purple solid line) undergo PI supernovae and leave no compact objects between $m_{\rm ZAMS} \sim 119$–$344\ M_\odot$ and $\sim$119–$230\ M_\odot$, respectively. The shaded area shows the PI mass gap, with the hatched regions corresponding to the uncertainty in current models (e.g., Farmer et al. 2019; Mapelli et al. 2020).

distances are distributed uniformly over comoving volume and time.

The time- and angle-averaged sensitive luminosity distances of the cWB-IMBHB search for mergers similar to GW190521 in O1, O2, and O3a data are 1.1, 1.2, and 1.7 Gpc, respectively, showing a substantial gain in sensitivity over successive runs. The combined searched time–volume over O1, O2, and O3a data is 9.1 Gpc^3 yr. Thus, taking a Jeffreys prior on the rate R as $p(R) \propto R^{-0.5}$, and with one event detected above threshold, we obtain an estimate $R = 0.13^{+0.3}_{-0.11}\ \mathrm{Gpc}^{-3}\ \mathrm{yr}^{-1}$.

This rate is below previous upper limits obtained by various methods: (mass- and spin-dependent) upper limits inferred from LIGO–Virgo searches of O1–O2 data, $0.20\ \mathrm{Gpc}^{-3}\ \mathrm{yr}^{-1}$ or greater (Abbott et al. 2019d); and limits obtained in Chandra et al. (2020) from numerical simulations of BBH signals with generic precessing spins added to O1 data, $0.36\ \mathrm{Gpc}^{-3}\ \mathrm{yr}^{-1}$ or greater. Our rate is also well below model-dependent limits of $\mathcal{O}(1)\ \mathrm{Gpc}^{-3}\ \mathrm{yr}^{-1}$ obtained in Fishbach et al. (2020) for possible BBH populations with $45 < m_1/M_\odot < 150$. Our estimate is for a population sharing the properties of GW190521; as we obtain more observations of high-mass BBH systems, we expect to better constrain the distribution of their masses and spins and thus refine the population rate estimate. The merger rate obtained here may be compared to expectations from possible formation channels, as in the following section.

5. Astrophysical Formation Channels and Implications for Stellar Collapse

Both the primary component mass and remnant mass of this system are higher than the previously most massive BBH detected by LSC and Virgo, GW170729 (Abbott et al. 2019i). Other candidate events, dubbed GW170817A and GW151205, have been identified in O1 and O2 data by other groups (Nitz et al. 2019; Zackay et al. 2019), with component masses higher than GW170729 if of astrophysical origin. Here we do not attempt to assess possible astrophysical implications of such additional events.

Our analysis of the BBH population detected in the O1 and O2 runs using parameterized models of the mass distribution indicates that 99% of merging BH primaries have masses below $45\ M_\odot$ (Fishbach & Holz 2017; Abbott et al. 2019h). As the primary mass of GW190521 is well above this value, the system is well within the highest-mass 1% of the population inferred from O1 and O2 observations. We obtain confirmation of the unexpected nature of GW190521 by generating synthetic catalogs of 25 (50) BBH detections to represent expectations for BBH detections in the first half of O3. The masses of synthetic detections are obtained via draws from the posterior of the O1–O2 population described by the most general model, Model C, of Abbott et al. (2019h), after applying selection effects. We then extract the highest-mass primary BH $m_{1,\rm max}$ and compare to the primary mass of GW190521. For the 25-event (50-event) synthetic catalogs, 0.6% (1.3%) of $m_{1,\rm max}$ values lie above 85 and 3.0% (5.3%) lie above 71 (the posterior median and 5th percentile estimated using the NRSur PHM model). Even when accounting for statistical uncertainties in the mass estimation (Fishbach et al. 2020), the primary mass of GW190521 is in tension with the population inferred from O1 and O2.

Figure 10 shows the mass of GW190521 in comparison with the masses of all the O1 and O2 BBHs (left panel) and with current theoretical knowledge about the PI mass gap (right panel). A set of evolutionary astrophysical models (Spera & Mapelli 2017) relating the progenitor mass and compact object is also shown for reference. The astrophysical models are subject to several uncertainties in stellar evolution and CCSNe and only serve as representative examples. This figure is an update of Figure 5 of Abbott et al. (2019h) to include the masses of GW150521.1 and the most recent uncertainty

estimates on the PI mass gap, which we review below in Section 5.1.

Several mechanisms could fill the PI gap. In the following sections, we discuss second-generation (2g) BHs, stellar mergers in young star clusters, and BH mergers in AGN disks. Second-generation BHs, i.e., BHs born from the merger of two BHs, can have mass in the PI gap (Miller & Hamilton 2002; Fishbach et al. 2017; Gerosa & Berti 2017; Rodriguez et al. 2019). If they are in a dense stellar environment and are not ejected by the gravitational recoil, they have a chance to form a new binary system with another BH (Gerosa & Berti 2019; Rodriguez et al. 2019). Alternatively, a merger between an evolved star (with a well-developed helium or carbon-oxygen core) and a main-sequence companion might trigger the formation of a giant star with an oversized envelope with respect to the core. If this star collapses into a BH before its helium core enters the PI range, then it can give birth to a BH in the PI gap (Di Carlo et al. 2019; Spera et al. 2019). If this BH is inside a dense stellar environment, it has a chance to capture a companion by dynamical exchange. BHs in AGN disks might pair with other BHs and are expected to merge efficiently owing to gas torques, producing 2g BHs (e.g., McKernan et al. 2018). These BHs in AGN disks might even grow by gas accretion (e.g., McKernan et al. 2012).

Finally, van Son et al. (2020) investigated the possibility that BHs in isolated binaries might have mass in the PI gap by super-Eddington accretion of the companion onto the primary BH. Even under the most extreme assumptions, they find that at most ∼2% of all merging BBHs in isolated binaries contain a BH with a mass in the PI mass gap, and they find no merging BBH with a total mass exceeding $100\,M_{\odot}$.

5.1. Uncertainties on PI and Stellar Evolution Theory

The physical processes leading to PI and PPI are well known, and a robust formalism to model them has been developed (e.g., Fowler & Hoyle 1964; Barkat et al. 1967; Ober et al. 1983; Bond et al. 1984; Heger et al. 2003; Woosley et al. 2007; Chen et al. 2014; Yoshida et al. 2016; Woosley 2017, 2019; Marchant et al. 2019). On the other hand, there are still uncertainties on the minimum helium-core mass for a star to undergo PPI: Woosley (2017) indicate $M_{\rm He,min} \approx 32\,M_{\odot}$, while Leung et al. (2019) suggest that this value should be raised to $M_{\rm He,min} \approx 40\,M_{\odot}$. This difference might translate into a significant difference in the maximum BH mass.

In addition to this, there are critical uncertainties on other physical ingredients that combine with PI and PPI to shape the mass spectrum of BHs (e.g., Belczynski et al. 2016, 2020; Stevenson et al. 2019). Recently, Farmer et al. (2019) and Renzo et al. (2020) have investigated the main sources of uncertainty on the lower edge of the PI mass gap, by modeling naked helium cores. The impact of time-dependent convection on the location of the lower edge of the PI mass gap is found to be $\Delta m \approx 5\,M_{\odot}$ (Renzo et al. 2020). Variations in the treatment of convective mixing and neutrino physics are found to have small effects on the maximum BH mass (with a mass variation $\Delta m \approx 1$–$2\,M_{\odot}$), while different stellar metallicity and wind mass-loss prescriptions have more conspicuous repercussions ($\Delta m \approx 4\,M_{\odot}$). Most importantly, the uncertainties on nuclear reaction rates have a dramatic impact on the maximum BH mass, which can change by $\Delta m \approx 16\,M_{\odot}$, corresponding to 30%–40% of the maximum BH mass. Most of the differences come from the $^{12}{\rm C}(\alpha,\gamma)^{16}{\rm O}$ reaction (Farmer et al. 2019; see also Takahashi et al. 2018). This result is particularly important if we consider that Farmer et al. (2019) explore only 1σ uncertainties (see, e.g., deBoer et al. 2017 for a recent review) and vary only a few nuclear reaction rates.

The maximum BH mass estimated by Farmer et al. (2019) is $\approx 56\,M_{\odot}$; however, they model pure helium cores, without hydrogen envelopes. Mapelli et al. (2020) show that accounting for the collapse of a residual hydrogen envelope can increase the maximum BH mass by $\approx 20\,M_{\odot}$ in the case of metal-poor ($Z \leqslant 0.0003$), slowly rotating progenitor stars. Hence, the final fate of the hydrogen envelope is an additional source of uncertainty, with an impact of $\Delta m \approx 20\,M_{\odot}$ on the maximum BH mass.

While mass transfer in close binaries is expected to remove most of the hydrogen envelope, metal-poor ($Z \leqslant 3 \times 10^{-4}$) single stars with zero-age main-sequence (ZAMS) mass $m_{\rm ZAMS} \lesssim 70\,M_{\odot}$ are expected to retain a significant fraction of their hydrogen envelope. If most of this hydrogen envelope collapses into the final compact object, the maximum BH mass is ∼60–65 $M_{\odot}$, while a naked helium core can produce BHs up to $\sim 45\,M_{\odot}$ (assuming median values for the nuclear reaction rates; Mapelli et al. 2020).

In summary, many sources of uncertainty affect our knowledge of the PI mass gap, the two principal ones being nuclear reaction rates ($\Delta m \approx 16\,M_{\odot}$) and the collapse of the hydrogen envelope ($\Delta m \approx 20\,M_{\odot}$). The combination of the main uncertainties has yet to be studied; therefore, it is not clear whether their effects sum up, as needed to explain the primary mass of GW190521. Based on these considerations, ∼60–65 $M_{\odot}$ is probably a conservative lower limit to the edge of the mass gap.

5.2. Hierarchical Merger Scenario

In this section, we discuss general properties of hierarchical mergers, i.e., mergers involving one or two second-generation BHs; we then present a Bayesian estimate of the relative probabilities (odds) that GW190521 is the product of a hierarchical BH merger, as opposed to a merger of first-generation (hereafter 1g) BHs. The masses of 2g BHs can fall in the PI gap: the merger remnant of GW170729 (Abbott et al. 2019i) is a previously reported example. A 2g BH is alone at birth, unless it was a member of a triple system that remains bound after the formation of the BH. However, a single 2g BH might acquire a companion through dynamical exchanges, if it forms in a dense cluster (Miller & Hamilton 2002; Colpi et al. 2003; Rodriguez et al. 2019), or through migration-mediated interactions in an AGN disk (McKernan et al. 2012; Bartos et al. 2017).

When formed, a 2g BH is subject to a relativistic gravitational recoil velocity (kick), which can eject it from its birthplace (Merritt et al. 2004); see Figure 4. For example, if a 2g BH forms in a dense star cluster, it might be retained in the cluster and subsequently acquire a new companion only if the local escape velocity is larger than $\gtrsim 50\,{\rm km\,s^{-1}}$ (Holley-Bockelmann et al. 2008; Antonini & Rasio 2016; O'Leary et al. 2016; Gerosa & Berti 2019). In this scenario, the companion might be a 1g BH or, less likely, a 2g BH (Rodriguez et al. 2019).

The relativistic kick at birth strongly depends on BH spin: maximally spinning BHs with spins in the orbital plane and counteraligned receive the largest kicks (e.g., Campanelli et al. 2007a, 2007b). Under the simplified assumption that all 1g

BHs are born with spin $\chi = 0$, then ~60% of 2g BHs are retained in a typical globular cluster, while if all 1g BH have $\chi = 0.5$, then less than 3% of merger products are retained (Rodriguez et al. 2019). For these reasons, hierarchical mergers are expected to be more likely in nuclear star clusters (e.g., Antonini & Rasio 2016; Arca Sedda et al. 2020), which have the highest escape velocity, rather than globular clusters or smaller stellar systems, such as open clusters and young star clusters.

Binaries with 2g BHs have several distinctive properties. The *mass of the primary* can be significantly larger than the lower boundary of the PI mass gap, although the exact distribution strongly depends on the 1g mass function (Chatziioannou et al. 2019; Gerosa & Berti 2019; Rodriguez et al. 2019; Doctor et al. 2020). Concerning the predicted *mass ratios*, 1g+2g mergers tend to have more unequal mass ratios than 2g+2g mergers (Rodriguez et al. 2019). The preference of GW190521 for a mass ratio $q \sim 1$ suggests that this system is more likely consistent with a 2g+2g merger than with a 1g+2g merger. Indeed, it is also conceivable for the system to be a merger of 1g BHs where one component was *above* the PI mass gap, though this is disfavored by the preference for near-equal masses (see Figure 8).

Spin measurements are a distinguishing feature of 2g BHs, because merger remnants are, on average, rapidly rotating with $\chi \sim 0.7$ (e.g., Baker et al. 2004; Buonanno et al. 2008; Lousto et al. 2010; Hofmann et al. 2016; Fishbach et al. 2017). Since they acquire companions through dynamical exchanges, spins are expected to be isotropically distributed with respect to the BBH orbital angular momentum (e.g., Mandel & O'Shaughnessy 2010; Rodriguez et al. 2016). A direct consequence of spatial isotropy is that the predicted distribution of effective spins is broad and symmetric about $\chi_{\rm eff} = 0$ (Farr et al. 2018; Gerosa & Berti 2019; Rodriguez et al. 2019; Kimball et al. 2020a). This prediction is broadly consistent with the range of $\chi_{\rm eff}$ and relatively large $\chi_{\rm p}$ values inferred for GW190521, reported in Section 2.2.

Finally, to estimate the predicted *merger rate* of PI BBHs from the hierarchical scenario, we should take into account that these mergers come from all kinds of star clusters with $v_{\rm esc} > 50\,{\rm km\,s^{-1}}$, hence both massive globular clusters and nuclear star clusters (or AGN disks). Considering only globular clusters and assuming that 1g BHs have zero spin, Rodriguez et al. (2019) find that ~3% of all mergers from globular clusters at redshift $z < 1$ have a component greater than $55\,M_\odot$, corresponding to 7% of the detectable BBHs from globular clusters.

5.2.1. Bayesian Analysis of Hierarchical Formation in Globular Clusters

We apply the method of Kimball et al. (2020b) to recover posteriors over the relative rates of 1g+2g and 2g+2g mergers to 1g+1g mergers, as well as the odds ratios that the GW190521 binary is of 1g+2g or 2g+2g origin, using our estimates of source component masses and spins within a physical model of the hierarchical merger process adapted to globular clusters. This analysis illustrates the many physical parameters and associated uncertainties that enter any inference on the origin of massive BBH.

We perform hierarchical Bayesian inference on a population model containing 1g+1g, 1g+2g, and 2g+2g mergers. For the first-generation BBH population, we adopt Model C in Abbott et al. (2019h): the mass distribution is a mixture of a truncated power law and a high-mass Gaussian component (Talbot & Thrane 2018), while the component spins follow nonsingular beta distributions with isotropic orientations. We also apply a theoretically motivated prior to the upper cutoff of the power-law mass component $m_{\rm max}$ to reflect expectations from stellar collapse dynamics, in particular PI (see Section 5.1). Considering uncertainties due to nuclear reaction rates (Farmer et al. 2019) and fallback dynamics (Mapelli et al. 2020), we take a prior Gaussian distribution over $m_{\rm max}$ with mean $50\,M_\odot$ and standard deviation $10\,M_\odot$. As mentioned above, we might also consider a 1g component *above* the PI mass gap, i.e., of $\sim 120\,M_\odot$; however, this would add complexity to the analysis while being unlikely to significantly alter the main outcome.

For simplicity, all 1g+1g mergers are here assumed to occur in environments that could potentially lead to subsequent mergers (Doctor et al. 2020). The 1g+2g and 2g+2g populations are formed by applying transfer functions from Kimball et al. (2020b) to the 1g+1g distributions, motivated by simulations reported in Rodriguez et al. (2019). The populations are combined into a mixture model by calculating branching ratios for the fraction of 1g+1g merger remnants that are retained in their cluster environments after receiving relativistic kicks at merger (calculated with the PRECESSION package of Gerosa & Kesden 2016; Gerosa 2016). The retention probability depends on the cluster escape velocity: as in Kimball et al. (2020b), we take a nominal cluster mass of $5 \times 10^5\,M_\odot$ with a Plummer radius of 1 pc (Harris 1996; Kremer et al. 2019); to quantify dependence on the escape velocity, we also consider a higher mass cluster of $10^8\,M_\odot$ representative of nuclear cluster environments.

The overall retention fraction is also highly sensitive to the 1g+1g spin magnitude distribution. Fuller & Ma (2019) find that a significant fraction of stellar BHs should form with near-zero natal spins; for BBHs formed in clusters via dynamical interaction we may also neglect any possible effect of strong stellar binary interactions on 1g BH spins. Thus, we also perform an analysis with an expanded model that includes an additional subpopulation of 1g BHs with zero spin, making up a fraction λ_0 of 1g+1g binary components. We quote results both with and without this zero-spin channel.

We apply our mixture models to a set of BBH observations consisting of GW190521 and all BBH detections from O1 and O2, performing inference on model hyperparameters using GWPOPULATION (Talbot et al. 2019) and Bilby (Ashton et al. 2019). In Figure 11, we plot the resulting marginalized Bayes factor of a given BBH being of xg+2g versus 1g+1g origin as a function of primary component mass and spin, together with the 90% and 68% credible regions for GW190521. Overall Bayes factors including dependence on both component masses and spins generally favor 2g+2g origin; the parameter estimation likelihood strongly favors near-equal component masses; thus, 1g+2g origin implying significantly unequal masses is disfavored by the data.

Figure 12 (orange contours) shows the relative rates of 1g+2g and 2g+2g mergers for the model without a 1g zero-spin subpopulation. We find $\log_{10}(\mathcal{R}_{\rm 1g+2g}/\mathcal{R}_{\rm 1g+1g})$ and $\log_{10}(\mathcal{R}_{\rm 2g+2g}/\mathcal{R}_{\rm 1g+1g})$ to be $-2.6^{+0.9}_{-1.1}$ and $-5.5^{+1.8}_{-2.2}$, respectively. Applying the priors given by the relative rates and marginalizing over system parameters and population hyperparameters, we calculate the odds ratio that the source of

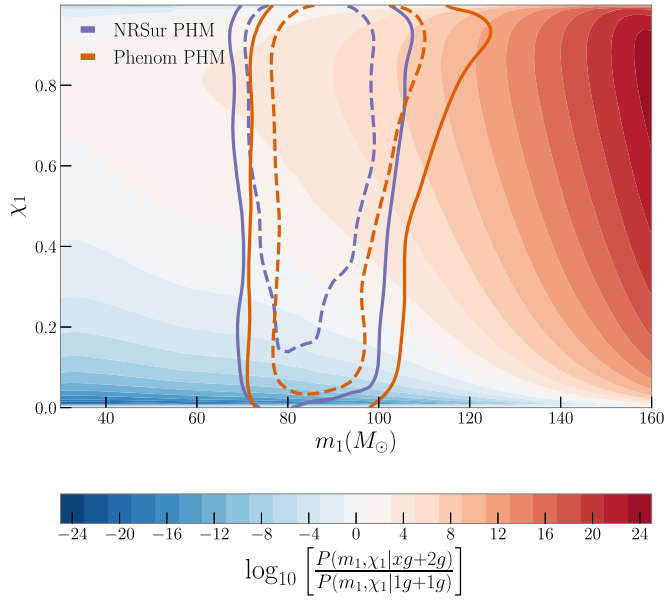

Figure 11. Marginalized Bayes factor for a BBH to be a second-generation merger (1g+2g or 2g+2g) as opposed to a first-generation BH merger, as a function of primary mass and spin, in the globular cluster analysis of Section 5.2.1 using a physically motivated prior cutoff on 1g BH masses. The Bayes factor contours correspond to component masses and spins inferred using the NRSur PHM model for GW190521 and differ only slightly from those found using the Phenom PHM model. We show the 90% and 68% posterior credible regions for GW190521 as solid and dashed contours, respectively, for both the NRSur PHM and Phenom PHM models.

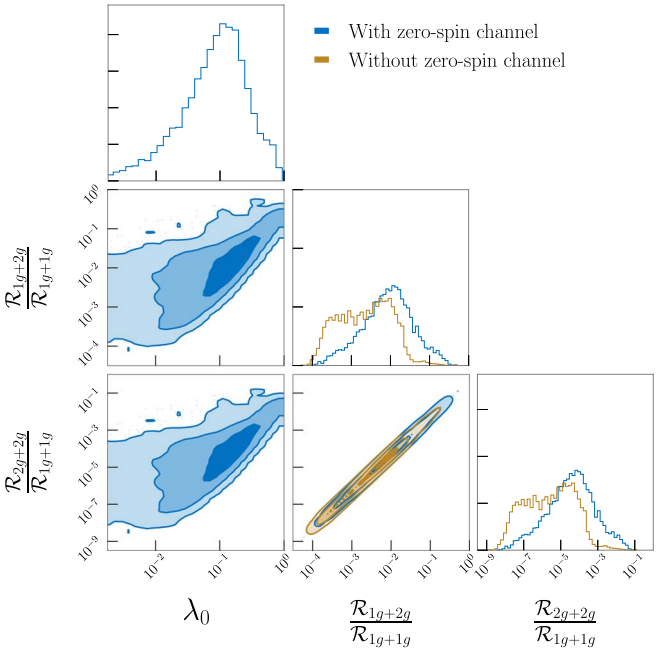

Figure 12. Relative rates of 1g+2g and 2g+2g as compared to first-generation mergers, in globular cluster models with (blue) and without (orange) a zero-spin stellar BH population (see Section 5.2.1), using GW190521 source parameters derived from NRSur PHM. In the model with zero-spin population, we also plot the fraction λ_0 of 1g+1g binary components belonging to this population.

GW190521 is a hierarchical merger, versus a 1g+1g merger. Our results, summarized in the top half of Table 2, are dependent on the waveform chosen to produce the parameter estimation samples, as well as assumptions on the 1g+1g spin and mass ratio distributions. Under these assumptions, we find that GW190521 is most likely to be of 1g+1g origin, because the merger remnants of BBHs with large component spins are often subject to kicks that eject them from low-mass clusters. Accounting for a possible 1g BH component *above* the mass gap, implying a significantly unequal-mass merger, would be unlikely to alter this conclusion.

Applying the model with a 1g zero-spin subpopulation yields higher retention fractions, due to lower merger recoil velocities, and higher relative hierarchical merger rates, shown in Figure 12 (blue contours): $\log_{10}(\mathcal{R}_{1g+2g}/\mathcal{R}_{1g+1g})$ and $\log_{10}(\mathcal{R}_{2g+2g}/\mathcal{R}_{1g+1g})$ become $-2.0^{+1.0}_{-1.2}$ and $-4.4^{+2.0}_{-2.4}$, respectively. When we include the zero-spin formation channel, the odds ratios for hierarchical origin, summarized in the bottom half of Table 2, increase by factors of ∼2–10, though we still favor GW190521 being due to a 1g+1g merger, for both the NRSur PHM and Phenom PHM parameter estimates. In this case, the estimated fraction λ_0 of merging 1g BHs from the zero-spin channel is in the range of ∼0.01–0.47.

We also consider a higher cluster mass of $10^8\,M_\odot$, which may be representative of nuclear cluster environments: the higher cluster mass increases the odds of hierarchical origin by 3–4 orders of magnitude, for both models with and without a zero-spin formation channel. For AGN environments essentially all 1g merger products are retained; however, quantitative assessment would require more detailed modeling of BH mergers in AGNs beyond their increased escape velocity, and the 1g+2g and 2g+2g population models we present here are tuned to globular cluster models.

Table 2
Odds Ratios for the Source of GW190521 Being a xg+2g Merger versus 1g +1g Merger, in the Globular Cluster Models of Section 5.2.1

No Zero-spin Channel	NRSur PHM	Phenom PHM
P(1g+2g):P(1g+1g)	0.28:1	0.28:1
P(2g+2g):P(1g+1g)	0.07:1	0.03:1
With Zero-spin Channel	**NRSur PHM**	**Phenom PHM**
P(1g+2g):P(1g+1g)	0.86:1	0.81:1
P(2g+2g):P(1g+1g)	0.68:1	0.23:1

In summary, the probability that GW190521 is due to a hierarchical merger in a stellar cluster is strongly dependent on the properties of 1g BHs in such environments, primarily on their mass and spin distributions and on the cluster escape velocity. With significantly larger event samples it may be possible to disentangle the different model parameters; thus, similar, high-mass BBH mergers constitute a future laboratory for BH populations and dynamics in cluster environments.

5.3. Stellar Merger Scenario

If a star grows an oversized hydrogen envelope with respect to its helium core, it might directly collapse to a BH with mass ∼60–100 $M_\odot$ without entering the PI/PPI regime (Bouffanais et al. 2019; Di Carlo et al. 2019; Spera et al. 2019). This scenario assumes that most of the hydrogen envelope collapses to a BH (see Sukhbold et al. 2016 for a discussion of the uncertainties). For a star to develop this oversized hydrogen envelope, one or more mergers between a helium-core giant and a main-sequence companion are required (Di Carlo et al. 2020). As in the hierarchical merger scenario, a BH born from a stellar merger is alone at birth, unless it was a member of a triple system that remains bound. In the field the BH remains

alone, while in a young star cluster, a globular cluster, or a nuclear star cluster the BH can acquire a companion through exchanges. A further variation of this model is that GW190521 formed in a triple or multiple stellar system. The inner binary star of the triple might have merged, producing the primary BH via the stellar merger mechanism described above. If the outer member is massive enough, it might then collapse, becoming the secondary BH. The most critical aspect of a triple origin for GW190521 is the orbit of the tertiary body.

The *primary mass* distribution predicted by the stellar merger model scales approximately as m^{-5} with $m > 60\,M_{\odot}$. The expected *mass ratio* is most likely $q \sim 0.4$–0.6, but all mass ratios between $q \sim 0.04$ and $q \sim 1$ are possible (Di Carlo et al. 2020). Hence, the primary mass and the mass ratio predicted by this scenario are compatible with the properties of GW190521.

If the angular momentum of the core of the massive progenitor is not dissipated efficiently, this scenario predicts a high primary *spin*. Since this is a dynamical formation scenario, spin orientations are expected to be isotropically distributed. As we already discussed for the hierarchical scenario (Section 5.2), an isotropic spin distribution is consistent with the fact that GW190521 has a low $\chi_{\rm eff}$ and a relatively large $\chi_{\rm p}$.

Finally, Di Carlo et al. (2019) predict that up to ∼2% of all BBH mergers from young star clusters involve BHs in the PI mass gap born from (multiple) stellar mergers. These represent $\lesssim$10% of all detectable mergers from star clusters. As noted in Jani & Loeb (2020), $\lesssim$0.8% of all massive stars contribute to a BBH merger population in the PI mass gap.

In summary, the primary mass, mass ratio, effective spin, and precession spin parameters of GW190521 are consistent with the stellar merger scenario in star clusters. The key difference between the hierarchical merger scenario and the stellar merger scenario is that the latter does not imply relativistic kicks at birth; hence, it might be at least one order of magnitude more common in star clusters. On the other hand, the details of the stellar merger scenario depend on delicate assumptions about stellar mergers (e.g., that most mass is retained by the merger product) and massive star evolution (e.g., stellar rotation).

5.4. AGN Disk Scenario

The nucleus of an active galaxy might harbor tens of thousands of stellar-mass BHs that moved into the innermost parsec owing to mass segregation (Bahcall & Wolf 1977; Morris 1993; Miralda-Escudé & Gould 2000; Antonini 2014; Hailey et al. 2018; Generozov et al. 2018). In this dense gaseous environment, BH orbits are efficiently torqued by gas drag until they align with the AGN disk (Bartos et al. 2017; McKernan et al. 2018). Once in the disk, BHs can accrete gas, and they are expected to acquire companions and efficiently merge with them as an effect of gas torques (McKernan et al. 2012, 2014, 2020; Bellovary et al. 2016; Bartos et al. 2017). When these BHs merge with other BHs, there is a high chance that they are not ejected, because of the high escape velocity in galactic nuclei (thousands of kilometers per second, given the proximity to an SMBH). Hence, AGN disks might easily harbor 2g BHs (Yang et al. 2019a).

As a consequence of the joint contribution of gas accretion, BBH mergers, and high escape velocities, a fraction of BHs in AGN disks are expected to have masses in the PI mass gap or even in the IMBH regime (McKernan et al. 2012). Recent work suggests that they have a mass function similar to a power law, but significantly flatter than field BHs (Yang et al. 2019b), or even reminiscent of a broken power law (McKernan et al. 2018; Yang et al. 2019a). The possible *mass ratios* are highly uncertain, though most mergers have mass ratios less extreme than 10:1 (McKernan et al. 2018; Yang et al. 2019a).

As to the *spin* magnitudes, we expect large spins ($\chi \sim 0.7$) if BHs in AGN disks are 2g BHs. Since BH orbits tend to align with the AGN disk, there might be some preferential alignment in the spins of BBHs (McKernan et al. 2012). Unlike the other possible scenarios, BBH mergers in an AGN disk may have an associated electromagnetic counterpart (an ultraviolet flare; McKernan et al. 2019). No prompt electromagnetic counterpart has been reported for GW190521 (e.g., Barthelmy et al. 2019; Casentini et al. 2019; Doyle et al. 2019a, 2019b; Lipunov et al. 2019; Negoro et al. 2019; Turpin et al. 2019a, 2019b; Watson et al. 2019), but see Graham et al. (2020), which appeared during the revision of this work, for a possible candidate optical counterpart.

Finally, the fraction of BBHs in the PI mass gap born in AGN disks might be large: Yang et al. (2019a) suggest that 40% of all AGN-assisted mergers detected by LIGO–Virgo will include a BH with mass $\gtrsim 50\,M_{\odot}$; on the other hand, the overall contribution of AGN disks to the BBH merger rate might be low. Most works suggest a total merger rate of ∼1–10 $\mathrm{Gpc^{-3}\,yr^{-1}}$ (e.g., Bartos et al. 2017; Stone et al. 2017; Yang et al. 2019b; Arca Sedda 2020), while McKernan et al. (2018) and Tagawa et al. (2020) try to quantify additional uncertainties and end up with merger rates of $\sim 10^{-3}$–10^{4} $\mathrm{Gpc^{-3}\,yr^{-1}}$ and ∼0.02–60 $\mathrm{Gpc^{-3}\,yr^{-1}}$, respectively.

6. Alternative Scenarios

The short duration and bandwidth of the signal observed in the data open the possibility that the source may not be uniquely explained as an unusually massive, quasi-circular BBH merger formed via astrophysical processes. Furthermore, given a transient GW signal for which a full inspiral-merger-ringdown morphology is not directly evident in the data, a natural question is whether the signal may be consistent with other types of modeled GW source. We consider several possible alternative scenarios below; all are disfavored either by the data, or by low prior probability of the alternative hypothesis, or by both.

6.1. Eccentricity and Head-on Collisions

The waveform observed in the data may also be consistent with the merger of a BBH with nonzero orbital eccentricity. The short duration of the signal makes it difficult to distinguish the amplitude modulation associated with precession from that due to eccentric orbits, or even head-on collisions (mergers that happen immediately at closest approach; Calderón Bustillo et al. 2020). More quantitative evaluation of this issue requires further development of accurate and computationally efficient eccentric waveforms and is thus deferred to future work. Efforts to efficiently detect and estimate the parameters for eccentric compact binaries are under development (Lower et al. 2018; Romero-Shaw et al. 2019; Lenon et al. 2020).

From an astrophysical perspective, BBHs with eccentricity $e \gtrsim 0.1$ at merger are deemed to be almost impossible from isolated binary evolution but might account for ∼1% of all

BBH mergers in globular clusters and other dense star clusters (Gültekin et al. 2006; Samsing et al. 2014, 2018; Samsing & Ramirez-Ruiz 2017; Rodriguez et al. 2018; Samsing 2018; Samsing & D'Orazio 2018; Zevin et al. 2019; Fragione et al. 2020). Head-on collisions are even more rare owing to the small geometric cross section of individual BHs (Samsing et al. 2014).

The high concentration of BHs in nuclear star clusters might produce a population of extremely eccentric BBHs from single–single BH capture by GW radiation (O'Leary et al. 2009; Gondán et al. 2018), although the cross section for this process is orders of magnitude lower than the cross section for a binary—single encounter (Samsing et al. 2014). Finally, Kozai–Lidov resonances (Kozai 1962; Lidov 1962) in triple systems might also trigger eccentric BBHs in the field (Antognini et al. 2014; Antonini et al. 2017; Silsbee & Tremaine 2017) or in dense star clusters (Wen 2003; Antonini & Perets 2012; Antonini et al. 2016; Kimpson et al. 2016; Hoang et al. 2018). Considering that ∼25% of massive stars are members of triple systems (Sana et al. 2014), Antonini et al. (2017) estimate a merger rate of ∼0.3–2.5 $\mathrm{Gpc^{-3}\,yr^{-1}}$ from isolated resonating triple systems, up to ∼5% of which retain high eccentricity at merger.

Most of the formation channels that can explain the mass of the primary BH in GW190521 are based on dynamical encounters in dense star clusters and allow for the formation of eccentric BBHs. Hence, even if eccentric BBH mergers are estimated to be extremely rare, we cannot exclude that the source binary of GW190521 has nonzero eccentricity.

6.2. Strong Gravitational Lensing

Another possible explanation for the apparent inconsistency of GW190521 with formation from stellar collapse is gravitational lensing of the signal by galaxies or galaxy clusters (Broadhurst et al. 2018; Li et al. 2018; Ng et al. 2018; Oguri 2018; Smith et al. 2018). If GW190521 is a strongly lensed signal, it will receive a magnification μ defined such that GW amplitude is increased by a factor $\mu^{1/2}$ relative to the unlensed case. For a given observed GW signal, the luminosity distance to the source, and thus its redshift, may then be much larger than in the absence of lensing. Strong lensing is expected to be relatively rare at current detector sensitivities, with 1 in every 100–1000 detected events strongly lensed by individual galaxies (Holz & Wald 1998; Li et al. 2018; Ng et al. 2018; Oguri 2018) and a similarly low rate for lensing by galaxy clusters (Smith et al. 2018; Oguri 2019).

Under the strong-lensing hypothesis $\mathcal{H}_L$, we assume that the event comes from a BBH population of stellar collapse origin and infer its magnification, redshift, and component masses. The posterior distribution of the parameters is (Pang et al. 2020)

$$p(\mu, \vartheta|d, \mathcal{H}_L) \propto p(d|\vartheta)p(\vartheta|\mu, \mathcal{H}_L)p(\mu|\mathcal{H}_L), \quad (1)$$

where ϑ are the apparent parameters of the waveform received at the detector, which differ from the source-frame parameters owing to effects of redshift and lensing. For the prior over component masses and redshift of the source $p(m_1, m_2, z|\mathcal{H}_L)$, we take a binary BH population model from those used in Abbott et al. (2019h) for O1 and O2 observations, with fixed population parameters $\lambda = 0$, $\alpha = 1$, $\beta_q = 0$, $m_{\rm min} = 5\,M_\odot$, multiplied by the optical depth of lensing by galaxies $\tau(z) = 4.17 \times 10^{-6}\ (D_c(z)/\mathrm{Gpc})^3$ (Haris et al. 2018), where D_c is the comoving distance. For the primary mass upper cutoff $m_{\rm max}$ we consider two different values to account for uncertainties in the edge of the PISN gap, $m_{\rm max} = (50, 65)\,M_\odot$. We use the lensing prior $p(\mu|\mathcal{H}_L) \propto \mu^{-3}$ (Blandford & Narayan 1986) with a lower limit $\mu > 2$ appropriate to strong lensing. We adopt the NRSur PHM waveform model. The resulting magnification estimate is mostly sensitive to the measurement of the component masses.

We find that the required magnification under the lensing hypothesis, taking $m_{\rm max} = 50\,M_\odot$ ($m_{\rm max} = 65\,M_\odot$), is 13^{+54}_{-8} (6^{+28}_{-4}), with source-frame masses $43^{+6}_{-16}\,M_\odot$ ($55^{+9}_{-22}\,M_\odot$) and $35^{+11}_{-15}\,M_\odot$ ($44^{+14}_{-19}\,M_\odot$) at redshift $2.5^{+2.1}_{-0.7}$ ($1.8^{+1.7}_{-0.6}$). At these redshifts, the lensing optical depth is low: $9^{+10}_{-3} \times 10^{-4}$ ($5^{+9}_{-3} \times 10^{-4}$).

One possible signature of strong lensing would be multiple GW images, which may give rise to two events occurring closer in time than expected for a Poisson process of BBH mergers, and with consistent sky localization and intrinsic parameters. Another candidate GW signal, S190521r (Abbott et al. 2019c), was reported 4.6 hr after GW190521; however, the two events' sky localizations strongly disfavor lensing, showing no overlap (Haris et al. 2018; Hannuksela et al. 2019; Singer et al. 2019). Any lensed counterpart image could, though, have been too weak to be confidently detected and may have arrived at a larger time separation or when the detectors were not operating. Moreover, in the case of galaxy cluster lensing, the counterpart could appear at a separation of years in time (Smith et al. 2018).

Given the low expected lensing rate and optical depth and the absence of an identifiable multi-image counterpart close to GW190521, our current analyses find no evidence in favor of the strong-lensing hypothesis. Future analyses using subthreshold searches and multi-image searches on all event pairs may yield better constraints on strong lensing (Haris et al. 2018; Hannuksela et al. 2019; Li et al. 2019; McIsaac et al. 2019).

6.3. Primordial BH Mergers

Primordial BHs (PBHs; Carr & Hawking 1974; Khlopov 2010) are thought to be formed from collapse of dark matter overdensities in the very early universe (at redshifts $z > 20$, i.e., before the formation of the first stars) and may account for a nontrivial fraction of the density of the universe (Carr et al. 2016; Clesse & García-Bellido 2017). Since the binary components of GW190521 are unlikely both to have formed directly from stellar collapse, it is possible that they may be of PBH origin (Bird et al. 2016); however, theoretical expectations of the mass distribution and merger rate of PBH binaries have large uncertainties (e.g., Byrnes et al. 2018), so we do not attempt to quantify such scenarios. Some theories of PBH formation predict predominantly small component spins $\chi \ll 1$ (Chiba & Yokoyama 2017), which are disfavored by our parameter estimates for GW190521 (Section 2.2 and Figure 2).

6.4. Cosmic String Signal Models

Cosmic string cusps and kinks (e.g., Damour & Vilenkin 2000) may yield short-duration transient signals (bursts) with support at low frequency (e.g., Divakarla et al. 2019, Section IV D). There has been no previous detection of a

cosmic string GW burst (Aasi et al. 2014b; Abbott et al. 2018b), and bounds on cosmic string model parameters derived from the overall contribution to the GW stochastic background are generally more stringent by orders of magnitude than bounds from direct burst searches (Abbott et al. 2018b, 2019a). Thus, detection of a burst signal in current data is a priori unlikely; however, we consider this possibility for completeness. Here we estimate the likelihood for the data to be produced by a cosmic string signal and compare this with binary BH merger models as described in previous sections.

GW190521 is identified by the cosmic string matched filter search pipeline (Aasi et al. 2014b; Abbott et al. 2018b); however, the maximum S/Ns in this search (∼6 and ∼8 in LIGO Hanford and Livingston, respectively) are much lower than for modeled BBH search templates, best-fit binary merger waveform models, or unmodeled reconstructions, suggesting that the data strongly prefer a binary merger model to a cosmic string or cusp. In addition, the signal appears inconsistent with the cosmic string template, as evidenced by large values of the χ^2 test statistic, over 7 (3) in LIGO Livingston (Hanford), while the expected value for a cosmic string signal is unity. Figure 13 illustrates the mismatch between the best-matching cusp waveform and the Livingston data.

As a refinement of this analysis accounting for parameter uncertainties and phase-space volumes for different models, we compare the Bayes factors for a BBH waveform model to cosmic string cusp and kink models, respectively. Since the true rates of binary mergers in the mass range of GW190521 and of cosmic string transient signals are both unknown, we do not attempt to quantify prior odds for the two hypotheses. We use methods and models, including priors on cosmic string signal parameters, detailed in Divakarla et al. (2019). For the BBH model, we use the NRSur PHM waveform model with priors on component masses, spins, and distance matching those in Section 2. Using the `dynesty` nested sampling algorithm (Speagle 2020) within Bilby (Ashton et al. 2019; Romero-Shaw et al. 2020), we find Bayes factors $\log_{10} B^{\rm BBH}_{\rm cusp} = 29.8$ and $\log_{10} B^{\rm BBH}_{\rm kink} = 29.7$, strongly favoring the BBH hypothesis; thus, it is highly unlikely that this event was of cosmic string origin.

6.5. CCSN Signal Models

CCSN signals modeled in multidimensional simulations (e.g., Mezzacappa et al. 2020; O'Connor & Couch 2018; Andresen et al. 2019; Powell & Müller 2019) are of long duration (up to 1.5 s), may be broadband (from few Hz to around 1–2 kHz), and do not have morphology similar to GW190521. Such signals are expected to be detectable for sources within a distance of a few tens of kiloparsecs from Earth (Abbott et al. 2020d). We expect a CCSN signal to have electromagnetic and neutrino counterparts; however, no counterpart has been observed within a few hundred kiloparsecs (IceCube Collaboration 2019). GWs from extreme emission CCSNe, produced by highly deformed, rapidly rotating or fragmented cores, could be observed at a range of a few tens of megaparsecs (Abbott et al. 2020d). At that distance we do not expect to detect neutrinos; however, a detection of GWs produced by these extreme emission scenarios is overall very unlikely, and an electromagnetic counterpart would still be expected. It is thus implausible that the GW190521 signal was produced by CCSNe.

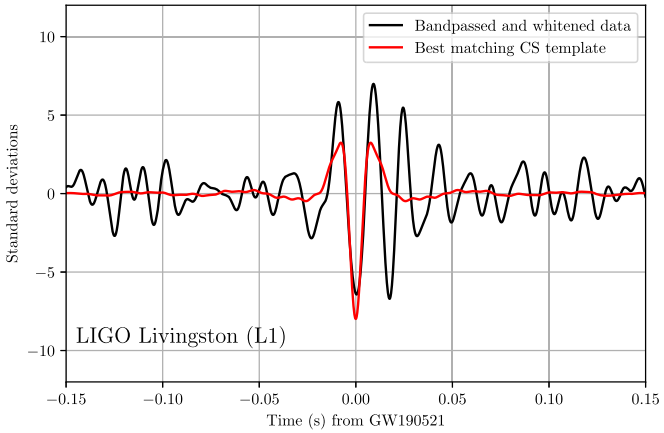

Figure 13. The LIGO Livingston strain data time series is shown in dark gray. The best-matching cosmic string cusp template is shown in red. Both are whitened using the detector's noise spectrum; the strain data are additionally bandpassed between 20 and 128 Hz to suppress noise well above the frequency support of the template.

7. Summary and Conclusions

The GW signal GW190521 observed by the Advanced LIGO and Advanced Virgo detectors is consistent with emission from the coalescence of a high-mass BBH system. Under that assumption, at least one of the component BHs in the binary has a mass in the PI mass gap with high probability, and the final merged BH has a mass in the IMBH range. There is no conclusive previous evidence from electromagnetic observations for the existence of IMBHs in this mass range (∼100–1000 $M_\odot$).

The signal is well described by waveforms derived from GR incorporating spin-induced orbital precession and higher-order multipoles, but neglecting orbital eccentricity. There is only weak evidence for the effects of orbital precession in the signal, and there is moderate but not conclusive evidence for high spin components in the orbital plane. The Bayes factor for the presence of higher-order multipoles is slightly negative, disfavoring their presence; however, their inclusion enables more precise estimates of the source's component masses, distance, and inclination to the line of sight.

Several tests demonstrate the consistency of the signal with GR predictions, including agreement between full inspiral-merger-ringdown waveforms derived from NR and ringdown-only waveforms formed by summing the quasi-normal modes of the final Kerr BH. Because of the short duration and low bandwidth of the observed signal, possible sources other than a quasi-circular, high-mass BBH merger may be considered. Initial studies using waveforms that include orbital eccentricity suggest a partial degeneracy between eccentricity significantly greater than 0.1 and precession; however, significant eccentricity is disfavored by a low prior probability. The possibility that the signal is from a cosmic string cusp or kink is considered, but the signal is a poor match to waveform models from such sources. Finally, the possibility of the source being a CCSN is considered; this is disfavored by the lack of any counterpart electromagnetic or neutrino signal for CCSNe.

We discussed various scenarios for the formation and evolution of such a massive system. Uncertainties on the PI mass gap might justify the formation of BHs with mass $>65\,M_\odot$ from stellar collapse. Alternatively, the primary BH might be the result of the merger of two smaller BHs (hierarchical scenario), or of two massive stars. The mild

evidence for precession suggests a dynamical formation scenario, which predicts nearly isotropic spin orientation, such as the hierarchical BH merger or the outcome of a stellar merger in star clusters. The formation of GW190521 via isolated binary evolution appears disfavored.

Finally, we considered the possibilities that GW190521 is a strongly lensed signal from a lower-mass, high-redshift BBH merger, or that the system is a binary of primordial BHs (formed in the early universe). The mass of the system, the mass ratio, and the merger rate derived for this event are consistent with all of these scenarios, although the prior probability of strong lensing is low.

It is not possible to conclude at this time whether GW190521 represents the first of a new population of BBHs or is merely at the high-mass end of the population of BBH systems already observed by LIGO and Virgo. A future publication will address this question in the context of the larger sample of BBH events observed in the first half of the LIGO–Virgo O3 run, O3a (2019 April 1 through October 1). The answer, whether positive or negative, has the potential to provide new insights into the population and evolution of the most massive stars. We look forward to observing more binary mergers with high mass to further inform our understanding of these phenomena.

In upcoming future observing runs (Abbott et al. 2018c) we expect the global advanced detector network's sensitivity to BBH mergers to increase significantly, with potentially several hundreds of detections per year, reaching out to redshifts of a few or more. We may thereby observe a large sample of events similar to GW190521, which will constitute a unique source of information on the binary formation environments and channels, and on the dynamics and evolution of massive stellar BHs over cosmic history. This will enable us to address questions such as the natal spin and mass distribution of BHs as a product of stellar collapse dynamics including PI, stellar cluster masses and dynamics, merger kicks due to GW emission, and tests of GR for highly spinning BHs.

The evidence for high-mass BBHs and IMBH binaries advances the science case for enhanced sensitivity at lower GW frequencies ($\lesssim$5 Hz). The proposed next-generation ground-based GW detectors, such as Einstein Telescope (Punturo et al. 2010) and Cosmic Explorer (Abbott et al. 2017c; Reitze et al. 2019), can observe events similar to GW190521 up to a redshift of $\sim$20 (Gair et al. 2011; Jani et al. 2020). Such potential observations at high redshift can probe the dynamics and evolution of massive stellar BHs over cosmic history. GW190521 also motivates the possibility for multiband GW observations (Fregeau et al. 2006; Miller 2009; Sesana 2016; Jani et al. 2020) between ground-based detectors and upcoming space-based detectors like LISA (Amaro-Seoane et al. 2017). Such joint observations will provide a unique opportunity to test GR with highly spinning BHs (Vitale 2016) and probe binary formation environments and channels through measurements of spin evolution and eccentricity (Cutler et al. 2019).

The authors gratefully acknowledge the support of the United States National Science Foundation (NSF) for the construction and operation of the LIGO Laboratory and Advanced LIGO, as well as the Science and Technology Facilities Council (STFC) of the United Kingdom, the Max-Planck-Society (MPS), and the State of Niedersachsen/Germany for support of the construction of Advanced LIGO and construction and operation of the GEO600 detector. Additional support for Advanced LIGO was provided by the Australian Research Council. The authors gratefully acknowledge the Italian Istituto Nazionale di Fisica Nucleare (INFN), the French Centre National de la Recherche Scientifique (CNRS), and the Netherlands Organization for Scientific Research, for the construction and operation of the Virgo detector and the creation and support of the EGO consortium. The authors also gratefully acknowledge research support from these agencies, as well as by the Council of Scientific and Industrial Research, the Department of Science and Technology, the Science & Engineering Research Board (SERB), and the Ministry of Human Resource Development, India; the Spanish Agencia Estatal de Investigación, the Vicepresidència i Conselleria d'Innovació Recerca i Turisme and the Conselleria d'Educació i Universitat del Govern de les Illes Balears, the Conselleria d'Innovació Universitats, Ciència i Societat Digital de la Generalitat Valenciana, and the CERCA Programme Generalitat de Catalunya, Spain; the National Science Centre of Poland; the Swiss National Science Foundation (SNSF); the Russian Foundation for Basic Research; the Russian Science Foundation; the European Commission; the European Regional Development Funds (ERDF); the Royal Society; the Scottish Funding Council; the Scottish Universities Physics Alliance; the Hungarian Scientific Research Fund (OTKA); the French Lyon Institute of Origins (LIO); the Belgian Fonds de la Recherche Scientifique (FRS-FNRS), Actions de Recherche Concertées (ARC), and Fonds Wetenschappelijk Onderzoek—Vlaanderen (FWO), Belgium; the Paris Île-de-France Region; the National Research, Development and Innovation Office Hungary (NKFIH); the National Research Foundation of Korea; Industry Canada and the Province of Ontario through the Ministry of Economic Development and Innovation; the Natural Science and Engineering Research Council Canada; the Canadian Institute for Advanced Research; the Brazilian Ministry of Science, Technology, Innovations, and Communications; the International Center for Theoretical Physics South American Institute for Fundamental Research (ICTP-SAIFR); the Research Grants Council of Hong Kong; the National Natural Science Foundation of China (NSFC); the Leverhulme Trust; the Research Corporation; the Ministry of Science and Technology (MOST), Taiwan; and the Kavli Foundation. The authors gratefully acknowledge the support of the NSF, STFC, INFN, and CNRS for provision of computational resources.

We would like to thank all of the essential workers who put their health at risk during the COVID-19 pandemic, without whom we would not have been able to complete this work.

Strain data from the LIGO and Virgo detectors associated with GW190521 can be found in Abbott et al. (2020c). This document has been assigned the LIGO document No. LIGO-P2000021.

References

Aasi, J., Abbott, B. P., Abbott, R., et al. 2015, CQGra, 32, 074001
Aasi, J., Abbott, B. P., Abbott, R., et al. 2014a, PhRvD, 89, 122003
Aasi, J., Abadie, J., Abbott, B. P., et al. 2014b, PhRvL, 112, 131101
Abadie, J., Abbott, B. P., Abbott, R., et al. 2012, PhRvD, D85, 102004
Abbott, B. P., Abbott, R., Abbott, T. D., et al. 2016a, PhRvD, 94, 064035
Abbott, B. P., Abbott, R., Abbott, T. D., et al. 2016b, ApJL, 833, L1
Abbott, B. P., Abbott, R., Abbott, T. D., et al. 2016c, PhRvL, 116, 221101
Abbott, B. P., Abbott, R., Abbott, T. D., et al. 2017d, PhRvL, 119, 161101
Abbott, B. P., Abbott, R., Abbott, T. D., et al. 2019i, PhRvX, 3, 031040
Abbott, B. P., Abbott, R., Abbott, T. D., et al. 2019d, PhRvD, 100, 064064
Abbott, B. P., Abbott, R., Abbott, T. D., et al. 2019h, ApJL, 882, L24

Abbott, B. P., Abbott, R., Abbott, T. D., et al. 2018c, LRR, 21, 57
Abbott, B. P., Abbott, R., Abbott, T. D., et al. 2016a, PhRvL, 116, 241102
Abbott, B. P., Abbott, R., Abbott, T. D., et al. 2016b, ApJL, 832, L21
Abbott, B. P., Abbott, R., Abbott, T. D., et al. 2017a, PhRvD, D96, 022001
Abbott, B. P., Abbott, R., Abbott, T. D., et al. 2017b, PhRvL, 118, 221101
Abbott, B. P., Abbott, R., Abbott, T. D., et al. 2017c, CQGra, 34, 044001
Abbott, B. P., Abbott, R., Abbott, T. D., et al. 2018a, Gravitational Wave Open Science Center, The 01 Data Release, doi:10.7935/K57P8W9D
Abbott, B. P., Abbott, R., Abbott, T. D., et al. 2018b, PhRvD, D97, 102002
Abbott, B. P., Abbott, R., Abbott, T. D., et al. 2019b, GCN, 24621, 1
Abbott, B. P., Abbott, R., Abbott, T. D., et al. 2019c, GCN, 24632, 1
Abbott, B. P., Abbott, R., Abbott, T. D., et al. 2019e, Gravitational Wave Open Science Center, doi:10.7935/CA75-FM95
Abbott, B. P., Abbott, R., Abbott, T. D., et al. 2019f, GCN, 24640, 1
Abbott, B. P., Abbott, R., Abbott, T. D., et al. 2019g, PhRvD, 100, 104036
Abbott, R., Abbott, R., Abbott, T. D., et al. 2020e, ApJL, 896, L44
Abbott, B. P., Abbott, R., Abbott, T. D., et al. 2020d, PhRvD, 101, 084002
Abbott, B. P., Abbott, R., Abbott, T. D., et al. 2020f, CQGra, 37, 055002
Abbott, B., Abbott, R., Abbott, T. D., et al. 2019a, PhRvD, 100, 061101
Abbott, B. P., Abbott, T. D., Abraham, S., et al. 2020a, PhRvD, 102, 043015
Abbott, B. P., Abbott, T. D., Abraham, S., et al. 2020c, Gravitational Wave Open Science Center GW190521 data release, (doi: 10.7935/1502-wj52)
Abbott, R., Abbott, T. D., Abraham, S., et al. 2020b, PhRvD, 125, 101102
Acernese, F., Agathos, M., Agatsuma, K., et al. 2015, CQGra, 32, 024001
Acernese, F., Agathos, M., Aiello, L., et al. 2019, PhRvL, 123, 231108
Ade, P. A. R., Aghanim, N., Arnaud, M., et al. 2016, A&A, 594, A13
Agathos, M., Del Pozzo, W., Li, T. G. F., et al. 2014, PhRvD, 89, 082001
Ajith, P., Hannam, M., Husa, S., et al. 2011, PhRvL, 106, 241101
Amaro-Seoane, P., Audley, H., Babak, S., et al. 2017, arXiv:1702.00786
Anderson, J., & van der Marel, R. P. 2010, ApJ, 710, 1032
Andresen, H., Müller, E., Janka, H. T., et al. 2019, MNRAS, 486, 2238
Antognini, J. M., Shappee, B. J., Thompson, T. A., & Amaro-Seoane, P. 2014, MNRAS, 439, 1079
Antonini, F. 2014, ApJ, 794, 106
Antonini, F., Chatterjee, S., Rodriguez, C. L., et al. 2016, ApJ, 816, 65
Antonini, F., & Perets, H. B. 2012, ApJ, 757, 27
Antonini, F., & Rasio, F. A. 2016, ApJ, 831, 187
Antonini, F., Toonen, S., & Hamers, A. S. 2017, ApJ, 841, 77
Arca Sedda, M. 2020, ApJ, 891, 47
Arca Sedda, M., Mapelli, M., Spera, M., Benacquista, M., & Giacobbo, N. 2020, ApJ, 894, 133
Arun, K. G., Buonanno, A., Faye, G., & Ochsner, E. 2009, PhRvD, 79, 104023
Ashton, G., Hübner, M., Lasky, P. D., et al. 2019, ApJS, 241, 27
Babak, S., Taracchini, A., & Buonanno, A. 2017, PhRvD, 95, 024010
Bahcall, J. N., & Wolf, R. A. 1977, ApJ, 216, 883
Baker, J., Campanelli, M., Lousto, C. O., & Takahashi, R. 2004, PhRvD, 69, 027505
Baldassare, V. F., Reines, A. E., Gallo, E., et al. 2016, ApJ, 829, 57
Baldassare, V. F., Reines, A. E., Gallo, E., & Greene, J. E. 2015, ApJL, 809, L14
Baldassare, V. F., Reines, A. E., Gallo, E., & Greene, J. E. 2017, ApJ, 836, 20
Ball, W. H., Tout, C. A., Żytkow, A. N., & Eldridge, J. J. 2011, MNRAS, 414, 2751
Barkat, Z., Rakavy, G., & Sack, N. 1967, PhRvL, 18, 379
Barth, A. J., Greene, J. E., & Ho, L. C. 2005, ApJL, 619, L151
Barth, A. J., Ho, L. C., Rutledge, R. E., & Sargent, W. L. W. 2004, ApJ, 607, 90
Barthelmy, S. D., Lien, A. Y., Palmer, D. M., et al. 2019, GCN, 24646, 1
Bartos, I., Kocsis, B., Haiman, Z., & Márka, S. 2017, ApJ, 835, 165
Baumgardt, H., He, C., Sweet, S. M., et al. 2019, MNRAS, 488, 5340
Begelman, M. C. 2010, MNRAS, 402, 673
Begelman, M. C., Volonteri, M., & Rees, M. J. 2006, MNRAS, 370, 289
Belczynski, K., Heger, A., Gladysz, W., et al. 2016, A&A, 594, A97
Belczynski, K., Klencki, J., Fields, C. E., et al. 2020, A&A, 636, A104
Bellovary, J. M., Mac Low, M.-M., McKernan, B., & Ford, K. E. S. 2016, ApJL, 819, L17
Berti, E., Cardoso, V., & Starinets, A. O. 2009, CQGra, 26, 163001
Berti, E., Cardoso, V., & Will, C. M. 2006, PhRvD, 73, 064030
Berti, E., Yagi, K., Yang, H., & Yunes, N. 2018, GReGr, 50, 49
Bhagwat, S., Forteza, X. J., Pani, P., & Ferrari, V. 2020, PhRvD, 101, 044033
Bird, S., Cholis, I., Muñoz, J. B., et al. 2016, PhRvL, 116, 201301
Blanchet, L. 2014, LRR, 17, 2
Blanchet, L., Damour, T., Esposito-Farèse, G., & Iyer, B. R. 2005, PhRvD, 71, 124004
Blanchet, L., Faye, G., Iyer, B. R., & Sinha, S. 2008, CQGra, 25, 165003
Blanchet, L., Iyer, B. R., Will, C. M., & Wiseman, A. G. 1996, CQGra, 13, 575
Blanchet, L., & Sathyaprakash, B. S. 1995, PhRvL, 74, 1067
Blanchet, L., Damour, T., Iyer, B. R., et al. 1995, PhRvL, 74, 3515
Blandford, R., & Narayan, R. 1986, ApJ, 310, 568
Bohé, A., Hannam, M., Husa, S., et al. 2016, PhenomPv2—Technical Notes for the LAL Implementation, Tech. Rep. LIGO-T1500602, LIGO Scientific Collaboration and Virgo Collaboration, https://dcc.ligo.org/T1500602/public
Bohé, A., Shao, L., Taracchini, A., et al. 2017, PhRvD, 95, 044028
Bond, J. R., Arnett, W. D., & Carr, B. J. 1984, ApJ, 280, 825
Bouffanais, Y., Mapelli, M., Gerosa, D., et al. 2019, ApJ, 886, 25
Boyle, M., Hemberger, D., Iozzo, D. A. B., et al. 2019, CQGra, 36, 195006
Bressan, A., Marigo, P., Girardi, L., et al. 2012, MNRAS, 427, 127
Broadhurst, T., Diego, J. M., & Smoot, G. I. 2018, arXiv:1802.05273
Bromm, V., & Loeb, A. 2003, ApJ, 596, 34
Buonanno, A., Cook, G. B., & Pretorius, F. 2007, PhRvD, D75, 124018
Buonanno, A., & Damour, T. 1999, PhRvD, 59, 084006
Buonanno, A., & Damour, T. 2000, PhRvD, 62, 064015
Buonanno, A., Kidder, L. E., & Lehner, L. 2008, PhRvD, 77, 026004
Byrnes, C. T., Hindmarsh, M., Young, S., & Hawkins, M. R. S. 2018, JCAP, 1808, 041
Calderón Bustillo, J., Husa, S., Sintes, A. M., & Pürrer, M. 2016, PhRvD, 93, 084019
Calderón Bustillo, J., Laguna, P., & Shoemaker, D. 2017, PhRvD, 95, 104038
Calderón Bustillo, J., Salemi, F., Dal Canton, T., & Jani, K. 2018, PhRvD, 97, 024016
Calderón Bustillo, J., Sanchis-Gual, N., Torres-Forné, A., & Font, J. 2020, Submitted, https://dcc.ligo.org/LIGO-P1900363
Campanelli, M., Lousto, C., Zlochower, Y., & Merritt, D. 2007a, ApJL, 659, L5
Campanelli, M., Lousto, C. O., Zlochower, Y., & Merritt, D. 2007b, PhRvL, 98, 231102
Carr, B., Kühnel, F., & Sandstad, M. 2016, PhRvD, 94, 083504
Carr, B. J., & Hawking, S. W. 1974, MNRAS, 168, 399
Carullo, G., Del Pozzo, W., & Veitch, J. 2019, PhRvD, D99, 123029
Casentini, C., Verrecchia, F., Tavani, M., et al. 2019, GCN, 24623, 1
Chandra, K. V. G., Bustillo, J. C., & Pai, A. 2020, arXiv:2002.10666
Chatziioannou, K., Cotesta, R., Ghonge, S., et al. 2019, PhRvD, 100, 104015
Chatziioannou, K., Klein, A., Yunes, N., & Cornish, N. 2017, PhRvD, 95, 104004
Chen, K.-J., Woosley, S., Heger, A., Almgren, A., & Whalen, D. J. 2014, ApJ, 792, 28
Chiba, T., & Yokoyama, S. 2017, PTEP, 2017, 083E01
Clesse, S., & García-Bellido, J. 2017, PDU, 15, 142
Colpi, M., Mapelli, M., & Possenti, A. 2003, ApJ, 599, 1260
Cornish, N. J., & Littenberg, T. B. 2015, CQGra, 32, 135012
Cotesta, R., Buonanno, A., Bohé, A., et al. 2018, PhRvD, 98, 084028
Cseh, D., Webb, N. A., Godet, O., et al. 2015, MNRAS, 446, 3268
Cutler, C., Berti, E., Jani, K., et al. 2019, BAAS, 51, 109
Damour, T. 2001, PhRvD, 64, 124013
Damour, T., Jaranowski, P., & Schaefer, G. 2001, PhLB, 513, 147
Damour, T., & Vilenkin, A. 2000, PhRvL, 85, 3761
deBoer, R. J., Görres, J., Wiescher, M., et al. 2017, RvMP, 89, 035007
Del Pozzo, W., & Veitch, J. 2020, CPNest: An Efficient Python Parallelizable Nested Sampling Algorithm, https://github.com/johnveitch/cpnest, doi:10.5281/zenodo.835874
den Brok, M., Seth, A. C., Barth, A. J., et al. 2015, ApJ, 809, 101
Di Carlo, U. N., Giacobbo, N., Mapelli, M., et al. 2019, MNRAS, 487, 2947
Di Carlo, U. N., Mapelli, M., Bouffanais, Y., et al. 2020, MNRAS, 497, 1043
Divakarla, A. K., Thrane, E., Lasky, P. D., & Whiting, B. F. 2019, arXiv:1911.07998
Doctor, Z., Wysocki, D., O'Shaughnessy, R., Holz, D. E., & Farr, B. 2020, ApJ, 893, 35
Dong, X.-B., Ho, L. C., Yuan, W., et al. 2012, ApJ, 755, 167
Doyle, M., Bozzo, E., Savchenko, V., et al. 2019a, GCN, 24620, 1
Doyle, M., Bozzo, E., Savchenko, V., et al. 2019b, GCN, 24624, 1
Farmer, R., Renzo, M., de Mink, S. E., Marchant, P., & Justham, S. 2019, ApJ, 887, 53
Farr, B., Holz, D. E., & Farr, W. M. 2018, ApJL, 854, L9
Farrell, S. A., Webb, N. A., Barret, D., Godet, O., & Rodrigues, J. M. 2009, Natur, 460, 73
Favata, M., Hughes, S. A., & Holz, D. E. 2004, ApJL, 607, L5
Fedrow, J. M., Ott, C. D., Sperhake, U., et al. 2017, PhRvL, 119, 171103
Feng, H., & Soria, R. 2011, NewAR, 55, 166
Filippenko, A. V., & Ho, L. C. 2003, ApJL, 588, L13
Filippenko, A. V., & Sargent, W. L. W. 1989, ApJL, 342, L11
Fishbach, M., Farr, W. M., & Holz, D. E. 2020, ApJL, 891, L31

Fishbach, M., & Holz, D. E. 2017, ApJL, 851, L25
Fishbach, M., Holz, D. E., & Farr, B. 2017, ApJL, 840, L24
Fitchett, M. J. 1983, MNRAS, 203, 1049
Fowler, W. A., & Hoyle, F. 1964, ApJS, 9, 201
Fragione, G., Loeb, A., & Rasio, F. A. 2020, ApJL, 895, L15
Fregeau, J. M., Larson, S. L., Miller, M., O'Shaughnessy, R. W., & Rasio, F. A. 2006, ApJL, 646, L135
Fryer, C. L., Belczynski, K., Wiktorowicz, G., et al. 2012, ApJ, 749, 91
Fryer, C. L., Woosley, S. E., & Heger, A. 2001, ApJ, 550, 372
Fuller, J., & Ma, L. 2019, ApJL, 881, L1
Gair, J. R., Mandel, I., Miller, M., & Volonteri, M. 2011, GReGr, 43, 485
Gebhardt, K., Rich, R. M., & Ho, L. C. 2005, ApJ, 634, 1093
Generozov, A., Stone, N. C., Metzger, B. D., & Ostriker, J. P. 2018, MNRAS, 478, 4030
Gerosa, D. 2016, Precession, v. 1.0.3, Zenodo, doi:10.5281/zenodo.1478928
Gerosa, D., & Berti, E. 2017, PhRvD, 95, 124046
Gerosa, D., & Berti, E. 2019, PhRvD, 100, 041301
Gerosa, D., & Kesden, M. 2016, PhRvD, 93, 124066
Gerssen, J., van der Marel, R. P., Gebhardt, K., et al. 2002, AJ, 124, 3270
Giacobbo, N., Mapelli, M., & Spera, M. 2018, MNRAS, 474, 2959
Giersz, M., Leigh, N., Hypki, A., Lützgendorf, N., & Askar, A. 2015, MNRAS, 454, 3150
Giesler, M., Isi, M., Scheel, M. A., & Teukolsky, S. 2019, PhRvX, 9, 041060
Godet, O., Barret, D., Webb, N. A., Farrell, S. A., & Gehrels, N. 2009, ApJL, 705, L109
Gondán, L., Kocsis, B., Raffai, P., & Frei, Z. 2018, ApJ, 860, 5
Graff, P. B., Buonanno, A., & Sathyaprakash, B. 2015, PhRvD, 92, 022002
Graham, M. J., Ford, K. E. S., McKernan, B., et al. 2020, PhRvL, 124, 251102
Greene, J. E., & Ho, L. C. 2004, ApJ, 610, 722
Greene, J. E., & Ho, L. C. 2007, ApJ, 670, 92
Greene, J. E., Strader, J., & Ho, L. C. 2019, arXiv:1911.09678
Gültekin, K., Miller, M. C., & Hamilton, D. P. 2006, ApJ, 640, 156
Gurkan, A. M., Freitag, M., & Rasio, F. A. 2004, ApJ, 604, 632
Hailey, C. J., Mori, K., Bauer, F. E., et al. 2018, Natur, 556, 70
Hannam, M., Husa, S., Baker, J. G., et al. 2009, PhRvD, 79, 084025
Hannam, M., Schmidt, P., Bohé, A., et al. 2014, PhRvL, 113, 151101
Hannuksela, O. A., Haris, K., Ng, K. K. Y., et al. 2019, ApJL, 874, L2
Haris, K., Mehta, A. K., Kumar, S., Venumadhav, T., & Ajith, P. 2018, arXiv:1807.07062
Harris, W. E. 1996, AJ, 112, 1487
Healy, J., Lange, J., O'Shaughnessy, R., et al. 2018, PhRvD, 97, 064027
Healy, J., & Lousto, C. O. 2017, PhRvD, 95, 024037
Healy, J., Lousto, C. O., Lange, J., et al. 2019, PhRvD, 100, 024021
Heger, A., Fryer, C. L., Woosley, S. E., Langer, N., & Hartmann, D. H. 2003, ApJ, 591, 288
Hinder, I., Buonanno, A., Boyle, M., et al. 2014, CQGra, 31, 025012
Hoang, B.-M., Naoz, S., Kocsis, B., Rasio, F. A., & Dosopoulou, F. 2018, ApJ, 856, 140
Hofmann, F., Barausse, E., & Rezzolla, L. 2016, ApJL, 825, L19
Holley-Bockelmann, K., Gültekin, K., Shoemaker, D., & Yunes, N. 2008, ApJ, 686, 829
Holz, D. E., & Wald, R. M. 1998, PhRvD, 58, 063501
Husa, S., Khan, S., Hannam, M., et al. 2016, PhRvD, 93, 044006
IceCube Collaboration 2019, GCN, 24618, 1
Isi, M., Giesler, M., Farr, W. M., Scheel, M. A., & Teukolsky, S. A. 2019, arXiv:1905.00869
Jani, K., Healy, J., Clark, J. A., et al. 2016, CQGra, 33, 204001
Jani, K., & Loeb, A. 2020, ApJL, 889, L35
Jani, K., Shoemaker, D., & Cutler, C. 2020, NatAs, 4, 260
Jiménez-Forteza, X., Keitel, D., Husa, S., et al. 2017, PhRvD, D95, 064024
Johnson-McDaniel, N. K., Gupta, A., Ajith, P., et al. 2016, Determining the Final Spin of a Binary Black Hole System Including In-plane Spins: Method and Checks of Accuracy, Tech. Rep. LIGO-T1600168, https://dcc.ligo.org/T1600168/public
Kaaret, P., Feng, H., & Roberts, T. P. 2017, ARA&A, 55, 303
Kaaret, P., Prestwich, A. H., Zezas, A., et al. 2001, MNRAS, 321, L29
Kamaretsos, I., Hannam, M., Husa, S., & Sathyaprakash, B. 2012, PhRvD, 85, 024018
Keitel, D., Forteza, X. J., Husa, S., et al. 2017, PhRvD, 96, 024006
Kelly, B. J., & Baker, J. G. 2013, PhRvD, 87, 084004
Khan, S., Chatziioannou, K., Hannam, M., & Ohme, F. 2019, PhRvD, 100, 024059
Khan, S., Ohme, F., Chatziioannou, K., & Hannam, M. 2020, PhRvD, 101, 024056
Khan, S., Husa, S., Hannam, M., et al. 2016, PhRvD, 93, 044007
Khlopov, M. Yu. 2010, RAA, 10, 495
Kidder, L. E. 2008, PhRvD, 77, 044016
Kim, C., Kalogera, V., & Lorimer, D. R. 2003, ApJ, 584, 985
Kimball, C., Berry, C., & Kalogera, V. 2020a, RNAAS, 4, 2
Kimball, C., Talbot, C., Berry, C. P. L., et al. 2020b, arXiv:2005.00023
Kimpson, T. O., Spera, M., Mapelli, M., & Ziosi, B. M. 2016, MNRAS, 463, 2443
Kızıltan, B., Baumgardt, H., & Loeb, A. 2017, Natur, 545, 510
Klimenko, S., Vedovato, G., Drago, M., et al. 2016, PhRvD, 93, 042004
Kozai, Y. 1962, AJ, 67, 591
Kremer, K., Ye, C. S., Rui, N. Z., et al. 2019, arXiv:1911.00018
Kumar Mehta, A., Tiwari, P., Johnson-McDaniel, N. K., et al. 2019, PhRvD, 100, 024032
Lange, J., O'Shaughnessy, R., & Rizzo, M. 2018, arXiv:1805.10457
Lanzoni, B., Mucciarelli, A., Origlia, L., et al. 2013, ApJ, 769, 107
Lenon, A. K., Nitz, A. H., & Brown, D. A. 2020, arXiv:2005.14146
Leung, S.-C., Nomoto, K., & Blinnikov, S. 2019, ApJ, 887, 72
Li, A. K. Y., Lo, R. K. L., Sachdev, S., Li, T. G. F., & Weinstein, A. J. 2019, arXiv:1904.06020
Li, S.-S., Mao, S., Zhao, Y., & Lu, Y. 2018, MNRAS, 476, 2220
Li, T. G. F., Del Pozzo, W., Vitale, S., et al. 2012a, PhRvD, 85, 082003
Li, T. G. F., Del Pozzo, W., Vitale, S., et al. 2012b, JPhCS, 363, 012028
Lidov, M. L. 1962, P&SS, 9, 719
Lin, D., Strader, J., Carrasco, E. R., et al. 2018, NatAs, 2, 656
Lin, D., Strader, J., Romanowsky, A. J., et al. 2020, ApJL, 892, L25
Lipunov, V., Gorbovskoy, E., Kornilov, V., et al. 2019, GCN, 24619, 1
Littenberg, T. B., & Cornish, N. J. 2015, PhRvD, 91, 084034
Lodato, G., & Natarajan, P. 2006, MNRAS, 371, 1813
Loeb, A., & Rasio, F. A. 1994, ApJ, 432, 52
London, L., Khan, S., Fauchon-Jones, E., et al. 2018, PhRvL, 120, 161102
London, L. T. 2018, arXiv:1801.08208
Lousto, C. O., Nakano, H., Zlochower, Y., & Campanelli, M. 2010, PhRvD, 81, 084023
Lousto, C. O., & Zlochower, Y. 2011, PhRvL, 107, 231102
Lovelace, G., Lousto, C. O., Healy, J., et al. 2016, CQGra, 33, 244002
Lower, M. E., Thrane, E., Lasky, P. D., & Smith, R. 2018, PhRvD, 98, 083028
Lützgendorf, N., Kissler-Patig, M., Gebhardt, K., et al. 2013, A&A, 552, A49
Lützgendorf, N., Kissler-Patig, M., Noyola, E., et al. 2011, A&A, 533, A36
Mandel, I., & O'Shaughnessy, R. 2010, CQGra, 27, 114007
Mann, C. R., Richer, H., Heyl, J., et al. 2019, ApJ, 875, 1
Mapelli, M. 2016, MNRAS, 459, 3432
Mapelli, M., Spera, M., Montanari, E., et al. 2020, ApJ, 888, 76
Marchant, P., Renzo, M., Farmer, R., et al. 2019, ApJ, 882, 36
Matsumoto, H., Tsuru, T. G., Koyama, K., et al. 2001, ApJL, 547, L25
McIsaac, C., Keitel, D., Collett, T., et al. 2019, arXiv:1912.05389
McKernan, B., Ford, K. E. S., Bartos, I., et al. 2019, ApJL, 884, L50
McKernan, B., Ford, K. E. S., Bellovary, J., et al. 2018, ApJ, 866, 66
McKernan, B., Ford, K. E. S., Kocsis, B., Lyra, W., & Winter, L. M. 2014, MNRAS, 441, 900
McKernan, B., Ford, K. E. S., Lyra, W., & Perets, H. B. 2012, MNRAS, 425, 460
McKernan, B., Ford, K. E. S., O'Shaughnessy, R., & Wysocki, D. 2020, MNRAS, 494, 1203
Mehta, A. K., Mishra, C. K., Varma, V., & Ajith, P. 2017, PhRvD, 96, 124010
Merritt, D., Milosavljević, M., Favata, M., Hughes, S. A., & Holz, D. E. 2004, ApJL, 607, L9
Mezzacappa, A., Marronetti, P., & Landfield, R. E. 2020, PhRvD, 102, 023027
Mezcua, M. 2017, IJMPD, 26, 1730021
Mezcua, M., Civano, F., Fabbiano, G., Miyaji, T., & Marchesi, S. 2016, ApJ, 817, 20
Mezcua, M., Civano, F., Marchesi, S., et al. 2018, MNRAS, 478, 2576
Mezcua, M., Roberts, T. P., Lobanov, A. P., & Sutton, A. D. 2015, MNRAS, 448, 1893
Miller, M. 2009, CQGra, 26, 094031
Miller, M. C., & Colbert, E. J. M. 2004, IJMPD, 13, 1
Miller, M. C., & Hamilton, D. P. 2002, MNRAS, 330, 232
Miller-Jones, J. C. A., Wrobel, J. M., Sivakoff, G. R., et al. 2012, ApJL, 755, L1
Miralda-Escudé, J., & Gould, A. 2000, ApJ, 545, 847
Mishra, C. K., Kela, A., Arun, K. G., & Faye, G. 2016, PhRvD, 93, 084054
Mishra, C. K., Arun, K. G., Iyer, B. R., et al. 2010, PhRvD, 82, 064010
Monari, G., Famaey, B., Carrillo, I., et al. 2018, A&A, 616, L9
Morris, M. 1993, ApJ, 408, 496
Negoro, H., Kawai, N., Sugizaki, M., et al. 2019, GCN, 24625, 1
Ng, K. K. Y., Wong, K. W. K., Broadhurst, T., & Li, T. G. F. 2018, PhRvD, 97, 023012
Nitz, A. H., Dent, T., Davies, G. S., et al. 2019, ApJ, 891, 123

Noyola, E., Gebhardt, K., & Bergmann, M. 2008, ApJ, 676, 1008
Nyland, K., Marvil, J., Wrobel, J. M., Young, L. M., & Zauderer, B. A. 2012, ApJ, 753, 103
O'Connor, E. P., & Couch, S. M. 2018, ApJ, 865, 81
O'Leary, R. M., Kocsis, B., & Loeb, A. 2009, MNRAS, 395, 2127
O'Leary, R. M., Meiron, Y., & Kocsis, B. 2016, ApJL, 824, L12
O'Leary, R. M., Rasio, F. A., Fregeau, J. M., Ivanova, N., & O'Shaughnessy, R. 2006, ApJ, 637, 937
Ober, W. W., El Eid, M. F., & Fricke, K. J. 1983, A&A, 119, 61
Oguri, M. 2018, MNRAS, 480, 3842
Oguri, M. 2019, RPPh, 82, 126901
Okounkova, M. 2020, arXiv:2004.00671
Ossokine, S., Buonanno, A., Marsat, S., et al. 2020, arXiv:2004.09442
Ota, I., & Chirenti, C. 2020, PhRvD, 101, 104005
Pan, Y., Buonanno, A., Boyle, M., et al. 2011, PhRvD, 84, 124052
Pang, P. T. H., Hannuksela, O. A., Dietrich, T., Pagano, G., & Harry, I. W. 2020, MNRAS, 495, 3740
Pekowsky, L., O'Shaughnessy, R., Healy, J., & Shoemaker, D. 2013, PhRvD, 88, 024040
Perera, B. B. P., Stappers, B. W., Lyne, A. G., et al. 2017, MNRAS, 468, 2114
Portegies Zwart, S. F., Baumgardt, H., Hut, P., Makino, J., & McMillan, S. L. W. 2004, Natur, 428, 724
Portegies Zwart, S. F., & McMillan, S. L. W. 2002, ApJ, 576, 899
Powell, J., & Müller, B. 2019, MNRAS, 487, 1178
Punturo, M., Abernathy, M., Acernese, F., et al. 2010, CQGra, 27, 194002
Pürrer, M., & Haster, C.-J. 2020, PhRvR, 2, 023151
Racine, E. 2008, PhRvD, 78, 044021
Reines, A. E., Greene, J. E., & Geha, M. 2013, ApJ, 775, 116
Reitze, D., Adhikari, R. X., Ballmer, S., et al. 2019, BAAS, 51, 35
Renzo, M., Farmer, R. J., Justham, S., et al. 2020, MNRAS, 493, 4333
Riess, A. G., Casertano, S., Yuan, W., Macri, L. M., & Scolnic, D. 2019, ApJ, 876, 85
Rodriguez, C. L., Amaro-Seoane, P., Chatterjee, S., et al. 2018, PhRvD, 98, 123005
Rodriguez, C. L., Zevin, M., Amaro-Seoane, P., et al. 2019, PhRvD, 100, 043027
Rodriguez, C. L., Zevin, M., Pankow, C., Kalogera, V., & Rasio, F. A. 2016, ApJL, 832, L2
Romero-Shaw, I. M., Lasky, P. D., & Thrane, E. 2019, MNRAS, 490, 5210
Romero-Shaw, I. M., Talbot, C., Biscoveanu, S., et al. 2020, arXiv:2006.00714
Samsing, J. 2018, PhRvD, 97, 103014
Samsing, J., Askar, A., & Giersz, M. 2018, ApJ, 855, 124
Samsing, J., & D'Orazio, D. J. 2018, MNRAS, 481, 5445
Samsing, J., MacLeod, M., & Ramirez-Ruiz, E. 2014, ApJ, 784, 71
Samsing, J., & Ramirez-Ruiz, E. 2017, ApJL, 840, L14
Sana, H., Le Bouquin, J. B., Lacour, S., et al. 2014, ApJS, 215, 15
Schmidt, P., Hannam, M., & Husa, S. 2012, PhRvD, 86, 104063
Schmidt, P., Hannam, M., Husa, S., & Ajith, P. 2011, PhRvD, 84, 024046
Schmidt, P., Ohme, F., & Hannam, M. 2015, PhRvD, 91, 024043
Servillat, M., Farrell, S. A., Lin, D., et al. 2011, ApJ, 743, 6
Sesana, A. 2016, PhRvL, 116, 231102
Seth, A. C., Cappellari, M., Neumayer, N., et al. 2010, ApJ, 714, 713
Silsbee, K., & Tremaine, S. 2017, ApJ, 836, 39
Singer, L. P., Goldstein, D. A., & Bloom, J. S. 2019, arXiv:1910.03601
Singer, L. P., & Price, L. 2016, PhRvD, 93, 024013
Smith, G. P., Jauzac, M., Veitch, J., et al. 2018, MNRAS, 475, 3823
Soria, R., Hakala, P. J., Hau, G. K. T., Gladstone, J. C., & Kong, A. K. H. 2012, MNRAS, 420, 3599
Speagle, J. S. 2020, MNRAS, 493, 3132
Spera, M., & Mapelli, M. 2017, MNRAS, 470, 4739
Spera, M., Mapelli, M., Giacobbo, N., et al. 2019, MNRAS, 485, 889
Stevenson, S., Sampson, M., Powell, J., et al. 2019, ApJ, 882, 121
Stone, N. C., Metzger, B. D., & Haiman, Z. 2017, MNRAS, 464, 946
Strader, J., Chomiuk, L., Maccarone, T. J., et al. 2012, ApJL, 750, L27
Strohmayer, T. E., & Mushotzky, R. F. 2003, ApJL, 586, L61
Sukhbold, T., Ertl, T., Woosley, S. E., Brown, J. M., & Janka, H.-T. 2016, ApJ, 821, 38
Sutton, A. D., Roberts, T. P., Walton, D. J., Gladstone, J. C., & Scott, A. E. 2012, MNRAS, 423, 1154
Tagawa, H., Haiman, Z., & Kocsis, B. 2020, ApJ, 898, 25
Takahashi, K., Yoshida, T., & Umeda, H. 2018, ApJ, 857, 111
Talbot, C., Smith, R., Thrane, E., & Poole, G. B. 2019, PhRvD, 100, 043030
Talbot, C., & Thrane, E. 2018, ApJ, 856, 173
Tremou, E., Strader, J., Chomiuk, L., et al. 2018, ApJ, 862, 16
Tse, M., Yu, H., Kijbunchoo, N., et al. 2019, PhRvL, 123, 231107
Turpin, D., Dagoneau, N., Xin, L. P., et al. 2019a, GCN, 24657, 1
Turpin, D., Dagoneau, N., Xin, L. P., et al. 2019b, GCN, 24658, 1
Udall, R., Jani, K., Lange, J., et al. 2020, ApJ, 900, 80
van der Marel, R. P. 2004, in Coevolution of Black Holes and Galaxies, ed. L. C. Ho (Cambridge: Cambridge Univ. Press), 37
van der Marel, R. P., & Anderson, J. 2010, ApJ, 710, 1063
van Son, L. A. C., de Mink, S. E., Broekgaarden, F. S., et al. 2020, ApJ, 897, 100
Varma, V., & Ajith, P. 2017, PhRvD, 96, 124024
Varma, V., Ajith, P., Husa, S., et al. 2014, PhRvD, 90, 124004
Varma, V., Field, S. E., Scheel, M. A., et al. 2019, PhRvR, 1, 033015
Varma, V., Isi, M., & Biscoveanu, S. 2020, PhRvL, 124, 101104
Veitch, J., Raymond, V., Farr, B., et al. 2015, PhRvD, 91, 042003
Vishveshwara, C. V. 1970, PhRvD, 1, 2870
Vitale, S. 2016, PhRvL, 117, 051102
Volonteri, M. 2010, A&ARv, 18, 279
Wang, S., Liu, J., Bai, Y., & Guo, J. 2015, ApJL, 812, L34
Watson, A. M., Dichiara, S., Butler, N., et al. 2019, GCN, 24644, 1
Webb, N., Cseh, D., Lenc, E., et al. 2012, Sci, 337, 554
Wen, L. 2003, ApJ, 598, 419
Woosley, S. E. 2017, ApJ, 836, 244
Woosley, S. E. 2019, ApJ, 878, 49
Woosley, S. E., Blinnikov, S., & Heger, A. 2007, Natur, 450, 390
Wysocki, D., O'Shaughnessy, R., Lange, J., & Fang, Y.-L. L. 2019, PhRvD, 99, 084026
Yang, Y., Bartos, I., Gayathri, V., et al. 2019a, PhRvL, 123, 181101
Yang, Y., Bartos, I., Haiman, Z., et al. 2019b, ApJ, 876, 122
Yoshida, T., Umeda, H., Maeda, K., & Ishii, T. 2016, MNRAS, 457, 351
Zackay, B., Dai, L., Venumadhav, T., Roulet, J., & Zaldarriaga, M. 2019, arXiv:1910.09528
Zevin, M., Samsing, J., Rodriguez, C., Haster, C.-J., & Ramirez-Ruiz, E. 2019, ApJ, 871, 91
Zocchi, A., Gieles, M., & Hénault-Brunet, V. 2019, MNRAS, 482, 4713